Synthesis and Characterization of Novel Ternary Transition Metal Borides and New Synthesis Methods for superhard ReB_2 and Clathrate of Type-I

by

Burcu Uslu

A Thesis Submitted to the
Graduate School of Engineering
in Partial Fulfillment of the Requirements for
the Degree of

Master of Science
in
Material Science and Engineering
Koç University

August 2010

Koc University

Graduate School of Sciences and Engineering

This is to certify that I have examined this copy of a master's thesis by

Burcu Uslu

and have found that it is complete and satisfactory in all respects,
and that any and all revisions required by the final
examining committee have been made.

Committee Members:

_____

Mehmet Suat Somer, Ph. D. (Advisor)

_____

Levent Adem Demirel, Ph. D.

_____

Özlem Keskin, Ph. D. (Advisor)

Date: _____

ABSTRACT

The present thesis consists of three chapters: synthesis and characterization of ternary transition metal borides, superhard rhenium diboride (ReB_2) and clathrate of type-I. The first chapter describes the synthesis and characterization of ternary transition metal borides within the systems of Ta-Co-B, Ta-Ni-B, Ta-Re-B, Nb-Re-B, Hf-Ni-B, Ta-La-B and Re-Ni-B. The employed preparation technique was the solid state high temperate reactions performed in a home-made arc melting furnace. Characterization and identification of the obtained phases was done by X-ray powder diffraction. In case of Nb-Re-B system, niobium successfully substituted the tantalum atoms of $Ta_3Re_3B_4$ and a novel ternary compound was synthesized with the composition of $Nb_3Re_3B_4$. Except for the Re-Ni-B system, all products were phase mixtures of ternaries with already well-known binaries. A novel ternary compound was isolated with the nominal composition Re:Ni:B = 1:1:1. Optical micrographs confirmed that new "phase" comprised two different ternary borides, the shiny one being Re and the dark one Ni-rich, respectively. The analysis of the rhenium rich phase was performed with WDXS yielding an approximate composition of $Re_{20}Ni_3B_{11}$. Based on this, the empirical formula of the Ni-rich dark phase was calculated to $ReNi_{6.67}B_4$. Re:Ni:B = 1:1:1 could also be synthesized using the lead flux method.

The second part of the study is dedicated to rhenium diboride, the second hardest material known after diamond. The preparation was done for the first time in a lead flux at 1073 K which is the lowest synthesis temperature recorded for ReB_2, yet. In addition, both the reaction time (from 12 h to 5 h) and the molar ratios of the reactants (from Re/B/Flux Metal = 1:2:50 to 1:2:10) could be reduced dramatically. Excess lead was removed in boiling HCl solution. Characterizations of the products were performed using X-ray powder diffraction method and ICP-OES. Lead free inhesion of final product was audited with ICP-OES and EDXS yielding the chemical composition 1:1.98 which deviates only marginally from the ideal 1:2 ratio. The thermal stability of the compound was investigated up to 1373 K by DTA. The average crystallite size of

the synthesized powder was measured as 933 nm by the Hall-Williamson method and could successfully be reduced to 344 nm by ball-milling. The second synthesis technique employed on ReB_2 was microwave induced plasma. In this case the elements were exposed to hydrogen plasma (1200 W) for 30 minutes, resulting in formation of ReB_2 and a foreign phase. To exclude that the formation of the foreign phase was initialized by the contaminations in the used amorphous B, boron powder free of Mg was employed. Experiments showed that the formation of the byproduct is "intrinsic" and not affected by the impurities. DTA measurements confirmed that foreign phase decomposes at 948 K to ReB_2 and elemental boron. Annealing process and high temperatures inhibited the formation of the unknown phase indicating that its formation under microwave conditions is the result of the moderate temperatures governing in the hydrogen plasma. Synthesis of ReB_2 from stoichiometric mixture of the elements by arc melting is the most common preparation technique. In the present study, it could be proved that the start from the stoichiometric amounts of elements was not a successful route, effecting the final composition of the product due to the evaporation of amorphous boron during the arc melting process. Our results reveal that starting from molar ratios of Re:B = 1:4 to 1:7 yield the best result with respect to phase purity of ReB_2

In the last part of the thesis, Clathrate-I compound, K_8Ge_{46} was prepared via two novel methods: synthesis in liquid ammonia and by microwave induced plasma. In both cases, the formation of the final product was accompanied by the presence of elemental germanium. Hydrogen plasma was the "method of choice" giving the highest yield of clathrate compound and the lowest value for the byproduct elemental germanium.

Özet

Bu yüksek lisans çalışması üçlü metal borürleri, aşırı sert (superhard) renyum diborür ve tip-I klatratlarının sentez ve karakterizasyonu olmak üzere üç bölümden oluşmaktadır. Bu çalışmanın ilk bölümünde üçlü metal borürlerin, Ta-Co-B, Ta-Ni-B, Ta-Re-B, Nb-Re-B, Hf-Ni-B, Ta-La-B ve Re-Ni-B, ark eritme tekniği ile sentez ve karakterizasyonları çalışılmıştır. Bütün fazların karakterizasyonu X-ışını toz kırınım metodu ile yapılmıştır. $Ta_3Re_3B_4$ fazı baz alınarak tantalum atomları niobium ile değiştirilmiş ve $Nb_3Re_3B_4$ 'yeni' üçlü bileşiği elde edilmiştir. Re-Ni-B üçlü fazı hariç, bütün fazlarda yeni üçlü metal borür oluşumu bilindik ikili faz oluşumu ile birlikte gözlenmiştir. Yeni üçlü metal borür oluşumu Re/Ni/B un 1:1:1 oranında bileşimi ile elde edilmiştir. Optik mikrograf ölçümleri iki tane üçlü faz olduğunu ve EDXS ölçümleri de bir fazın renyum zengin diğerinin ise nikel zengin olduğunu göstermiştir. WDXS ile renyum zengin fazdan yapılan kuantifikasyon ölçümleri $Re_{20}Ni_3B_{11}$ kompozisyonunu vermiştir. Bu bilgi kullanılarak nikel zengin fazın kompozisyonu $ReNi_{6.67}B_4$ olarak belirlenmiştir. Aynı bileşik kurşun eriği içerisinde Re:Ni:B = 1:1:1 olarak da sentezlenmiştir.

Bu çalışmanın ikinci bölümde aşırı sert (superhard) renyum diborürün sentezi ve karakterizasyonu incelenmiştir. Yapılan çalışmada, ReB_2 ilk defa kurşun eriği içerisinde 1073 K de sentezlenmiştir ve bu sıcaklık literatürde verilen ReB_2 sentez sıcaklıklarının en düşüğüdür. Aynı çalışma, benzer bir çalışmaya kıyasla, sadece reaksiyon sıcaklığını düşürmemiş aynı zamanda reaksiyon süresini (12 saatten 5 saate) ve reaksiyona giren kimyasalların mol oranlarını (Re/B/Eriyik (flux) Metali oranları 1:2:50 iken 1:2:10) da dramatik ölçüde azaltmıştır. Elde edilen maddenin karakterizasyonu toz X-ışını kırımın (X-ray powder diffraction; XRPD) metodu ve indüktif olarak çiftleşmiş plazma/optik emisyon spektroskopisi (ICP-OES) ile yapılmıştır. ICP-OES sonuçlarına göre sentezlenen bileşiğin kompozisyonu 1:1.98 dir ve bu ideal orandan, 1:2, çok az bir sapma gösterir. Sistemin herhangi bir kurşun katkısını barındırmadığı ICP-OES ve

energy dağılımlı X-ışını spektroskopisi (EDXS) ile kanıtlanmıştır. Elde edilen maddenin 1373 K e kadar olan termal dayanıklılığı diferansiyel termal analiz (DTA) ölçümü sonucu bulunmuştur. Sentezlenen maddenin kristalit boyutu Hall-Williamson metodu ile 933 nm olarak tespit edilmiştir. Bilyeli freze (Ball-milling) metodu ile bu değer 344 nm ye çekilmiştir. ReB_2 sentezi için daha önce literatürde rastlanmamış bir metot, mikrodalga indüktif plazma, önerilmiştir. Elementlerin direk bileşimi ve hidrojen plazması (1200 W, 30 dakika) tercih edilmiş ve ReB_2 oluşumu ile birlikte yeni bir faz tespit edilmiştir. ReB_2 ve yeni fazın karakterizasyonu XRPD ile yapılmıştır. Oluşan fazın kullanılan amorf bordaki safsızlıktan gelmediğini kanıtlamak için elemental bor iki farklı metot ile sentezlendi: Metallo-termal (Mg safsızlığı) ve diboran dekompozisyonu. İki farklı türde sentezlenen borla da aynı faz oluşumu gözlendi. Diferansiyel termal analiz sonuçlarına göre elde edilen yeni faz 948 K de ReB_2 ve elementel bora dekompoze oluyor. Bu nedenle, yeni fazın sentezi sadece mikrodalga indüktif plazma gibi soğuk sentez imkânı ve yüksek reaksiyon hızı sağlayan bir sistem ile mümkün oldu. Daha önceki çalışmalarda ReB_2 sentezinin ark eritme metodu ile yapılabildiği belirtilmiş ancak atomik oranlar verilmemiştir. Ark eritme sentezi sırasında buharlaşan bor nedeni ile ReB_2'ın ark eritme ile sentezi stokiyometrik değerler ile mümkün değildir. Bu nedenle, sistematik bir çalışma ile kullanılması gereken atomik oranlar tespit edilmiştir. Re/B un 1:4 atomik oranından başlayarak 1:7 ye kadar olan alanda ReB_2 sentezlenebilmiştir. Çalışmanın karakterizasyonu XRPD ile yapılmıştır.

Bu çalışmanın üçüncü bölümünde, Klatrat-I bileşiği olan K_8Ge_{46} sentezi K_4Ge_9'dan başlayarak yeni iki metot ile gerçekleştirilmiştir: amonyak içerisinde ve mikrodalga indüktif plazma ile. İki sentezde de elementel germanyum oluşumu ile birlikte gözlenmiştir. Çalışmada hidrojen plasma tercih edilmiş ve en az elementel germanyum ve en çok klatrat oluşumu 600 W güç ve 40 dakika reaksiyon süresinde gözlenmiştir.

ACKNOWLEDGEMENTS

I would like to thank Prof. Mehmet SOMER for his superior guidance. I was one of the luckiest students to have the chance of working with him. I did not only learn a lot of things from him in terms of chemistry but also learned how to live the day. He believed in me and never stopped motivating me.

I don't now how this thesis would be without Selçuk Acar. The jealousy that I feel in his extraordinary working habits made me a hard working student. Many times with his offbeat lab skills, we made the most impossible dreams come true.

I should also thank to Umut Aydemir, Dr. Michael Baitinger and Max Planck Institute, Dresden. They supported me, educated me; moreover, they favored me with many kinds of chemicals and analyses.

My sincere thanks to the angel of inorganic lab: Dr. Anna Maria Miko. All the time, she made me feel important. Pınar and Merve made me feel like I am home. Thanks to all of my colleagues in the laboratory: Ali, Ahmet, Gizem and Muharrem abi for making those long years as enjoyable as they were.

I would like to thank every professor who helped me to improve myself. I thank to Prof. Levent Demirel and Dr. Özgür Birer because they scared me at most and I worked even much harder. I would like to thank to Dr. Ugur Ünal because he always treated me as a friend and more importantly, I would like to thank Prof. Yılgör and his wife because they guided me in terms of how a good hearted person should be and should not be.

I would like to thank my parents for their endless support and encouragement. They trusted in me at every step I have taken so far. I am very lucky to be a part of such a wonderful family. Last but not least I should thank to Azizoğlu for holding my hand despite every kind of moodiness I've made…

Table of Contents

List of Tables

List of Figures

Chapter 1

Overview

Transition Metal Borides

The modern inorganic chemistry defines the transition elements according to the filling of the 3d, 4d and 5d shells and in some cases that definition extends to include lanthanides and actinides. Transition elements cover the components between groups 3 and 12 of the periodic table. It comprises three rows and the first row consists of the elements from scandium to zinc, second row consists of the elements from yttrium to cadmium and the third row consists of the elements from lanthanum to mercury. The reason why they are called as transition elements is due to their *transitional* position between the metallic elements of groups 1 and 2 and predominantly non-metallic elements of groups 13 to 18. Since, they have typical metallic properties; they are also called as transition metals. It is hard to address a single feature for all transition elements; however, it can be said that all of them possess filled or partially filled valence *d* orbitals in one or more of their oxidation states. First row transition elements acquire the filling of the 3*d*, second row elements acquire the filling of the 4*d* and third row elements acquire the filling of 5*d* orbitals. Their configuration is presented in Table 1.1 [1].

Table 1.1 The electronic configurations of transition elements

Scandium	$[Ar]3d^14s^2$	Yttrium	$[Kr]4d^15s^2$	Lanthanum	$[Xe]5d^16s^2$
Titanium	$[Ar]3d^24s^2$	Zirconium	$[Kr]4d^25s^2$	Hafnium	$[Xe]4f^{14}5d^26s^2$
Vanadium	$[Ar]3d^34s^2$	Niobium	$[Kr]4d^45s^1$	Tantalum	$[Xe]4f^{14}5d^36s^2$
Chromium	$[Ar]3d^54s^1$	Molybdenum	$[Kr]4d^55s^1$	Tungsten	$[Xe]4f^{14}5d^46s^2$
Manganese	$[Ar]3d^54s^2$	Technetium	$[Kr]4d^55s^2$	Rhenium	$[Xe]4f^{14}5d^56s^2$
Iron	$[Ar]3d^64s^2$	Ruthenium	$[Kr]4d^75s^1$	Osmium	$[Xe]4f^{14}5d^66s^2$
Cobalt	$[Ar]3d^74s^2$	Rhodium	$[Kr]4d^85s^1$	Iridium	$[Xe]4f^{14}5d^76s^2$
Nickel	$[Ar]3d^84s^2$	Palladium	$[Kr]\ 4d^{10}5s^0$	Platinum	$[Xe]4f^{14}5d^96s^1$
Copper	$[Ar]3d^{10}4s^1$	Silver	$[Kr]4d^{10}5s^1$	Gold	$[Xe]4f^{14}5d^{10}6s^1$
Zinc	$[Ar]3d^{10}4s^2$	Cadmium	$[Kr]4d^{10}5s^2$	Mercury	$[Xe]4f^{14}5d^{10}6s^2$

Transition elements display interesting properties such as variable oxidation states including zero or negative oxidation states. Metal ions which belong to group 1 or 2 have a single valence state and the other ones usually possess two; however, all transition metals exhibit a wide range of valencies. Paramagnetism in transition elements is a result of unpaired electrons in *d* orbitals and diamagnetism is characteristic to the compounds where all the electrons are paired in *d* orbitals. Oxidation states of the transition metals used in the study are presented in the table 1.2 [2].

Table 1.2 The oxidation states of some transition metals used in the study. Common oxidation states are shown in red.

	Re	Ni	Ta	Co	Nb	Hf	Fe
-1	√	√	√	√	√		
0	√						
1	√	√		√			
2	√	√	√	√	√	√	√
3	√	√	√	√	√	√	√
4	√	√	√	√	√	√	
5	√		√	√	√		
6	√						
7	√						

Transition metal compounds are as much interesting as the transition metal elements. In order to understand the reason lies beneath, their electronic configuration should be studied in detail. Cursory examination on Table 1.1 leads to the presence of *d* orbitals in every element's configuration and their influence on bonding should not be underestimated. In fact, a mutual relation is offered between the *d* orbitals and bonding electrons, in which *d* orbitals are affected by the bonding electrons and also, bonding electrons are affected by the orbitals. Therefore, transition-metal chemistry investigates that proposed mutual relation in terms of two theories: Crystal Field Theory (CFT) and Ligand Field Theory (LFT).

Crystal Field theory proposes that outer or non-core electrons are exposed to three main energetic restrains a) kinetic energy b) attraction of the nucleus and c) repulsion of one another. Besides those, there will be a non-spherical electric field that comes from the surrounding ions. That electric field is called as the 'crystalline field', in short 'crystal field'. Theory is developed by considering the energy changes in

degenerate *d* orbitals and Figure 1.1 shows the angular forms of five degenerate *d* orbitals [1].

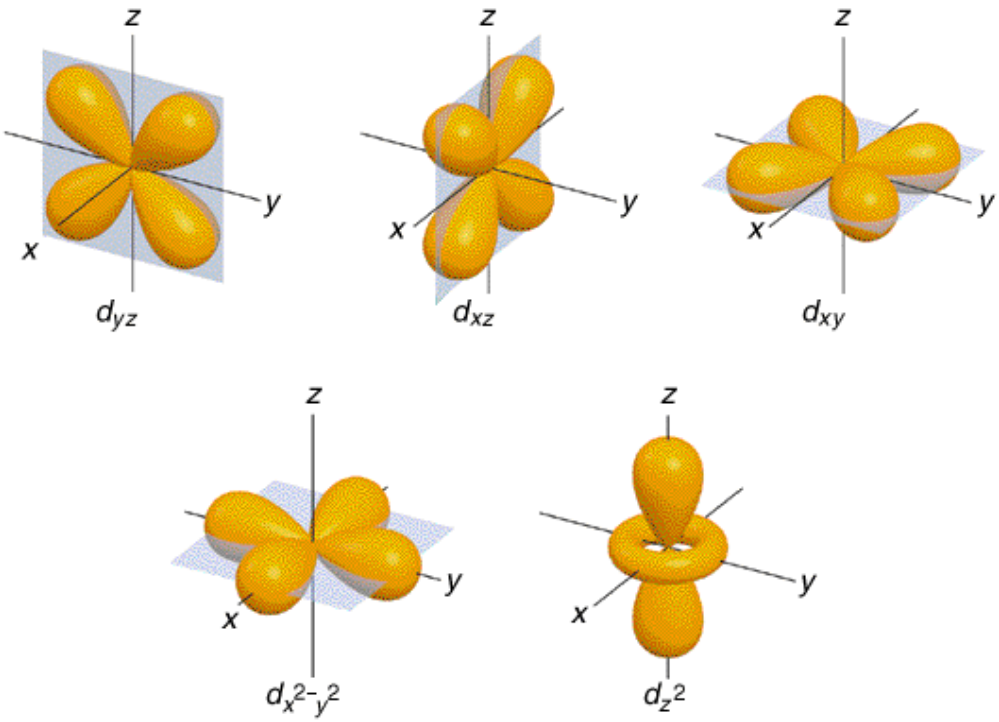

Figure 1.1 The angular forms of the five *d* orbitals

According to the theory, charges are situated at the main axes, x,y and z, and d_{z2} and d_{x2-y2} orbitals ; however d_{xy}, d_{xz} and d_{yz} are situated in between the main axes. Each electron in orbitals assumed energetically equivalent. Electrons' of an approaching ligand will be closer to some of the *d* orbitals of the metal. The repulsion between the electrons of the ligand and the electrons in the *d* orbitals of metal increases the energy of those orbitals. Since d_{xy}, d_{xz} and d_{yz} lie between the ligand ions, they will be less affected by that repulsion and d_{z2} and d_{x2-y2} orbitals will be raised energetically. This is called as splitting of *d* orbitals and many properties of transition metals are coming from splitting, relative energies. Orbital splitting diagram is a good way to learn about a compound's magnetic properties such as a compound with an unpaired electron in its

splitting diagram will be paramagnetic and it will be attracted by magnetic fields. On the other hand, a compound with a paired electron in its orbital splitting diagram will be diamagnetic [1,4].

Manganese oxide is a good example to illustrate the theory. Figure 1.2 shows that $3d_{z2}$ and $3d_{x2-y2}$ orbitals of Mn^{2+} ion point directly to the six O^{2-} ions; however d_{xy}, d_{xz} and d_{yz} lie between the O^{2-} ions, so they are less repelled by the ligand electrons [5].

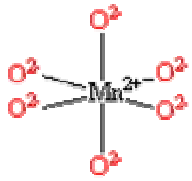

Figure 1.2 Representation of manganese (II) oxide (MnO).

Crystal Field theory does not give information about bonding; therefore, researchers come up with another theory which is called Ligand Field. Ligand Field theory treats metal and ligand interaction as a covalent bonding interaction and suggests that even though crystal-field splitting is too small as in the case of 3*d* orbitals, still there will be a significant energy splitting due to Coulombic interaction of the *d* block elements with the non-spherical environment. If the energy of the ligand orbital is compatible with the energy of the metal orbital, then they form a net interaction. That interaction forms new sets of orbitals such as bonding and antibonding and each orbital has different energy level. Since ligand field theory considers the bonding in terms energy splitting, it is considered as extended version of crystal field theory. Although crystal field and ligand field have different approaches, both of them underlines importance of *d* orbitals [1,6].

Transition metal compounds are as much interesting as the transition elements. Beyond their magnetic properties, they also possess superconductivity, superhardness and ultraincompressibility etc. Especially transition metal carbides, nitrides and borides are good candidates for forming unique and desirable properties in terms of industrial

usage such as high hardness at room temperature, high melting point, low diffusion coefficients and electric conductivity. Monocarbides and mononitrides of transition metals crystallize in non stoichiometric NaCl type of structure. Since the metal ions are almost twice of the size of non-metal, those can go into the interstitial holes in the metal structure; therefore, it is appropriate to call them as interstitial compounds. In case of transition metal carbides, carbon atoms go into the interstitial positions of face centered cubic structure; however, sometimes they do not occupy every interstitial position. Therefore the structure contains vacancies which are randomly arranged. That random arrangement develops powerful scattering centers for electrons and phonons. Therefore, higher values of vacancies are assumed to be the reason for extreme electrical resistivity of mentioned compounds at room temperatures. In figure 1.2, resistivity values of titanium carbide (TiC) at different carbon ratios are given [7].

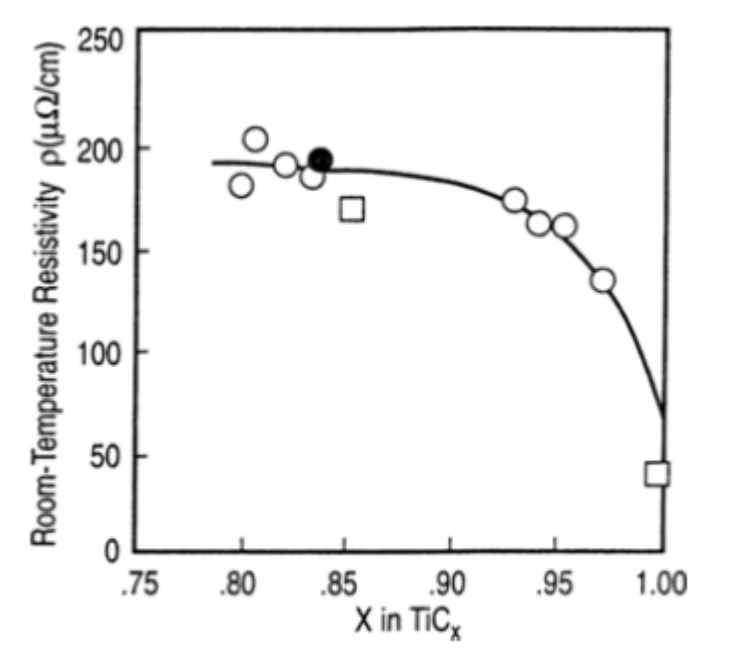

Figure 1.3 The dependence of resistivity on x for TiC_x single crystals

It was shown experimentally that the concentration of the vacancies increases with decreasing carbon content. These vacancies are also directly proportional for the point-defect scattering centers for conducting electrons and their number can be defined as ~ (1 - x). Figure 1.3 denotes that with increasing number of vacancies, the resistivity increases as well. After a certain point as x decreases, resistivity is not increases but saturates and reaches the maximum value with a carbon content of 0.75 and 0.85 in TiC.

Temperature dependence of resistivity is also examined on vanadium carbide. At high temperatures vanadium carbide goes into an ordered structure and because vacancies are distorted, electrons cannot scatter anymore. This trend decreases resistivity dramatically. Transition metal nitrides have similar tendency in electrical conductivity with carbides; however, borides differ dramatically from the nitrides and carbides [7].

Electron 'deficient' configuration of boron with three valence electrons provides interesting bonding properties, such as binding with almost all of the elements in any proportion. Especially with transition metals, they form industrially desired compounds, such as conductor terminals, evaporation chambers, molten metal atomization nozzles, fuel combustion systems, etc [8,9]. Borides of transition metals have high melting points which make them suitable refractory materials. The high melting point is usually accompanied by great hardness and some of them yield superhardness and ultra – incompressibility. Therefore, they have good wear resistance and used as cutting tools and wear–resistant coatings, as well. Since high–speed machining exceeds 1000 ^{o}C, required coating should have high oxidation resistance and borides are stable at high temperatures. Most of the transition metal borides carry good electrical and thermal conductivity which is a desirable property on the agenda of modern electronic device construction [10].

Some properties that make borides more interesting than carbides and nitrides are due to the details of microstructure, defects, crystal structure as a consequence of those the chemical composition. However, their impact degree has not solved yet.

Borides can be classified in three ways, according to the a) occurrence of short boron–boron contacts b) the trigonal prismatic environment of boron and c) transitions from close–packed to open structures.

a) Short boron–boron contacts

Structure formation strongly depends on metal to boron ratio (Me/B). Therefore, boron rich samples form short boron–boron contacts (1.7–1.9 Å) in two dimensions. One example is MeB_2, this type of composition belongs to the category a); however, it is more emphasized in Me_5B_3 and Me_3B_2 type of structures. The possible boron networks and boron arrangements within the crystal lattice are given by figure 1.4 with the Me/B ratio [10]. Ternary compounds may also contain other boron phases.

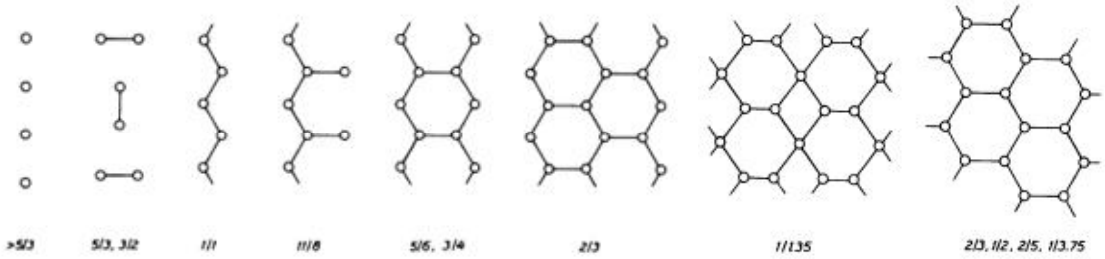

Figure 1.4 Two dimensional boron arrangements according to the given Me / B ratios

Some of the three dimensional boron units were observed with a metal to boron ratio smaller or equal to 0.25. The possible arrangement of boron in the crystal lattice is shown by figure 1.5 [10].

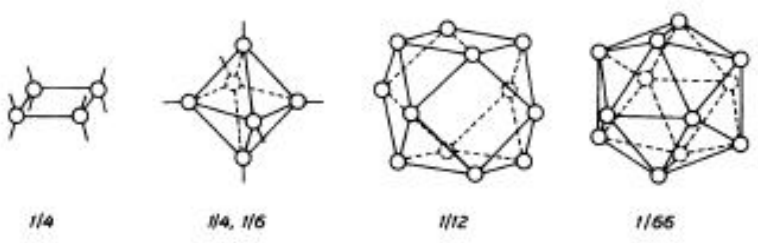

Figure 1.5 Three dimensional boron units with the given Me / B ratios

Trigonal prismatic environment of boron occurs in compounds with a more metal rich composition than MeB_4. Metal atoms distribute themselves at corners and they may also go on to the faces of prism. Carbides and nitrides prefer octahedral symmetry and some exceptional borides such as PtB and Rh_5B_4 also prefer octahedral coordination.

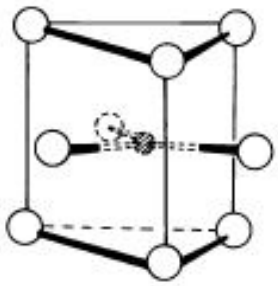

Figure 1.6 Metal atoms arrange themselves around boron in trigonal prismatic coordination.

c) Transitions from close–packed to open structures

Transition from close–packed to open structures occurs when the boron content of the boride increases. This leads to the formation of more boron–boron contacts and also increases the directionality of the boron–boron bonds. As a result, open structures form with low space–filling. This trend is shown on the example of the two compound with different boron content, 73 % space–filling parameter is given for $Nd_2Fe_{14}B$ whereas 40 % is given for YB_{66} [10].

Up to that point, general properties of transition metal borides have been presented. However, the main focus of this study is to investigate the syntheses of ternary transition metal borides with different syntheses method

Chapter 2

2. Ternary Transition Metal Borides

2.1 Introduction

Many technological processes require the improvement on the lifetimes of the materials used. Therefore, hard materials, wear-resistant and thermally stable compounds are highly desired. Ternary transition metal borides are highly promising like binary transition metal borides because usually a ternary compound is a derivative of a binary. Moreover, a binary transition metal boride may be synthesized at high temperatures; however, when it is turned into a ternary, the compound can be synthesized at low temperatures. Figure 2.1 shows the ternary compounds which are derivatives of $CeCo_5$ [11].

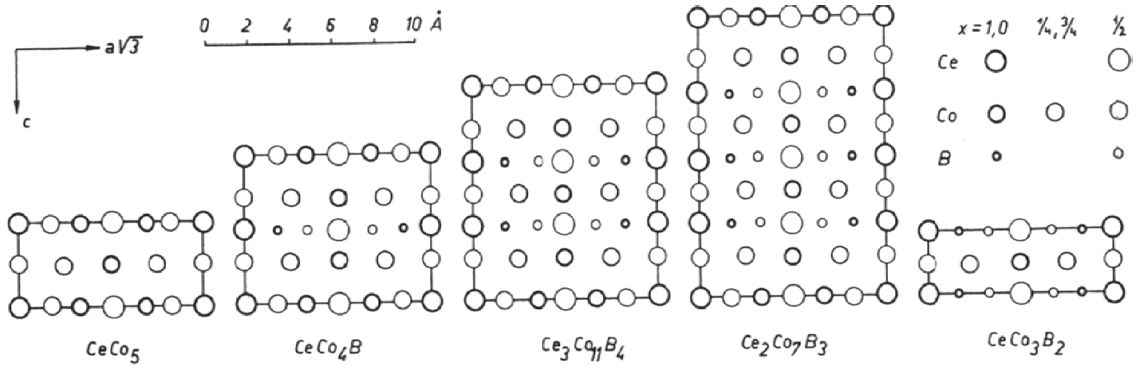

Figure 2.1 Derivatives of $CaCu_5$ – type structure

Unfortunately, there is only few studies available on ternary transition metal borides' structures. As discussed before, ternary transition metal borides also form

boron-boron chains and network structures. Figure 2.2 shows the boron-boron chain formation in the ternaries of Mn_2AlB_2 and MoAlB.

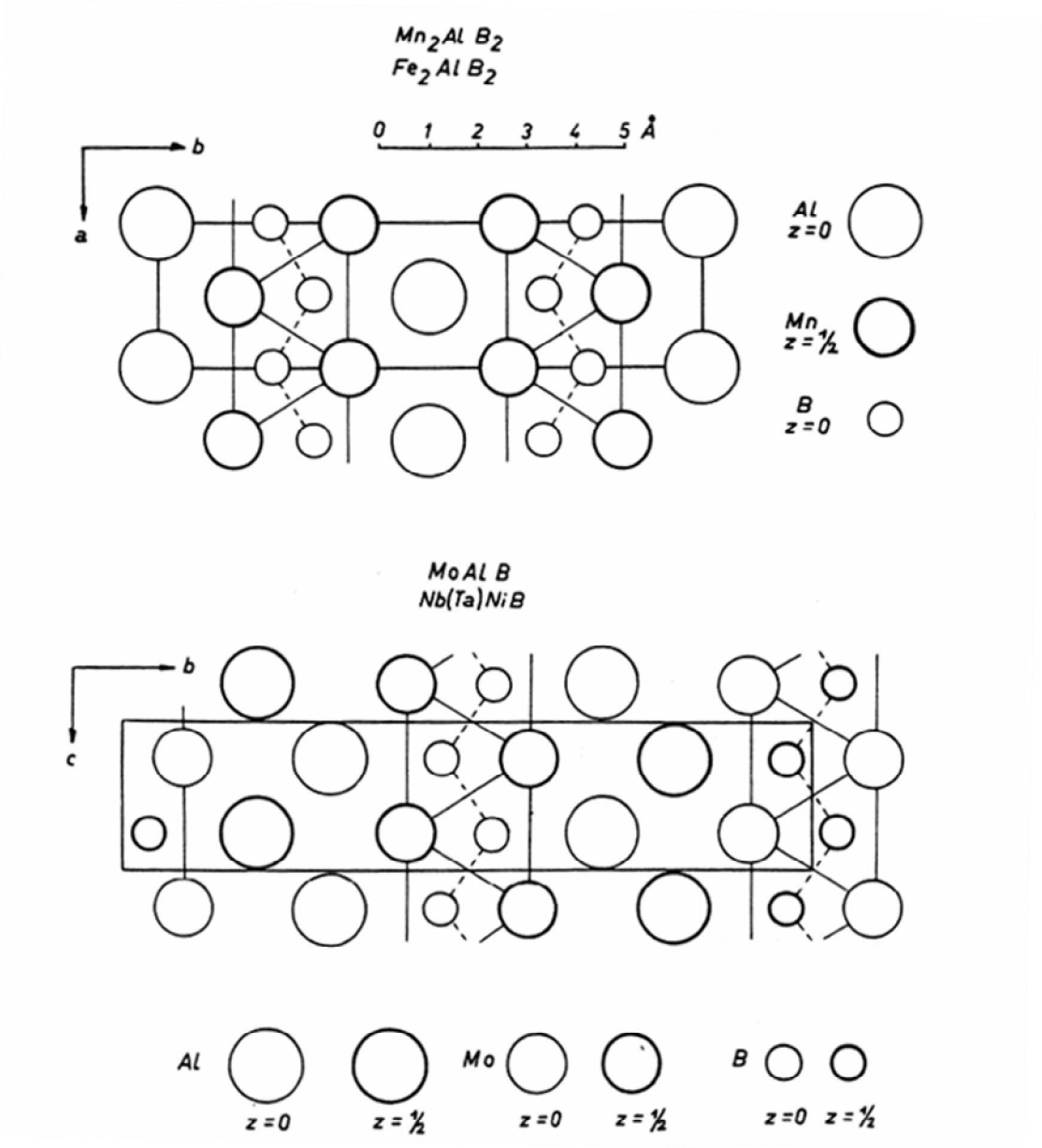

Figure 2.2 Zick-zag boron chains in $MoAl_2B_2$

Boron networks usually observed as 5-, 6- or 7- membered rings; however higher values of rings are also probable as in the case of $CeCr_2B_6$ which has 14-

membered rings of boron. Figure 2.3 illustrates Y_2ReB_6 compound which has all 5-, 6- and 7- membered rings.

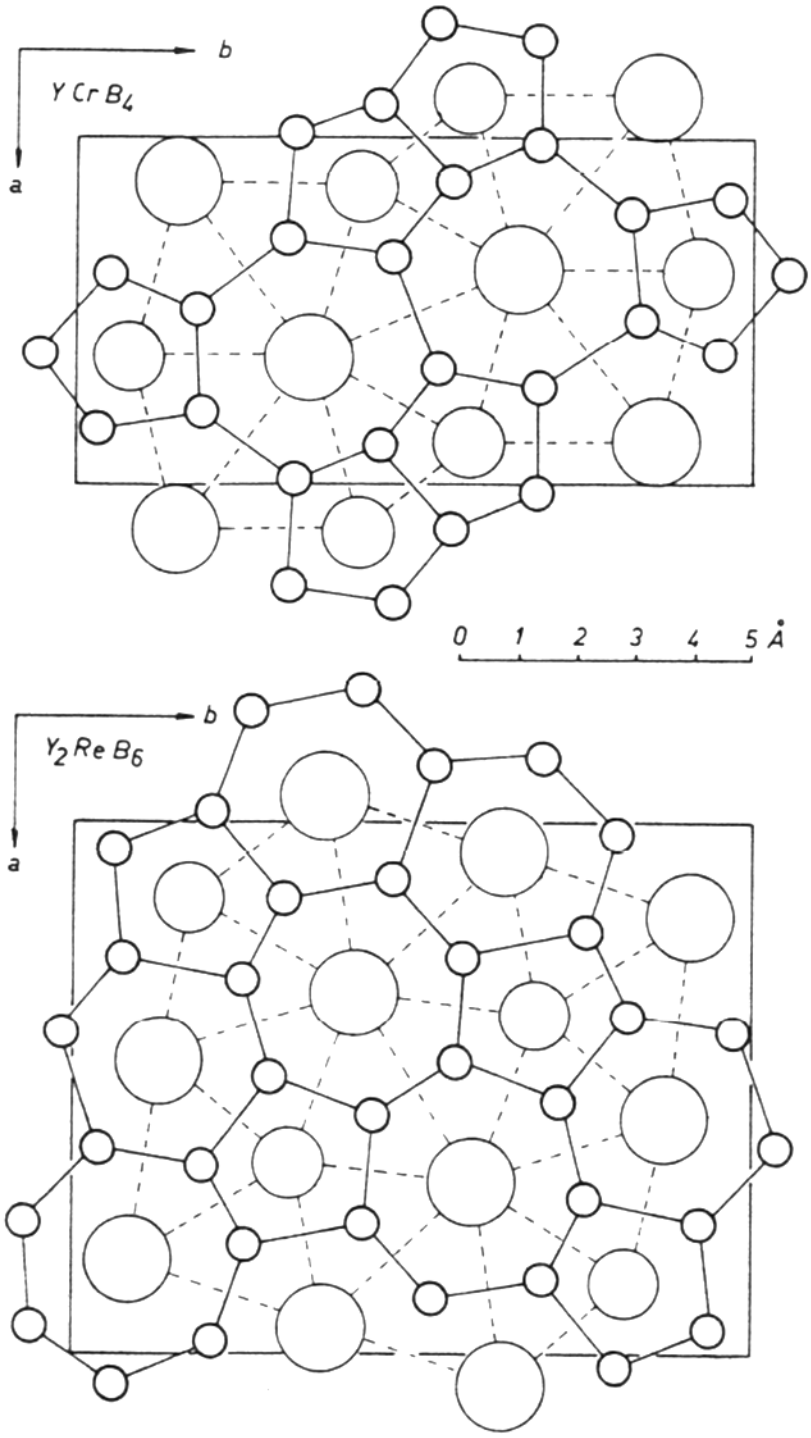

Figure 2.3 5- and 7- membered ring formation in ternary transition metal borides

Ternary transition metal borides can be classified in terms of binaries that represent their structure. *Nowotny* classified the known ternary transition metal borides in terms of structure types, possible formula and representative binary boride .

Table 2.1 Classification of transition metal borides

Structure type	Possible Formula	Representative of binary borides	Representative of ternary borides	Note	Structural elements
Filled ß-Mn	$(M,M')_5B_{1-x}$ $M_3M_2B_{1-X}$	--	$Mo_{\sim 4.5}Re_{\sim 15.5}B_{\sim 2.2}$	--	Metal framework
$Cr_{23}C_6$	$(M,M')_{23}B_6$	--	$Ce_2Ni_{21}B_6$ $Fe_{10\text{-}10\text{-}5}Ir_{13\text{-}7.5}B_6$	Ord. p.ord.	-"-
$W_9Co_3C_3$	$M_9M'_4B$	--	Hf_9Mo_4B	Ord.	-"-
Mn_3Ni_2Si (Ti_2Ni)	$(M_3B)M'_2$	--	Re_3Al_2B	Ord.	-"-
Filled Cu_3Au	$M_3M'B_{1-x}$	--	$Ni_3InB_{0.5}$	Ord.	-"-
W_6Fe_7 (μ)	$M_6M'_7B_x$	--	$Hf_{0.45}Al_{0.5}B_{0.05}$	Ord.	-"-
$MgCu_2$	$M(MB)_2$	--	[Ni, Be] $[Be, B]_2$	--	-"-
Filled Mn_5Si_3	$M_5M'_3B_{1-x}$	--	$Ta_5Ge_3B_{1-x}$	Ord.	Isolated boron
W_5Si_3	$M_5(M'B)_3$	--	$Cr_{\sim 4.5}P_2B$	--	-"-
$Ti_3Co_5B_2$	$(M,M')_4B$	--	$Ti_3Co_5B_2$	Ord.	-"-
Re_3B	M_3B	Re_3B	--		-"-
Filled Re_3B	$M_3B_xC_y$	--	$Cr_3B_{0.2}C_{0.8}$	p.ord.	-"-

Ti_3P	$(M,M')_3B$	--	$Mo_{0.4}Fe_{2.6}B$	--	-"-
Fe_3C	-"-	Co_3B	$Fe_{2.2}Ir_{0.8}B$	--	-"-
Mn_5C_2	M_5C_2	Pd_5B_2	--	--	-"-
Fe_2P	MM'B	--	NbFeB	Ord.	-"-
Ni_2Si		--	MoCoB	Ord.	-"-
NbCoB		--	TaCoB	Ord.	-"-
$CuAl_2$	$(M,M')_2B$ $Mg_2B_{0.5}$	Ta_2B	$V_{0.95\text{-}0.63}Re_{1.05\text{-}1.37}B$	--	-"-
$(BaAl_2)$ Al_2	$(M,M')_3B_2$	--	$LaCo_2B_2$	Ord.	-"-
(Re, Co) $_7B_4$	$(M,M')_7B_4$	--	(Re, Co) $_7B_4$	--	Isolated boron atom
Th_7Fe_3	M_7B_3	Ru_7B_3	--		-"-
$CaCu_5$ and family	$M(M'B)_5$	--	$CeCo_3B_2$ etc.	Ord.	-"-
NiAs	MB	$RhB_{1.1}$	--		-"-
$ThSi_2$	MB_{2-x}	$IrB_{1.1}$	--	Boron deficiency	-"-
WC	MB_{1-x}	IrB_{1-x}(h)	--		-"-
IrB_{1-x}(l)	-"-	IrB_{1-x}(l)	--		-"-
Cr_5B_3	$(M, M')_5B_3$	Cr_5B_3	$Cr_{1.8}W_{3.2}B_3$	--	Boron pairs+ isol. B-atoms
U_3Si_2	$(M, M')_3B_2$	V_3B_2	Mo_2FeB_2 $W_{1.75}Fe_{1.25}B_2$	Ord. p.ord.	Boron pairs

W_2CoB_2	-"-	--	W_2NiB_2	Ord.	-"-
$HfCo_3B_2$ related to $CaCu_5$	$M(M_3'B_2)$	--	$ZrCo_3B_2$	Ord.	-"-
$CeCo_4B_4$	$(M,M')_5B_4$	--	$CeCo_4B_4$	Ord.	-"-
W_3CoB_3	$(M,M')_4B_3$	--	W_3NiB_3	Ord.	B_3 groups
Mo_2IrB_2	$(M,M')_3B_2$	--	Mo_2IrB_2	Ord.	B_4 groups
FeB	MB	CoB	$Cr_{0.67}Os_{0.33}Br$	--	Boron-chain
MoB	-"-	MoB(l)	Re_3CrB_{4-x}	--	-"-
CrB	-"-	MoB(h)	$Hf_{0.2}W_{0.8}B$	--	-"-
MoAlB	$(M,M')_2B$	--	TaNiB	Ord.	-"-
m-Ni_4B_3	M_4B_3	m-Ni_4B_3	--		-"-
Mn_2AlB_2	$(M,M')_3B_2$	--	Fe_2AlB_2	Ord.	-"-
Mo_2BC	M_2BC	--	Mo_2BC	Ord.	-"-
o-Ni_4B_{3-X}	M_4B_{3-x}	o-Ni_4B_{3-X}	--		Boron chains+ isol. B-atoms
$Ru_{11}B_8$	$M_{11}B_8$	$Ru_{11}B_8$	--		
YBC	MBC	--	GdBC	Ord.	Branched chains
UBC	-"-	--	UBC	Ord.	-"-
$W_2Ir_3B_{6-x}$	$(M,M')_5B_6$	--	$W_2Ir_3B_5$ $Mo_{2.5}Ir_{2.5}B_5$	Ord. p.ord.	2-D Networks starting

					from double chain formation
Cr_3AlB_4	$(M,M')_4B_4$	--	Cr_3AlB_4	Ord.	Boron double chains
Ta_3B_4	$(M,M')_3B_4$	V_3B_4	$MoFe_2B_4$	Ord.	-"-
V_5B_6	$(M,M')_5B_6$	V_5B_6	$Cr_2Ni_3B_6$	--	Boron double chains+ boron chains
V_2B_3	$(M,M')_2B_3$	V_2B_3	$VCoB_3$ $Cr_{1.5}Ni_{0.5}B_3$	Ord. --	Boron triple chains
$CeCr_2B_6$	$(M,M')B_2$	--	$CeCr_2B_6$	Ord.	Starting network formation
$IrB_{1.35}$	MB_{2-x}	$IrB_{1.35}$	--		Two dimens. Boron network
$YcrB_4$	$(M,M')B_2$	--	$CeCrB_4$	Ord.	Boron or (B-C) networks
ScB_2C_2 related to $YcrB_4$	MB_2C_2	--	ScB_2C_2	Ord.	-"-
YB_2C_2	-"-	--	GdB_2C_2	Ord.	-"-
YB_2C	MB_2C	--	DyB_2C	Ord.	-"-
Y_2ReB_6	$(M,M')B_2$	--	Y_2ReB_6	Ord.	-"-

AlB_2	-"-	YB_2	--		-"-
ReB_2	-"-	ReB_2	$(W, Ir)B_2$	--	-"-
RuB_2	-"-	OsB_2	--		-"-
W_2B_5	$(M,M')_2B_{5-x}$	W_2B_5 Ru_2B_3	-- --		-"- Network + isol. B-atoms
Mo_2B_5	-"-	W_2B_5	$W_{1.37}Pd_{0.63}B_5$	--	
$Mo_{0.8}B_3$ ($Mo_2B_{\sim 9}$)	$(M,M')_{0.8}B_3$	$W_{0.8}B_3$	--		Network +
Sm_2B_5	M_2B_5	Sm_2B_5	--		Boron framework
YB_4	MB_4	ThB_4	--		-"-
MB_4	-"-	MB_4	--		-"-
CrB_4	-"-	CrB_4	--		-"-
MnB_4	-"-	MnB_4	--		-"-
CaB_6	MB_6	YB_6	--		-"-
UB_{12}	MB_{12}	ZrB_{12}	--		-"-
$MgAlB_{14}$	$(M,M')_2B_{14}$	--	$MgAlB_{14}$		-"-
$ZnB_{\sim 22}$	$MB_{\sim 20\text{-}40}$	$ZnB_{\sim 22}$	--		-"-
$REB_{\sim 100}$	$MB_{\sim 100}$	$YB_{\sim 66}$	--		-"-
. . B					. . Boron

p.ord. = partially ordered
ord. = ordered

In this thesis, ternary transition metal borides of Ta-Co-B, Ta-Ni-B, Ta-Re-B, Nb-Re-B, Hf-Ni-B, Ta-La-B and Re-Ni-B were studied with different stoichiometries. Two different methods were applied and experimental details were given in experimental procedures.

2.2 Experimental Procedures for Ternary Transition Metal Borides

The syntheses methods that were used for binary transition metal borides could be adopted for the syntheses of ternary transition metal borides. There are eight common syntheses types for the binary borides which are given as [2]:

i) Direct Combination of the Elements :

$Cr + nB \rightarrow CrB_n$ at 1150 ^oC

ii) Reaction of the element in molten salts or metals (flux)

$V + nB$ (Al flux) $\rightarrow VB_n$ at 1500 ^oC

$Mg + 2B$ (molten salt) $\rightarrow MgB_2$ at 600 ^oC [12]

iii) Reduction of metal oxide with amorphous elemental boron:

$Sc_2O_3 + 6B \rightarrow 2ScB_2 + B_2O_3$ at 1800 ^oC

iv) Volatile mixed halides are co-reduced with H_2 gas in a metal filament, hot tube or plasma torch:

$2TiCl_4 + 4BCl_3 + 10H_2 \rightarrow 2TiB_2 + 20\ HCl$ at 1300 ^oC

v) BX_3 (X = Halogen) is reduced with a metal or metal/H_2 gas mixture

$nBX_3 + (x + 1)\ M \rightarrow MB_n + xMX_{3n/x}$

$BCl_3 + W \rightarrow WB + Cl_2 + HCl$ at 1200 ^oC with H_2

vi) Reduction of oxides with carbon at high temperatures (≈ 2000 ^oC)

$V_2O_5 + B_2O_3 + 8C \rightarrow 2VB + 8CO$ at 1500 ^oC

vii) Metal oxides are reduced with boron carbide

$Eu_2O_3 + 3B_4C \rightarrow 2EuB_6 + 3CO$ at 1600 ^oC

$7Ti + B_2O_3 + 3B_4C \rightarrow 7TiB_2 + 3CO$

viii) Mixed oxides are co-reduced with metals in a thermite-type reaction

$TiO_2 + B_2O_3 \rightarrow TiB_2$ in a molten Na

In this thesis mainly direct syntheses from elements were performed and two main syntheses methods were preferred. Figure 2.4 illustrates the flow diagram of the methods used.

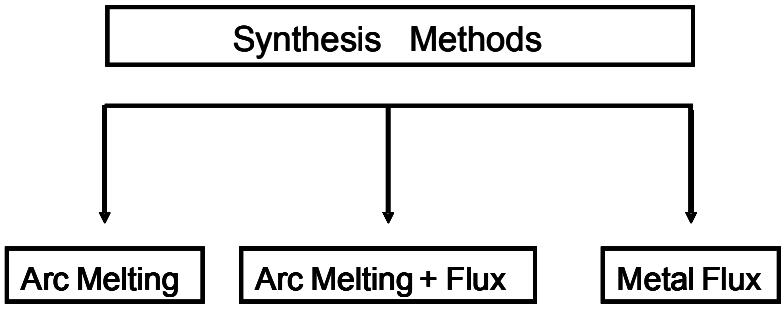

Figure 2.4 Flow diagram of synthesis methods for ternary transition metal borides

1) Arc Melting Synthesis

Syntheses of transition metal borides usually performed at high temperatures (1700 K<) by annealing for long hours. Instead of annealing for long hours, arc melting synthesis could be performed. Arc melting furnace goes up to high temperatures (3000 K<) within a few seconds and cools fast. Due to the reaction conditions, it is hard to obtain single phase. However, if the stability of the compound is high, then, arc melting synthesis saves time and energy. For instance, TaB is synthesized by annealing at 1150 ^{o}C for 150 hours [13,14]. However, arc melting takes only few seconds and that is the reason why arc melting is most employed synthesis tool for a huge number of transition metal borides.

In the present study, the synthesis of the metal borides was accomplished using a home-made arc furnace device (Fig 6.7). The preparation of the metal borides by arc melting process consists of three steps. In the first one, the stoichiometric amounts of powders of the starting elements were measured and placed in an agate mortar. The mixture was grinded for at least 5 minutes until a fine powder was obtained. The sample

was then transferred in a press form of 13mm diameter and pressed to pellet. In a typical reaction batch, a total of 0.5 g of sample was used and 10 kN pressure applied. Lower pressure values resulted in breakage of the pellets. These procedures - i.e. thoroughly grinding of and pressing the powder to a pellet - are helpful to obtain homogenous mixtures and enhance the mutual diffusion of the atoms located at boundary grains so that the solid state reaction can start and proceed fast.

In the last step, the sample pellet is placed onto the copper holder of the arc melting device. The orientation of the pellet occurred in the way as reported for Co_2B, according to which the vertical or tilted positioned pellets yielded better crystallization than the horizontal ones. After placement, the reaction chamber was evacuated to 2-$5 \cdot 10^{-3}$ mbar and refilled with argon. This procedure is repeated several times in order to minimize the contamination by air and moisture.

The inverter welder value was optimized to 50 ampere while the reaction took approximately 20 to 30 seconds to the completion. This procedure was repeated for minimum of three times to achieve an overall homogenization of the products. In order to avoid oxidation, the system was evacuated until the copper plate - i.e. the sample - cooled down to room temperature. Detailed experimental setup of home made arc melting is given in chapter 6.

2) Flux Method

An alternative route for performing high temperature reactions at more moderate temperatures is the flux method. Metal flux preparation technique is based on usage of a low melting and high boiling “non-reactive” metal as solvent for chemical reactions. One of the major barriers in solid state synthesis is the mutual diffusion of the atoms located at boundary grains so that a reaction can start. High temperatures are not always an appropriate tool to overcome this problem and very often specimens must be grinded repeatedly to fine powders to produce “fresh grain surfaces” for reaction to occur. In order to enhance the diffusion process in solids, molten salts or metals (i.e. fluxes) can

be utilized as solvents. This technique is known for more than 100 years in which the liquid may act both as solvent and reactant for intermediate species which may enhance the formation of the final product.

There are four key criteria which must be met by a metal to be employed as flux for reaction chemistry [15]:

1) The metal should form a melt at acceptable low temperatures so that conventional heating equipments and crucible materials can be used,

2) The metal should reveal a broad liquid range (i.e. large difference between its melting and boiling point)

3) The flux metal is expected to be easily removable from the final product by dissolution, filtration etc. and/or by physical methods (e.g. mechanical separation)

4) The metal flux should not form highly stable binary phases with any of the starting components.

The most commonly employed metal fluxes and their uses are [15]:

i) *Tin Flux* is used for binary and ternary phosphides and polyphosphides of rare–earth and transition metals, borides, silicides and further pnictides, binary and ternary stannides.

ii) *Lead Flux* is used for metal rich phosphides and arsenides.

iii) *Aluminium Flux* is used in the synthesis of borides, binary and ternary aluminides and quaternary compounds.

iv) *Gallium Flux* is used in the synthesis of transition metal gallides.

v) *Indium Flux* is used in the synthesis of binary transition metal indium compounds and rare – earth metal transition metal indides.

vi) *Lithium and Sodium Fluxes* are used in the synthesis of industrially important nitrides.

vii) *Zinc Flux* is used in the synthesis of binary stannides.

In this thesis, lead flux was applied for the first time ever for the systematic synthesis of binary and ternary metal borides. Compared to other metal fluxes, molten lead technique had only a limited use in the preparation of intermetallic phases, yet. The few examples are the synthesis of polyphosphides, (e.g. $MPbP_{14}$; M = Zn, Cd, Hg) and some silicides (e.g. $REMn_2Si_2$; RE = Y, Tb, Lu). The most common synthesis route for the transition metal containing borides is the reaction in aluminum flux with which several binary phases, such as V_2B_3, Cr_3B_4, Cr_2B_3, CrB_2, Ta_5B_6, Ta_3B_4, TaB_2, LaB_6 and LuB_4 could have successfully been prepared and characterized until now. An important detail is, that no ternary boride has ever been isolated from molten aluminum, yet, except for those containing Al in their chemical composition, i.e. $LuAlB_4$, $TmAlB_{14}$, etc [15]. Thus, the introduction of lead flux into the preparation tools of - flux-free - binary and ternary borides fills an important gap in the series of those metal fluxes with a high potential to be used universally for the synthesis of all kinds of intermetallic compounds.

The experimental steps followed for the metal flux syntheses are practically the same for each composition. For this purpose, stoichiometric amounts of reacting chemicals were grinded with an agate mortar to a fine powder. In the present study, the metal flux method was used for two purposes: synthesis of new compounds and obtaining qualitatively better crystals or single crystals. For both cases, the experimental steps are practically the same. The powders of the single components or as-prepared binary/ternary compounds were mixed with the most promising metal to form a flux. Usually the ratio of sample to metal varies depending on the class of compound and reaction parameters. For the metal borides in the present work, the value was optimized to 1:10. Alumina was chosen as the most appropriate container material because other crucible materials such as tantalum, niobium etc. might incorporate into the final products and contaminate them. The mixture was placed into the alumina container and the selected flux metal on the top. To minimize the interaction with air, the container was closed with an alumina cap. The closed container was then placed into a silica tube and subsequently transferred into a tube furnace. The reaction was performed under

argon flow. Since the reaction temperature strongly depends on the melting temperature of the metal flux used, the heating treatment had to be optimized for each compound. In a typical reaction batch, the sample was heated up to 1073 K, annealed for 5h and rapidly cooled down to room temperature. When the reaction was done, the alumina crucible with its content was boiled in 70% hydrochloric acid (HCl) until no bubbles were observed. The remaining powder - i.e. the final product - was washed several times with hot distilled water for the complete removal of $PbCl_2$. The reaction taking place is as follows:

$$Pb\ (s) + 2HCl\ (aq) \rightarrow PbCl_2\ (s) + H_2\ (g)$$

Lead (II) chloride is very good soluble in hot hydrochloric acid and water. The in HCl_{conc} insoluble final product - binary or ternary metal boride of gray or metallic color - is not sensitive to air and moisture. The experimental setup for metal flux reaction is illustrated in Figure 2.5.

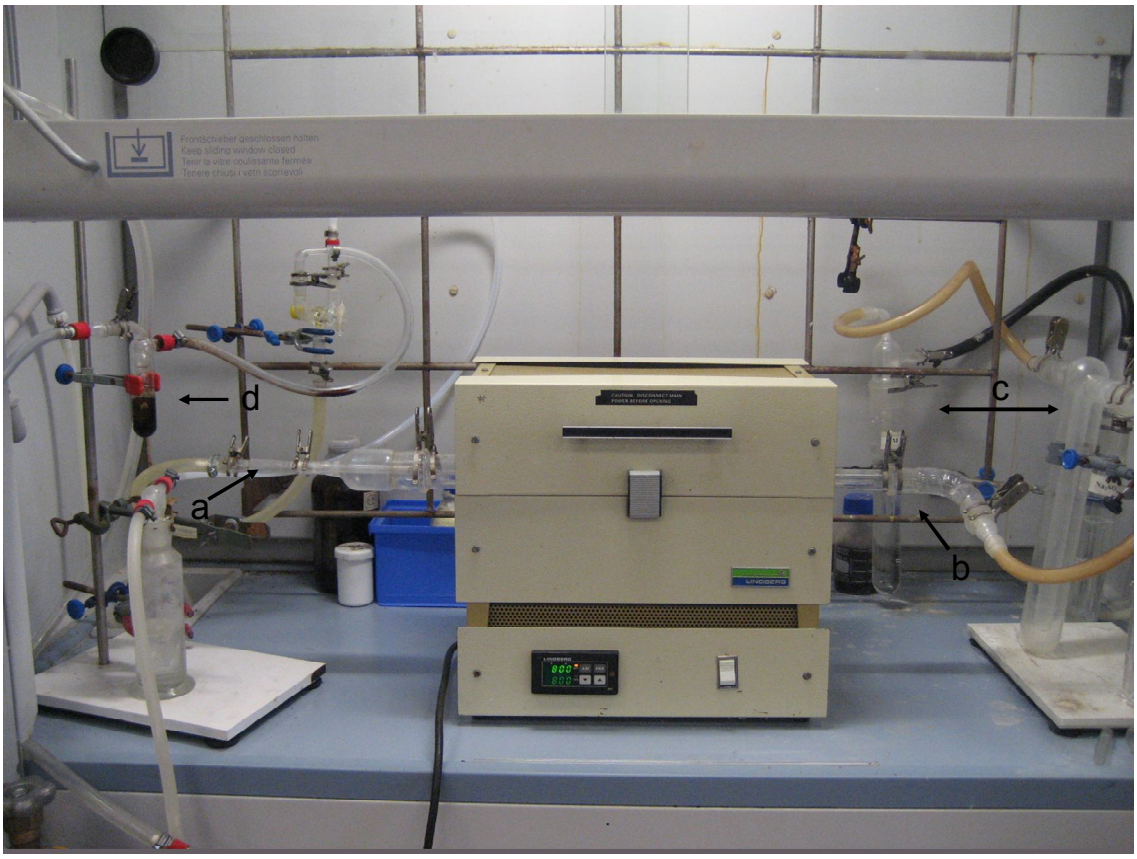

Figure 2.5 Experimental setup for Metal Flux reaction **a)** argon gas inlet; **b)** gas purge; **c)** gas traps; **d)** Sulfuric acid bubbler

2.3 Results and Discussion on Ternary Transition Metal Borides

Formation of new materials is based on interaction of the chemical components. In this sense, phase diagrams are universal source of information about multicomponent systems. This holds for a great number of binaries, among other also borides, while the respective ternary phase diagrams are only poorly studied. Main reason might be that their formation requires very high temperatures. Although arc melting is the method of choice for many of the high temperature syntheses, its application implicates some difficulties in terms of temperature control and reaction time. Furthermore, a good crystallization usually requires annealing, slow cooling etc. in order to achieve the thermodynamic equilibrium. In many cases, reactions from stoichiometric ratios are not feasible, because of the evaporation loses of some elements due to extreme high temperatures that are formed during the arc melting process.

In this thesis, ternary systems of Ta-Co-B, Ta-Ni-B, Ta-Re-B, Nb-Re-B, Hf-Ni-B, Ta-La-B and Re-Ni-B were studied using the arc melting technique. Except for the Re-Ni-B system, all products were phase mixtures of ternaries with already well-known binaries. Therefore, Re-Ni-B system was further investigated with flux method, too.

2.3.1. Ta-Co-B and Ta-Ni-B Ternary Systems

According to *Inorganic Crystals Structural Database (ICSD)*, the only known compound within the system of Ta-Co-B is $Ta_2Co_{21}B_6$. The phase was synthesized by annealing of the as-prepared ingot - from arc melting process - for long hours. Similarly, the only existing ternary in the Ta-Ni-B system is reported to be $TaNiB_2$ which was obtained via annealing at high temperature (~1673 K) [17]. In the present study, Ta-Co-B and Ta-Ni-B systems were reinvestigated by using the arc melting

method. Figure 2.6 displays the studied stoichiometric mixtures within the ternary Ta-Co-B system.

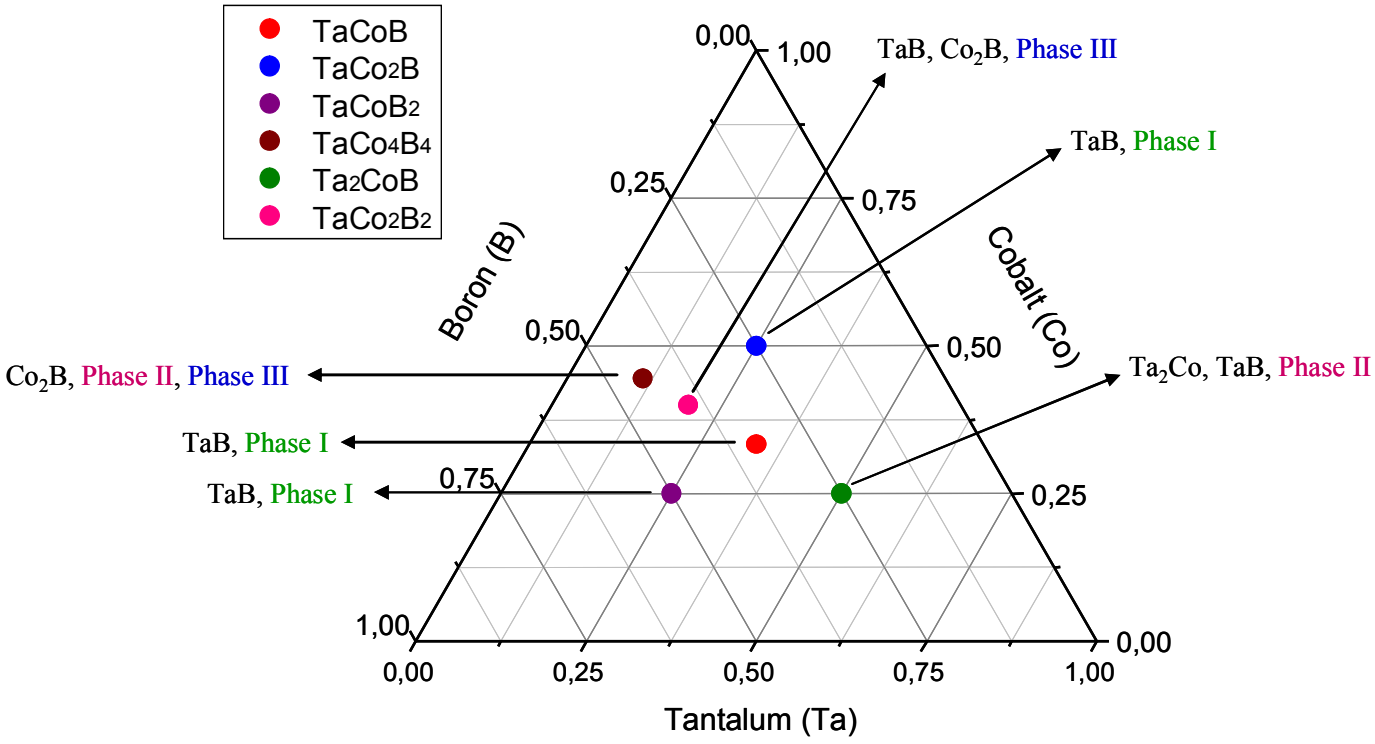

Figure 2.6 Ternary phase diagram of Ta-Co-B system

The synthesis attempts for a new Ta containing ternary boride ended up with formation of TaB and a new phase. While tantalum excesses initialized the formation of tantalum binaries, cobalt and boron surpluses counteracted the formation of TaB, but yielded Co_2B and a foreign phase. However, reported $Ta_2Co_{21}B_6$ or a new single phase could not be detected

Ta-Ni-B system culminated in two new phase mixtures consisting of one or more binaries. Figure 2.7 presents the different stoichiometric ratios of the studied samples within the Ta-Ni-B system. As for the ternary Ta-Co-B, tantalum excess resulted in the formation of TaB with Ta surplus. Nickel excess increased the formation of Phase I; however, boron excess ended up with formation of several binaries and

Phase II. Nickel and boron excess resulted in TaB, Ni_2B and formation of Phase II, while a new single phase or the reported $TaNiB_2$ could not be detected.

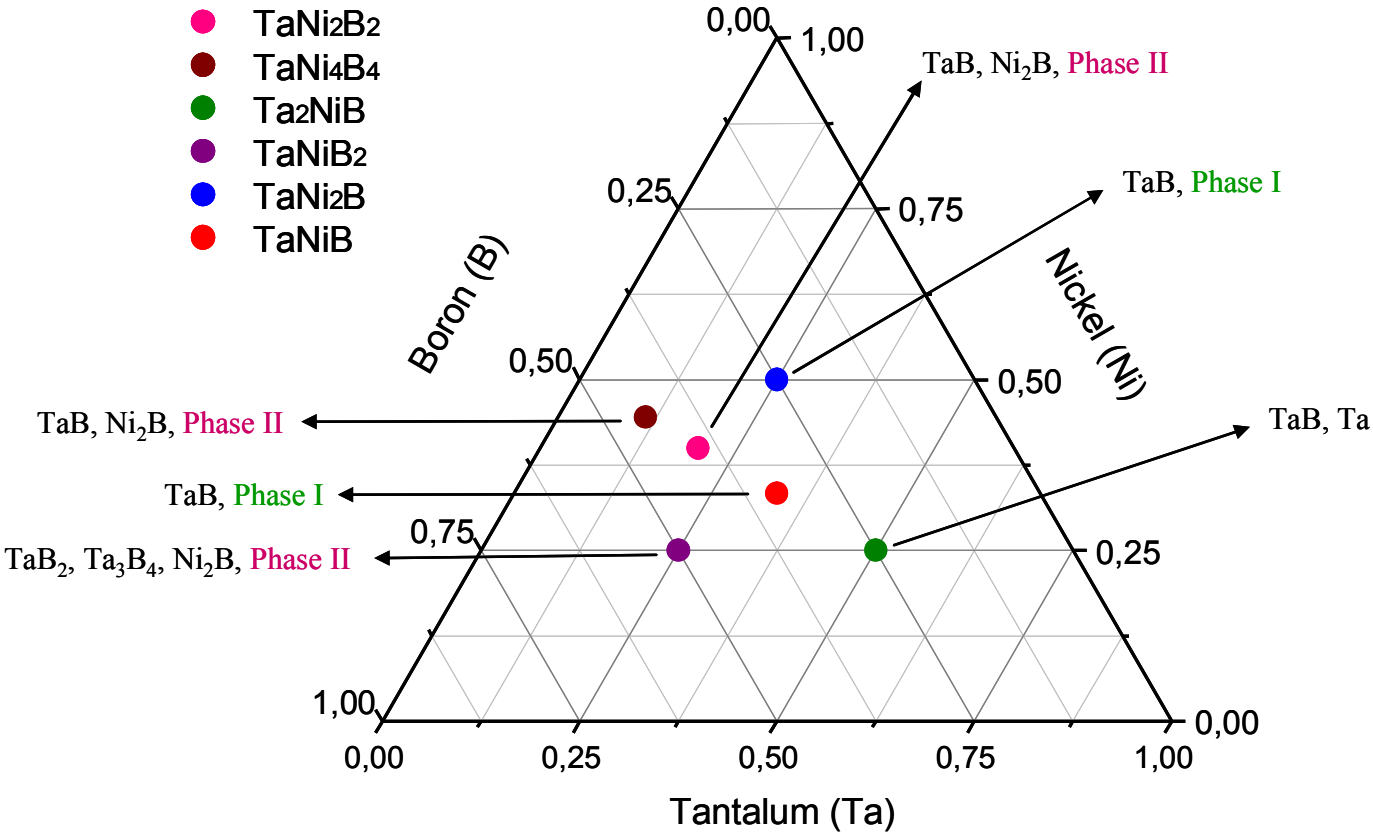

Figure 2.7 Ternary phase diagram of Ta-Ni-B system

Thus, the synthesis in both ternary systems failed to yield any single phased product ever. Arc melting synthesis is a suitable method for high temperature syntheses binaries. On the other hand, preparations aiming a ternary compound are often accompanied by formation of highly stable binaries. Phase diagrams of possible binary compounds were given in appendix A.3, A4 and A5. Arc melting synthesis exceeds 4000 K and in case of Ta-Co-B and Ta-Ni-B systems, upon cooling TaB is the first compound formed (~3363 K) being a highly stable binary. Hence, both ternary systems

nestle TaB in almost each synthesis. Different strategies were followed in order to prevent the TaB formation in preference of a single ternary phase. Ta powder was dissolved in NiB binary; however, the final product did not differ from the direct reaction from the elements. In a different experiment, Tantalum wire in combination with binary NiB was used instead of Ta powder in order to minimize its reactivity. Formation of ternary phase was expected on the wire; however, it again ended up with the binary TaB. To eliminate the unpleasant presence of binaries in favor of a single ternary phase, annealing is a highly recommended tool. The tempering process will help to achieve a better diffusion and enhance the dissolution of an additional element in the formed binary compound so that a ternary can be generated.

The result of the arc melting studies showed that Ni and B excess supports the formation of a new phase. On account of this information, $TaNi_4B_4$ system was studied with annealing as well at two different T_{max} values. The lower one at 1373 K ended up with Ni_3B binary and unidentified phase, while tempering at 1773 K resulted in a single ternary phase. Figure 2.8 compares the X-ray diagrams at 1373 K and 1773 K.

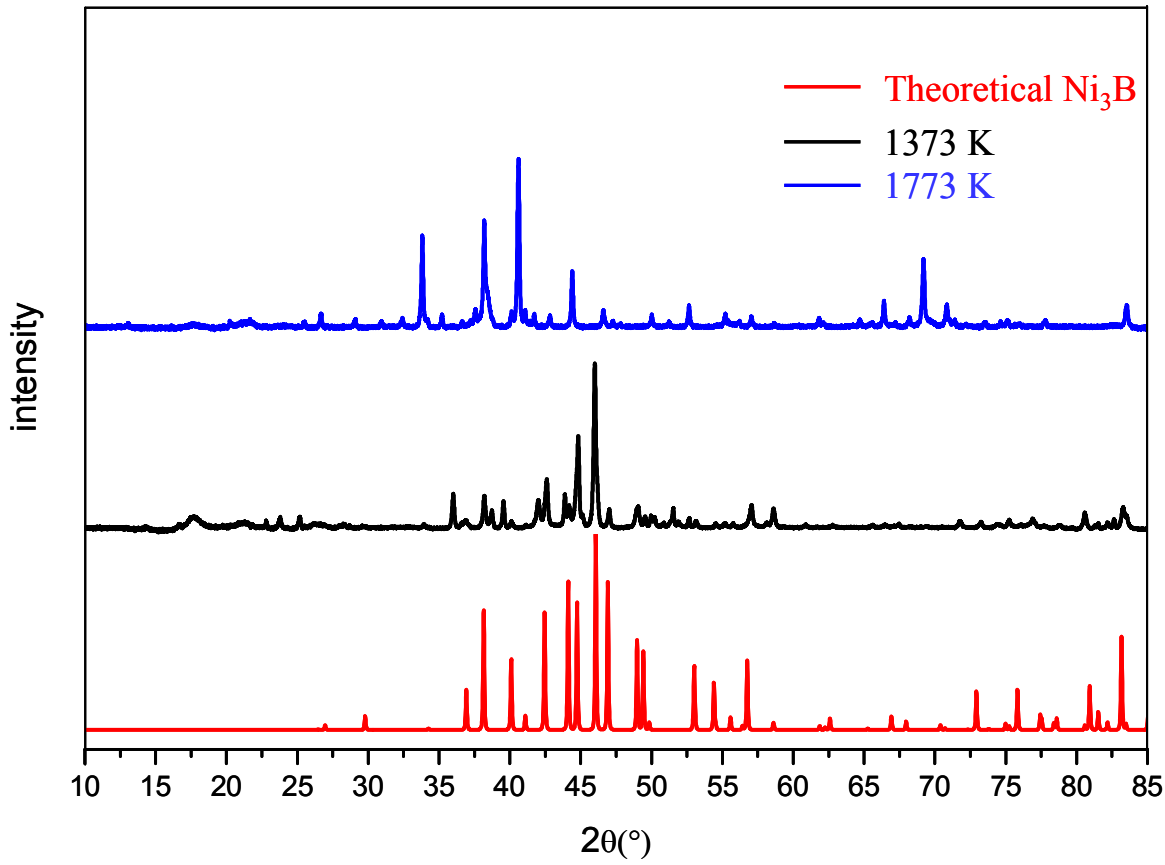

Figure 2.8 X-ray powder diagrams of samples synthesized at 1373 K and 1773 K.

Unfortunately, due to the lack of suitable single crystals the crystal structure of the compound could not be solved, yet.

2.3.2. Ta-Re-B and Nb-Re-B Ternary Systems

In 1971, the first ternary compound, $Ta_3Re_3B_4$, was synthesized via annealing at 1673 K. It crystallizes in the tetragonal system and is a derivative of U_3Si_2, in which Si is replaced by B and half of the U positions are statistically occupied by Ta and Re each

[18]. In this thesis, instead of annealing for long hours, arc melting was the synthesis method of choice. The formation $Ta_3Re_3B_4$ was accompanied by a new phase. Thanks to our systematic investigations, a new monophase compound could be obtained. Tantalum and niobium have the same atomic radii of 1.45 Å and similar electronegativity values. Hence, one can expect, that these two elements may substitute each other easily. Based on the given informations, the novel ternary compound should the derivative of the ternary Ta boride with the composition $Nb_3Re_3B_4$. As in the case of $Ta_3Re_3B_4$, it is accompanied by formation of a new foreign compound. Figure 2.9 compares the two compounds with the theoretical data.

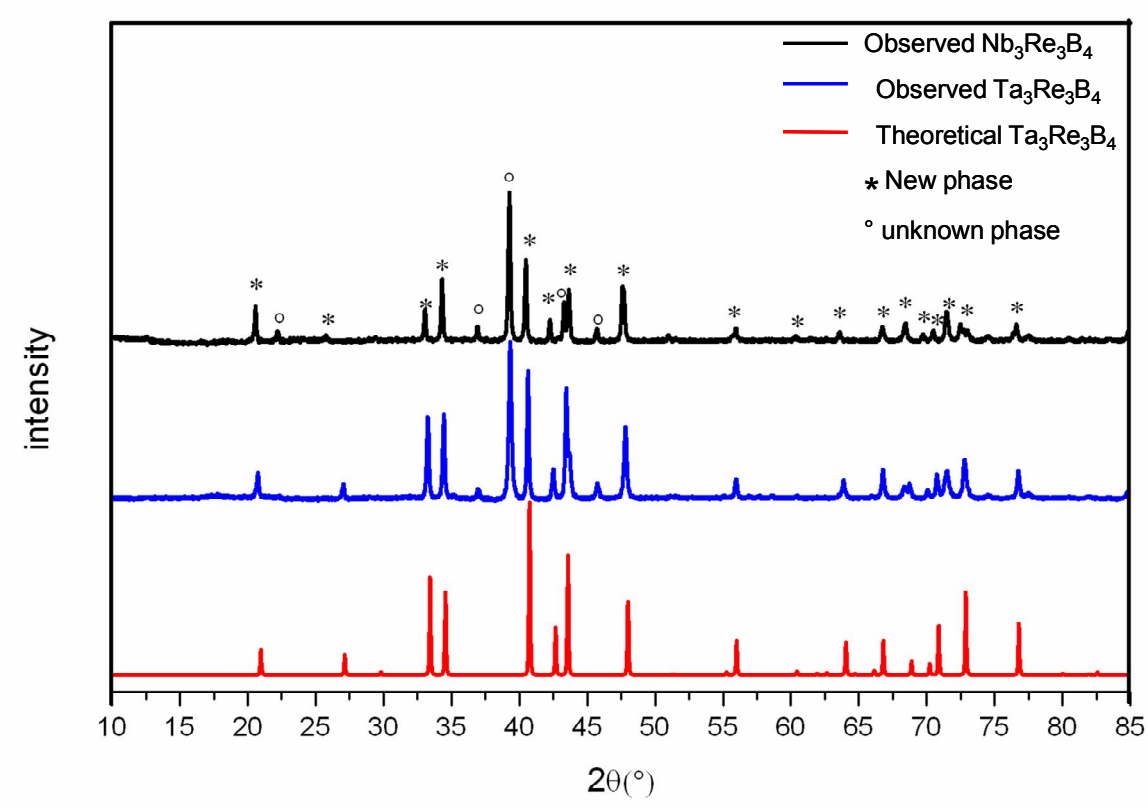

Figure 2.9 X-ray powder diagram compares $Ta_3Re_3B_4$ and $Nb_3Re_3B_4$ with the theoretical data

2.3.3. Hf-Ni-B Ternary System

Hf-Ni-B system was first investigated in 1972 by annealing at 1673 K; however, no results on the existence of any ternaries have been available up to now [19]. For this purpose, Hf-Ni-B system was reinvestigated using the arc melting as preparative tool again. Formation of a new phase was observed on the hafnium excess regions of the phase diagram; however, a pure single phase product could not be isolated yet. Figure 2.10 depicts the constructed phase diagram for Hf-Ni-B and the compounds detected within the ternary system.

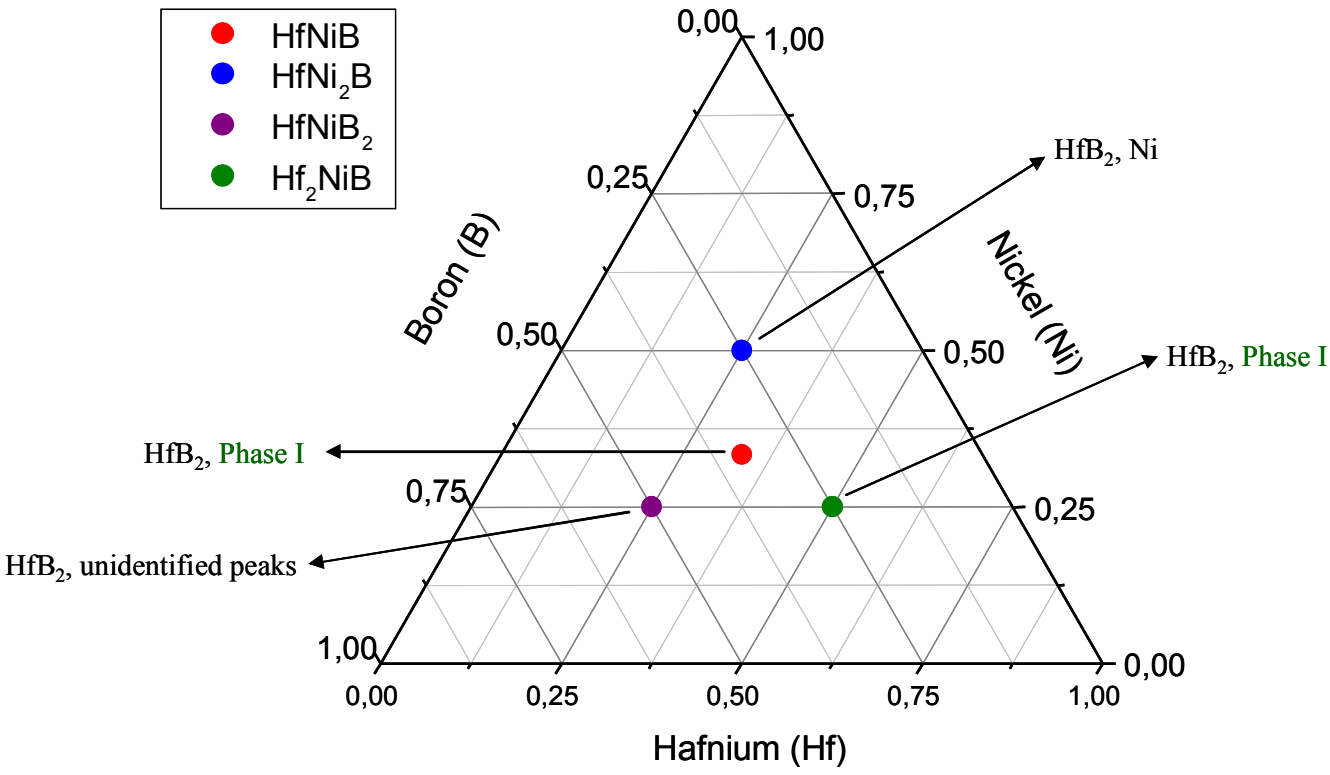

Figure 2.10 Hf-Ni-B ternary systems with arc melting synthesis

HfB_2 formation reaches its maximum when the molar ratio of Hf/Ni/B = 1:1:1. Even the slightest deviation from this composition resulted in formation of HfB_2 which is in good accordance with its high thermodynamic stability. To obtain a ternary phase, hafnium excess regions should be re-investigated. Also, annealing may improve the diffusion rates and enhances the thermodynamic equilibrium. The respective X-ray powder diagrams are represented in appendix A.7.

2.3.4. Ta-La-B Ternary System

LaB_6 is an air stable compound with a formation temperature of 2988 K. Phase-pure LaB_6 was commercially purchased and its solid state reaction with tantalum was investigated using the annealing method. Two different annealing programs were performed with tempering time of 72 h at 1173 K and 1573 K, each. 1173 K was obviously not sufficient enough for the initiation of the reaction; however, for 1573 K the powder diagram shows the clear evidence for the formation of a new phase. Figure 2.11 displays the relevant stoichiometric mixtures and the detected compounds.

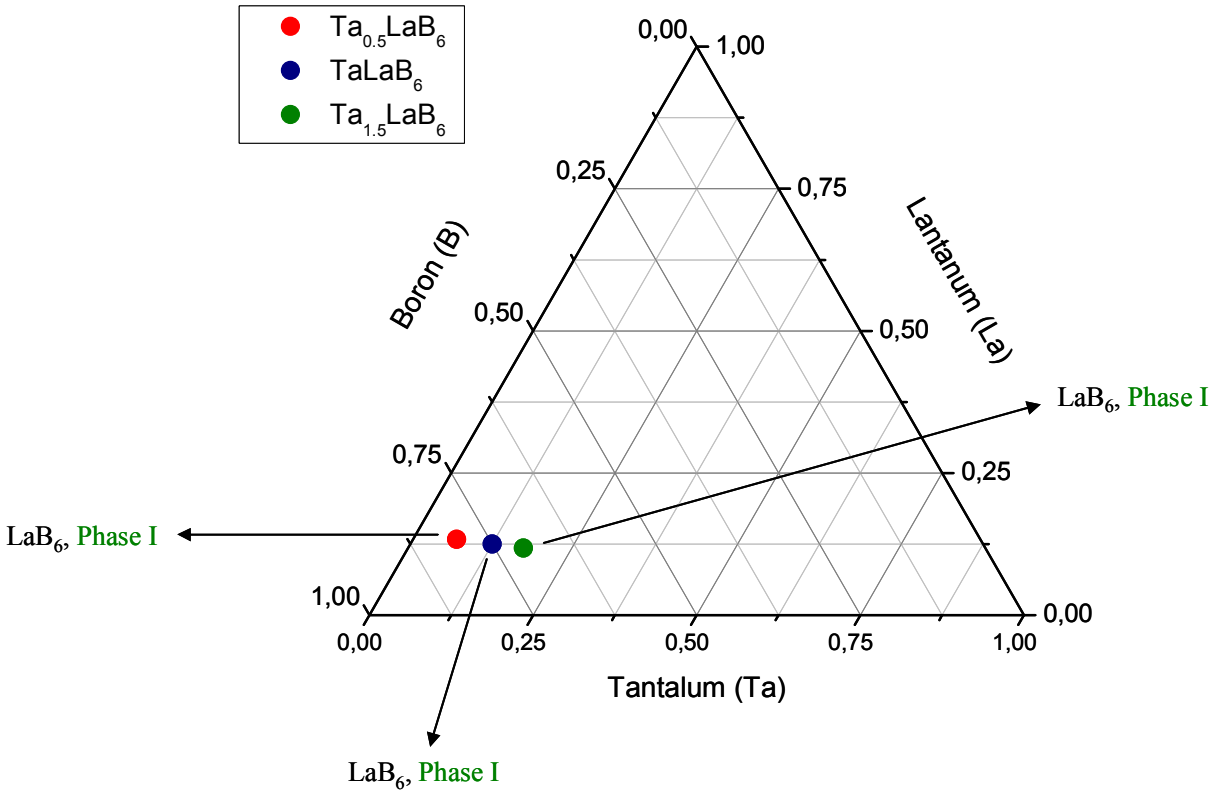

Figure 2.11 Studied ternary system of Ta-La-B by annealing at 1573 K

Figure 2.12 displays the X-ray powder diagrams of the compounds and it is clear that by increasing the tantalum concentration, the formation of the new phase increases dramatically, too. Major peaks from the new phase were assigned and indicated on the diagram. For further studies, tantalum excess regions of the phase diagram should be investigated with the aim of the isolation of the new ternary as single phase.

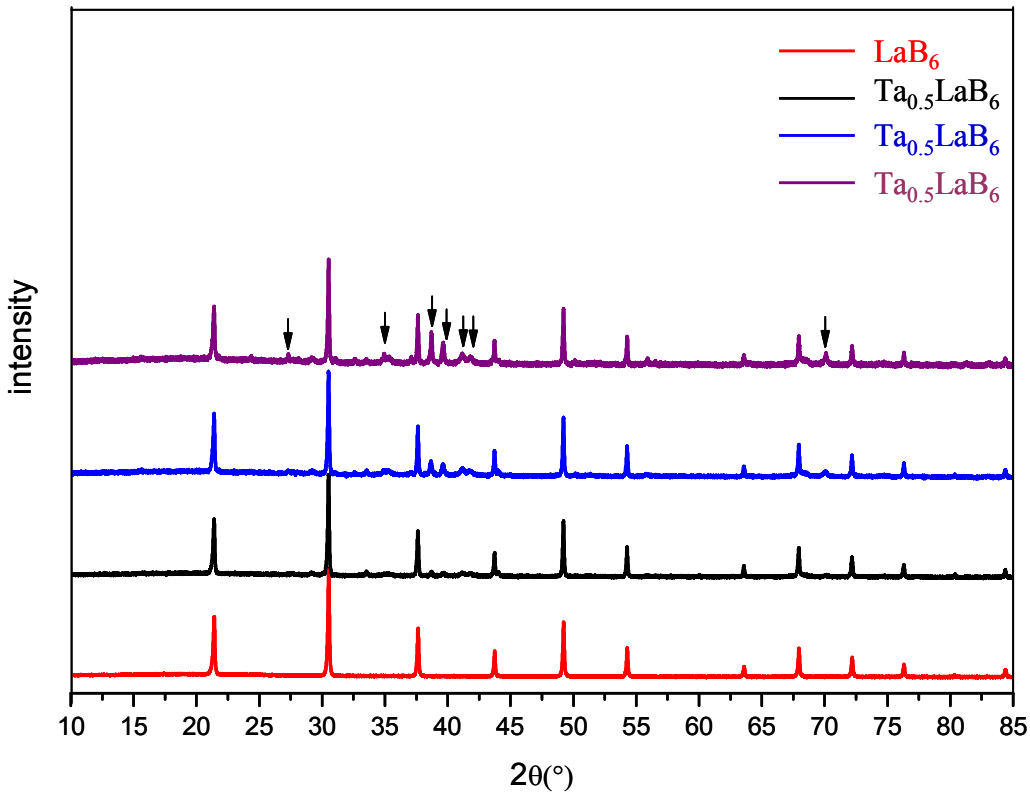

Figure 2.12 X-ray powder diagram of Ta-La-B system

2.3.5. Re-Ni-B Ternary System

Especially after the discovery of the property of superhardness for ReB_2, Re containing borides moved to the center of interest even though the abundance of this element in nature is limited and the price high. Rhenium is known to change the performance of the materials significantly. Ternary systems of rhenium and nickel with other transition metals are known [20]. However, their reaction with boron has not been investigated, yet.

In this thesis, the ternary Re-Ni-B system was studied both by employing arc melting and flux as synthesis routes. Prior to use of lead flux, aluminum flux was also applied. The latter resulted in formation of $Al_3B_6Ni_{20}$ while rhenium remained

unreacted. Figure 2.13 displays the "wonderful" crystals obtained from aluminum flux synthesis. Although the product was obtained by accident, the method is well suitable for the aimed synthesis $Al_3B_6Ni_{20}$.

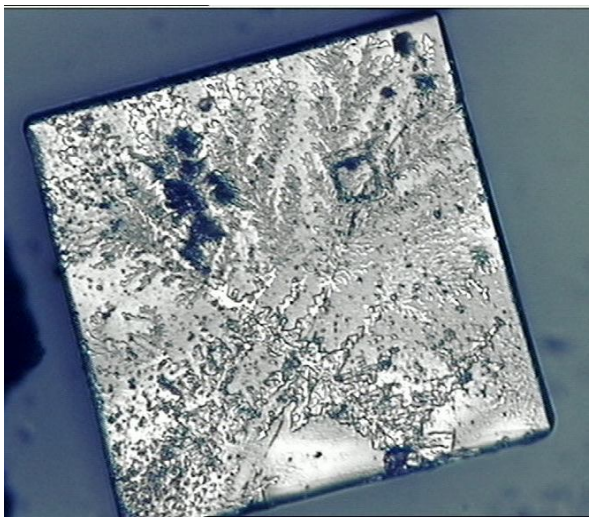

Figure 2.13 $Al_3B_6Ni_{20}$ crystals obtained from Re-Ni-B synthesis in Aluminum flux (20x magnifications)

Successful preparation of Re-Ni-B ternary phase was achieved with lead flux. To exclude any contamination from lead, EDX and ICP-OES measurements were performed. The results confirm the absence of lead in the samples (Figure 2.14).

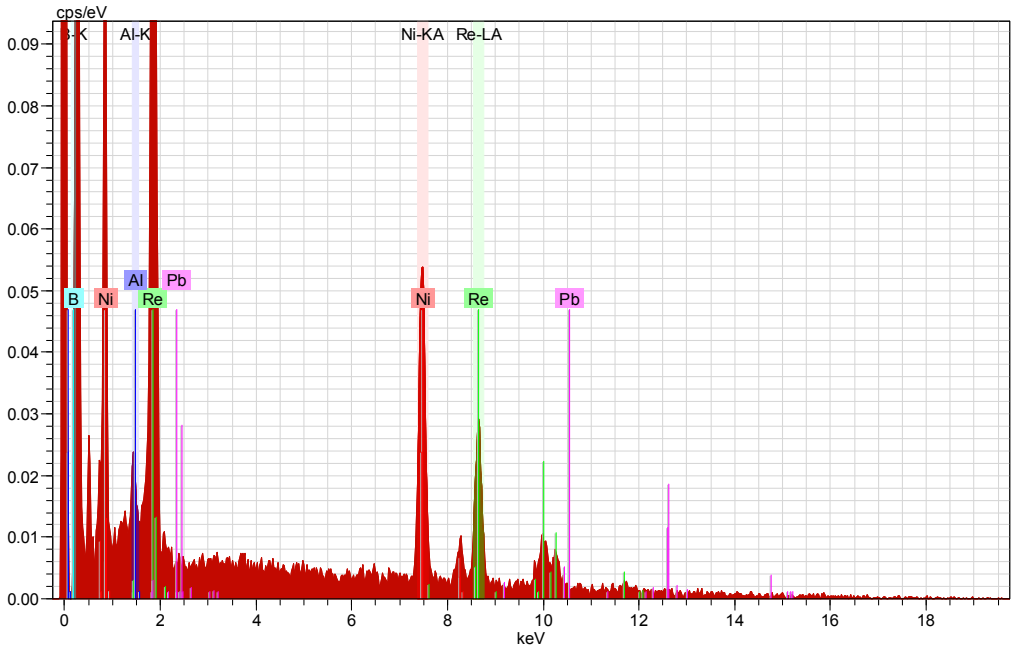

Figure 2.14 The result of the EDX measurements of a Re-Ni-B sample synthesized in lead flux

Boron is difficult to detect by EDX; therefore, WDX measurements were performed in order to calculate the approximate composition of the ternary compound. Aluminum contribution in the EDX measurements results from the device.

Arc melting and flux syntheses yield both the same final product. Since arc melting is less preferable for the single crystal growth, arc melting and flux techniques were combined. The as-prepared samples from arc melting were powdered and re-crystallized in lead flux. However, this procedure did not effect the crystallization, markedly. Most probably, the obtained compound was already in equilibrium. Arc melted and flux-grown samples were compared in figure 2.15.

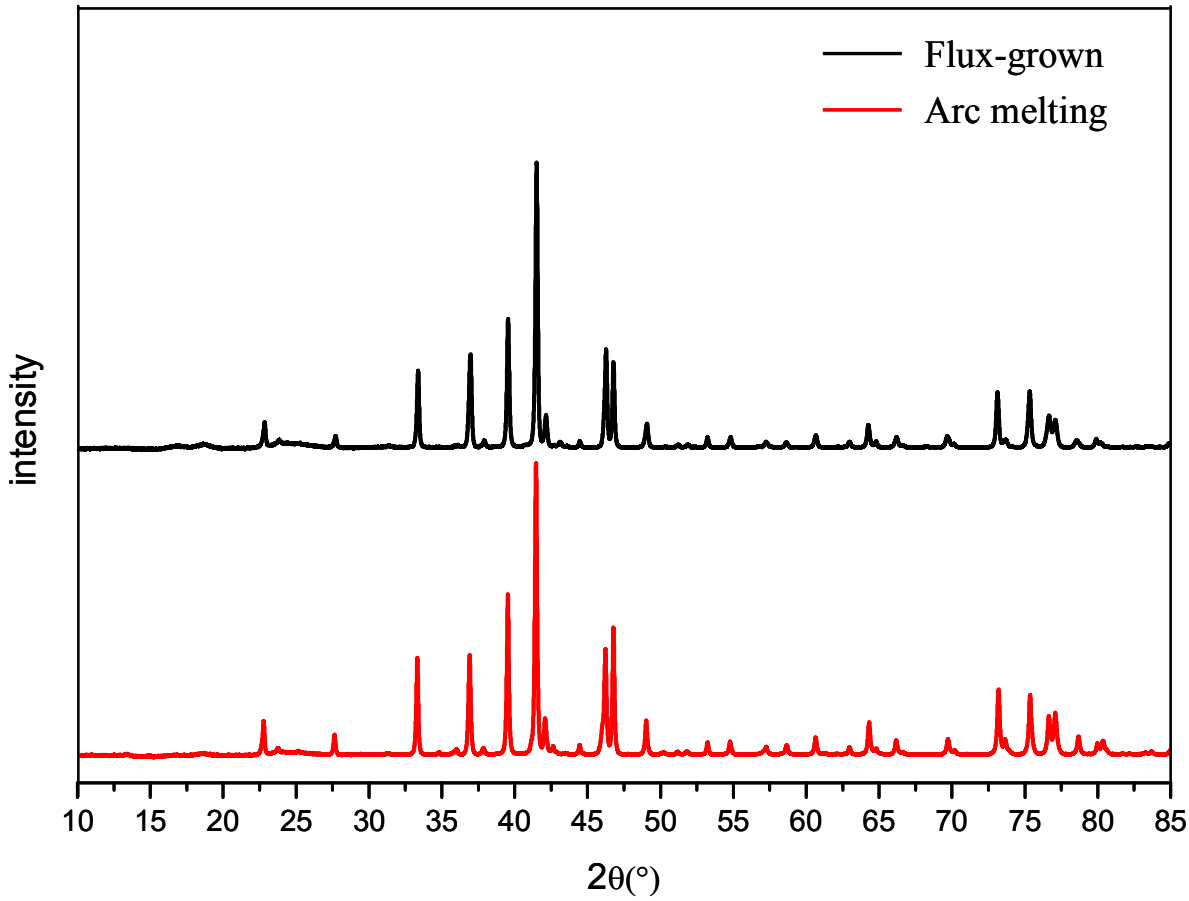

Figure 2.15 Comparison of the syntheses methods for the "Re-Ni-B compound" by arc melting and lead flux

SEM images were collected from the arc melted sample. Nickel and rhenium distributions were studied. Figure 2.16 displays 2000 µm magnification and figure 2.17 displays the nickel and rhenium distribution on the sample.

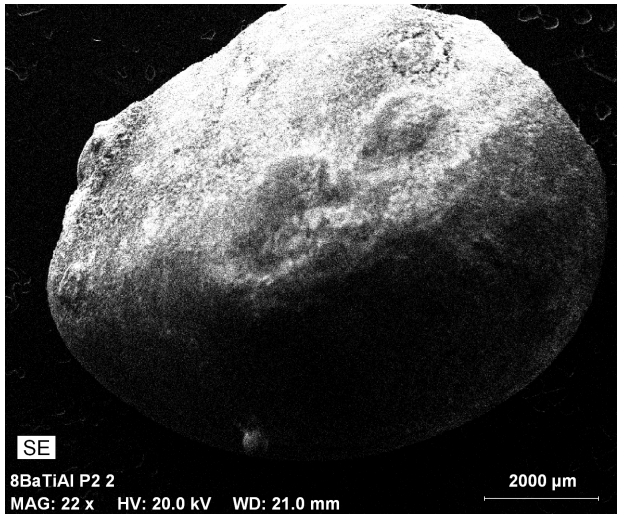

Figure 2.16 SEM image of Re-Ni-B ingot

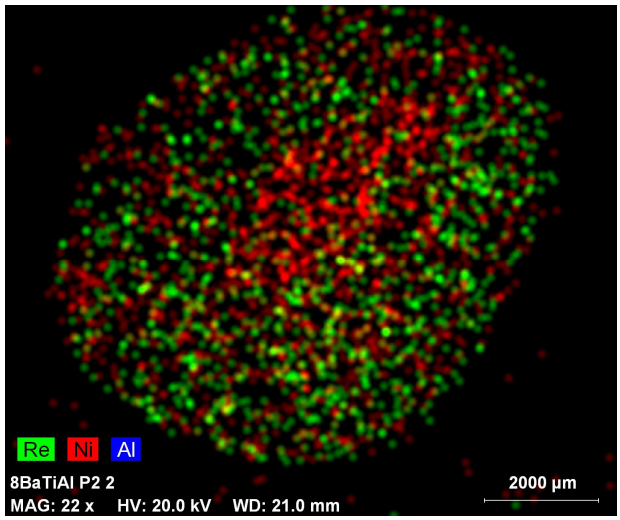

Figure 2.17 Rhenium and nickel distribution on Re-Ni-B ingot

The Fig. 2.17 shows that the distribution of rhenium and nickel (figure 2.17) on Re-Ni-B ingot is not homogeneous. Microstructure analyses help to interpret inhomogeneity. These were performed with a polished sample embedded into an epoxy resin. Optical microscope images and back-scattered electron micrographs were

collected. Figure 2.18a, b, c display optical microscope images at different magnifications of 1 mm, 100 µm and 50 µm, respectively.

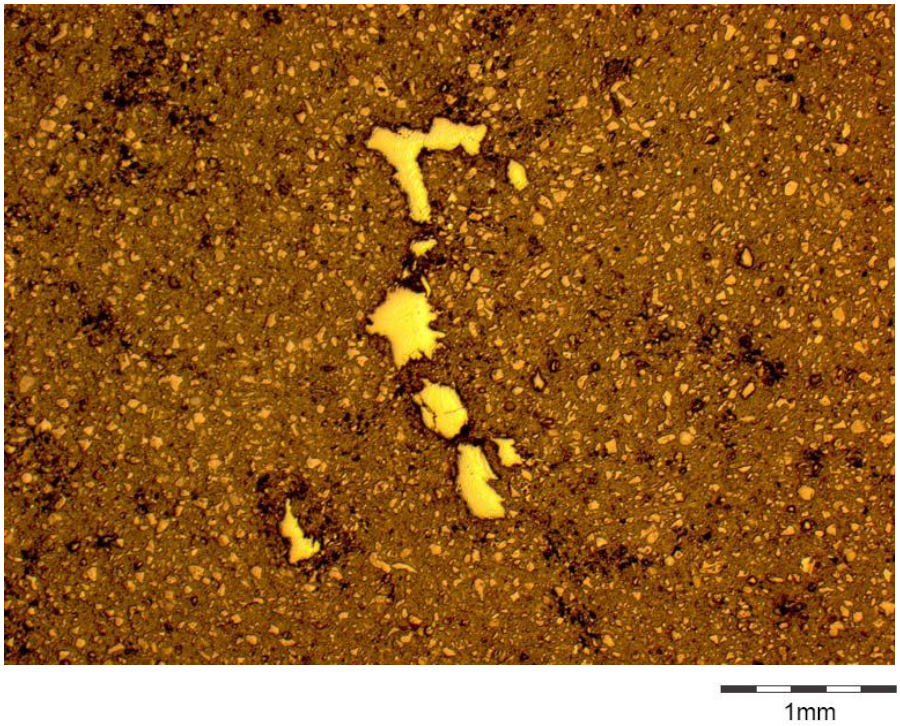

Figure 2.18 a) Optical microscope image of Re-Ni-B at 1 mm magnification

Polished sample is embedded into epoxy resin. Brown region belongs to epoxy resin and shiny part belongs to Re-Ni-B compound.

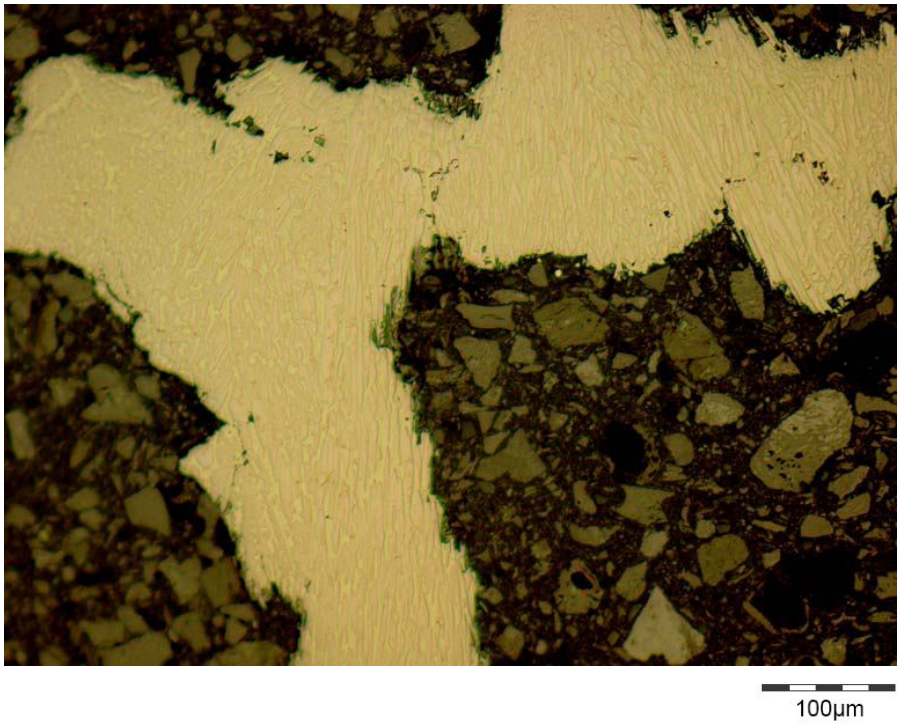

Figure 2.18 b) Optical microscope image of Re-Ni-B at 100 µm

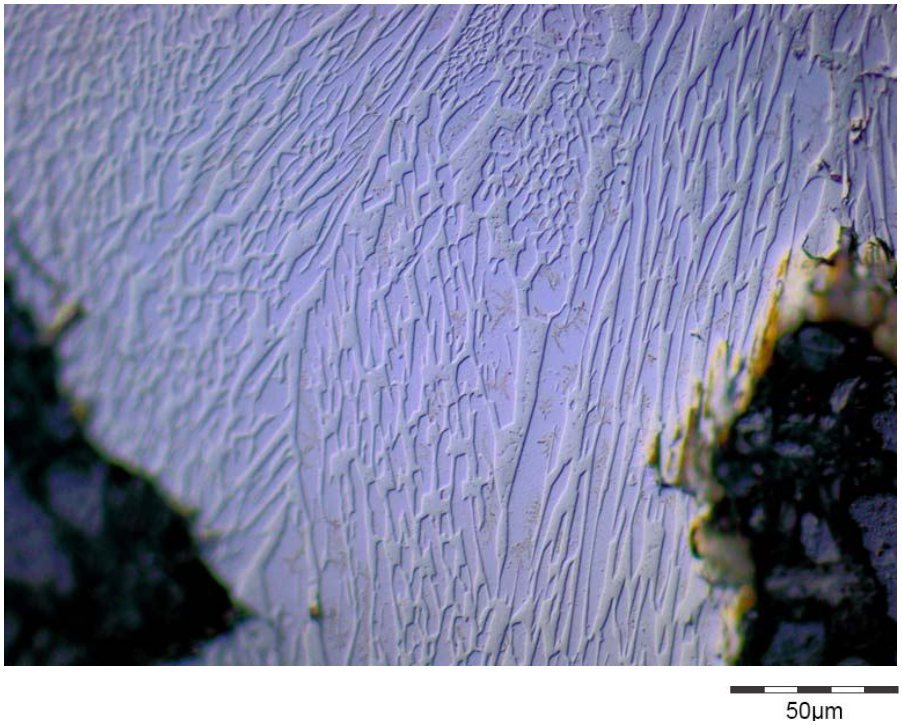

Figure 2.18 c) Optical Microscope image of Re-Ni-B sample at 50 µm

Grains are visible in figure 2.18 c. But, the coexistence of different phases could be better investigated by back-scattered electron micrographs. With this technique two different phases were detected; the one being shiny and the other one of dark color. Figure 2.19 illustrates the optical images from those two different phases. EDXS measurements were performed to investigate the contribution of each element to the two phases. According to the results, the shiny phase turned out to be rhenium and dark phase nickel rich, respectively. Figure 2.20 and figure 2.21 displays the EDXS measurements from rhenium and nickel rich phases.

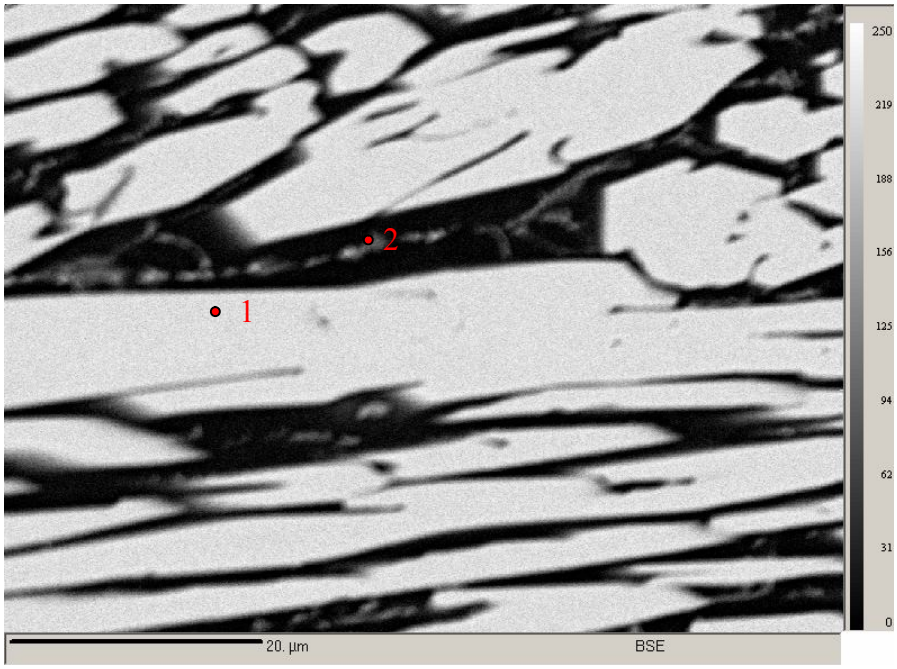

Figure 2.19 Back-scattered electron micrograph of "Re-Ni-B" which shows the coexistence of two different phases

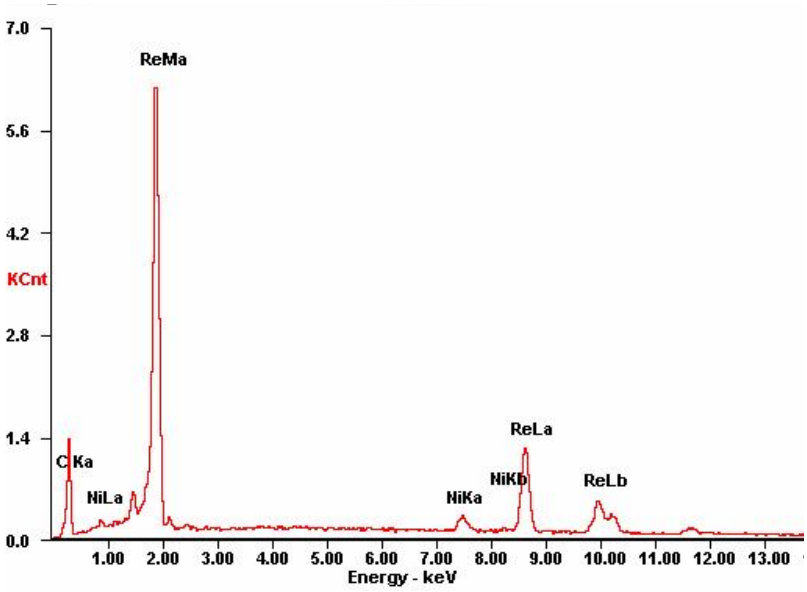

Figure 2.20 EDXS measurement from rhenium rich phase (shiny), also showing the nickel contribution

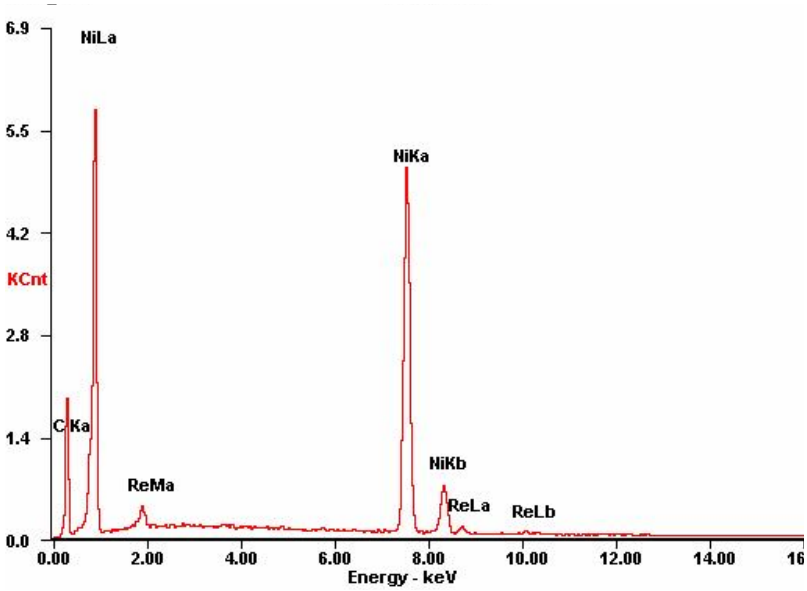

Figure 2.21 EDXS measurement from nickel rich phase (dark) indicating Ni as the majority component

Rhenium rich phase was further explored with WDXS measurements. Boron is a light weight element; therefore it is hard to detect with EDXS measurements. However, WDXS is a good method for detecting light weight elements. Boron contribution was confirmed with WDXS analysis from the rhenium rich phase. Figure 2.22 displays the WDXS result for boron.

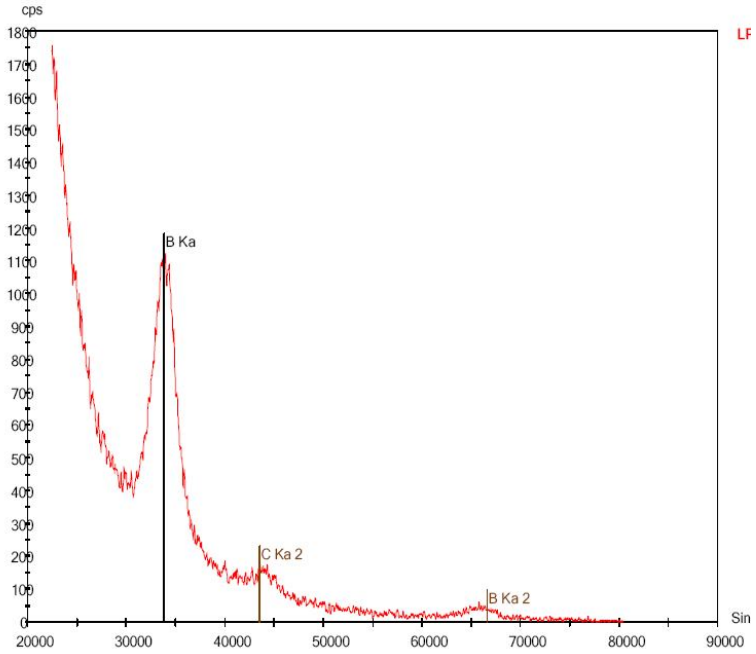

Figure 2.22 WDXS measurement confirms the contribution of boron to the rhenium rich phase

The composition of the compound was calculated by WDXS measurements from ten different points and figure 2.23 shows the points where measurements have been performed. The averaged values of the WDXS measurements were tabulated. It should be underlined that the results give only a rough estimation and not the exact composition of the respective sample. Table 2.2 exhibits the WDXS results from ten different points.

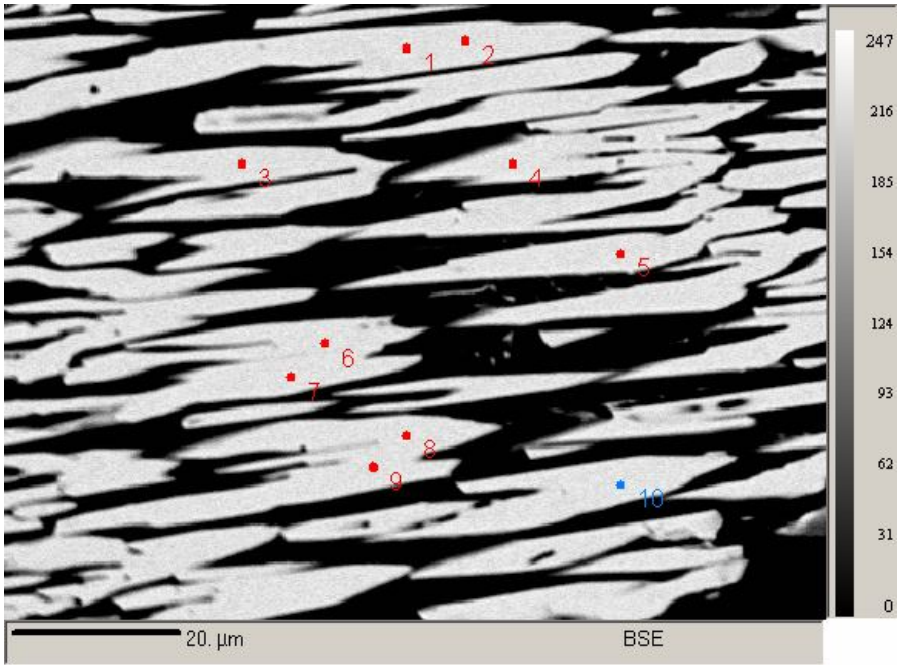

Figure 2.23 Back-scattered electron micrograph of Re-Ni-B with the points on which the measurements were performed

Table 2.2 WDXS quantification result for Re-Ni-B from ten different points

Average	Weight %	NormWeight%	Atomic %	Dev_Wt
B	3.04	2.99	32.51	0.28
Ni	4.48	4.40	8.83	0.61
Re	94.21	92.61	58.66	0.25

From the result of the WDXS analyses showed that the rhenium rich phase has the approximate composition of $Re_{20}Ni_3B_{11}$. Based on this, the empirical formula of the Ni-rich dark phase was calculated to $ReNi_{6.67}B_4$.

Figure 2.24 depicts the different ternary phases and their phase mixtures with binaries within the Re-Ni-B system.

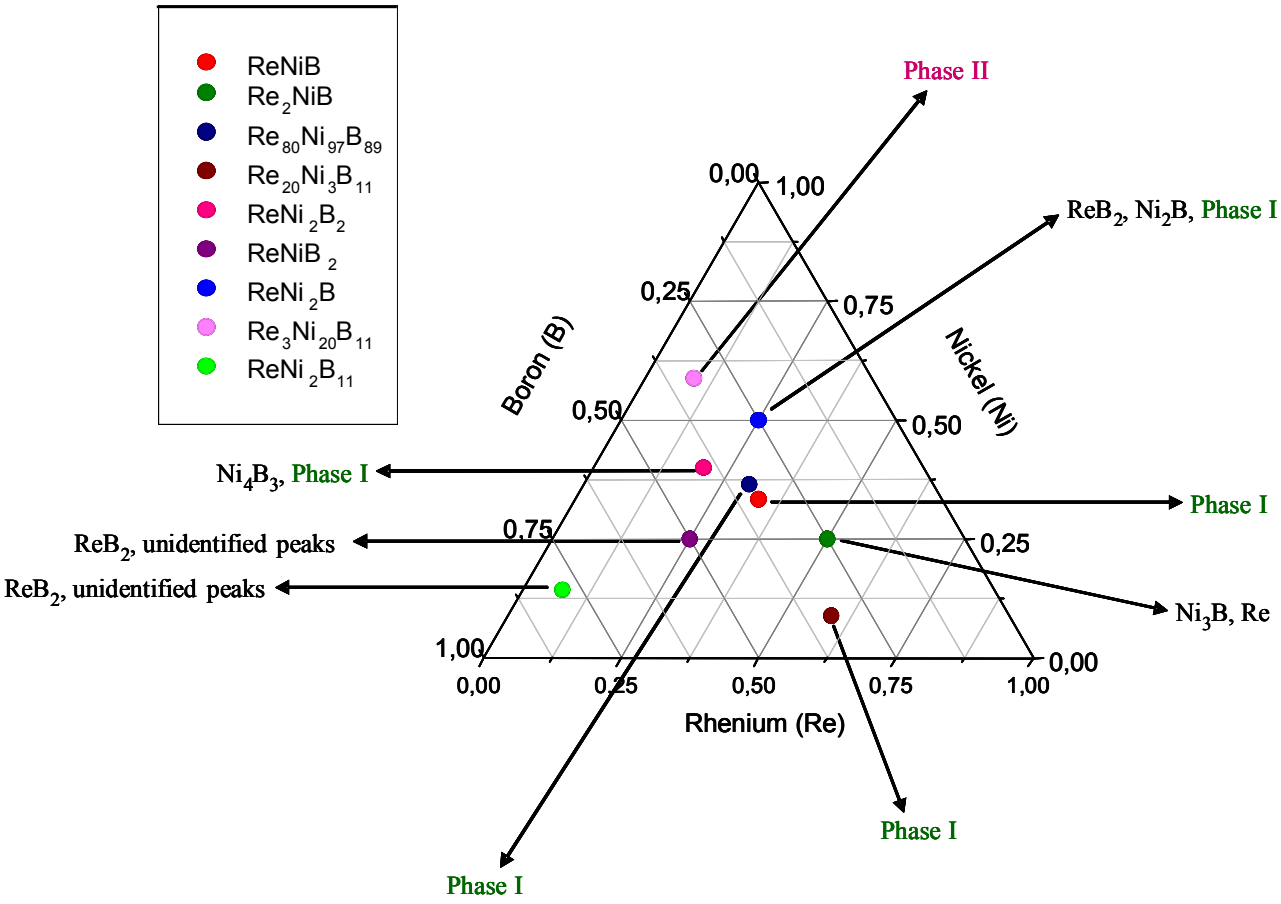

Figure 2.24 Different ternaries and binaries and their phase mixtures in the ternary phase diagram Re-Ni-B.

As future work, a systematic phase analytical study will be started aiming the isolation of the Re and Ni rich compounds as mono-phased products. The final goal is the determination of both the exact chemical compositions and the crystal structures of the two target phases either by application of the Rietveld Method to X-ray powder patterns or -when single crystals are available - by Single Crystal X-ray diffraction.

Chapter 3

3. Rhenium Diboride (ReB_2)

3.1 Introduction

The technology of today requires the usage of enduring materials, and carbides, borides or nitrides of transition metals are highly promising solids for these purposes. The conventional hard materials fulfill the expectations only up to a certain limit making the syntheses of superhard and ultra-incompressible materials to an interesting challenge for all preparative working material scientists. The mentioned properties were first observed for the cubic diamond (70-100 GPa) which is the hardest and most incompressible single-phase material known up to now. Conventoinally, any material with Vickers hardness higher than 40 GPa is defined as superhard material. After the discovery of synthetic diamond, cubic boron nitride (c-BN) yielded 45-50 GPa and took its place as second hardest material. However, both of those materials have some complications in industrial application. First of all, diamond is not appropriate for high temperature (>800 ^oC) utilizations, turning into graphite [21,22]. Also, boron nitride is not a good choice for iron containing materials due to the chemical dissolution of boron in iron. Furthermore, machines which operate at high speed may even exceed 1000 ^oC and this requires an oxidation resistance over that value. Recently published [Ref] refractory compound, rhenium diboride (ReB_2), is a "new" promising material which may help to overcome those problems. It has a melting temperature of 2400 ^oC and is ultra-incompressible, superhard material with Vickers hardness of 55.5 GPa [23].

Ultra incompressibility of ReB_2 is explained by two parameters which are high valence electron density and bond covalency. Among the transition metals, osmium has the highest valence electron density (0.572 electrons/$Å^3$) and rhenium is the second with a slightly lower value of 0.476 electrons/$Å^3$. When a boron atom migrates into the interstitial positions, it results in shortest metal-metal bond among the known transition

metal diborides and also the boron atoms form powerful covalent bonds. Bonding between rhenium and boron atoms is highly directional. It is known that highly directional covalent bonds resist elastic and plastic deformations; they suppress the formation and movement of dislocations and makes ReB_2 both incompressible and superhard. Figure 3.1 illustrates the charge density for ReB_2 where (Re–B) and (B–B) bonds exhibit high directionality [24,25].

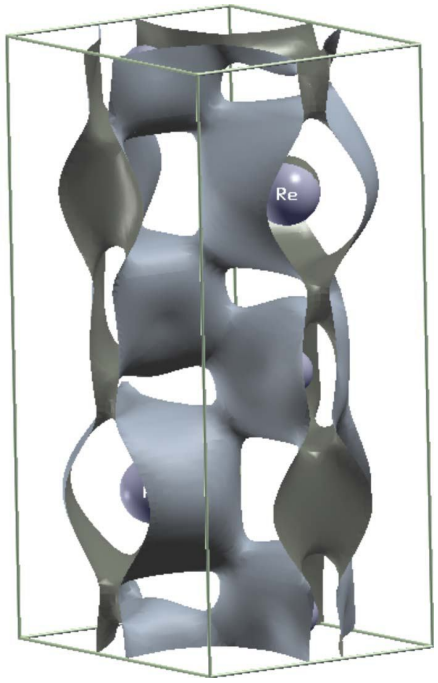

Figure 3.1 Charge density of ReB_2 where Re-B and B-B exhibit high directionality.

The synthesis of ReB_2 was inspired by the discovery of Re_2B upon which the Re–B system was reinvestigated by *Placa et al.* and a new tetragonal ReB_2 phase was isolated. The compound was prepared by induction heating (~ 1500 ^{o} C) of rhenium powder with amorphous boron in helium vitrified alumina crucible whose powder diffraction data is presented in table 3.1 [26].

Table 3.1 Powder diffraction data: ReB_2, Cu Kα, Ni filter

I/I_o^*	*d* (Å)	*Hkl*
65	2.74	002
30	2.51	100
100	2.38	101
20	2.08	102
11	1.868	004
40	1.768	103
7	1.499	104
14	1.449	110
15	1.351	112
9	1.284	105
3	1.255	200
2	1.246	006
9	1.238	201
3	1.190	202
9	1.145	114
7	1.121	203
2	1.116	106

ReB_2 is also accessible via arc melting (>3000 ^oC) [27] and zone floating (≈ 1800 ^oC) [28]. After the discovery of the potential usage of rhenium diboride in industry, different synthesis methods were applied to reduce the reaction temperature and the annealing time. Recently, *Levine* [29] introduced the aluminum flux method in which aluminum was employed as a solvent. For this synthesis, the reaction temperature and the molar ratio of the reactants Re/B/Al were set as 1400 °C and 1:2:50. Compared to the two conventional methods, the reaction temperature could significantly be reduced while the annealing time was reported to be approximately 10 hours. The main disadvantage of the flux technique in this case was the incorporation of some the molten aluminum metal into the final product resulting in a change of its chemical composition: $ReAl_{0.011}B_{1.85}$ [29].

In this thesis, ReB_2 was investigated with three different methods that make the synthesis more feasible for industrial production. Experimental methods and reaction optimizations were presented in ‘experimental procedures’.

3.2 Experimental Procedure

The synthesis conditions for ReB_2 have been investigated using the flux method, arc melting and microwave induced plasma. Although rhenium diboride is a well characterized material there are still preparative problems regarding the phase purity of the final product. The conventional preparation technique prefers the reaction at high temperatures followed by annealing for long hours, which is energy and time consuming.

In the presents study, two alternative synthesis methods - lead flux and microwave induced plasma - were successfully applied both yielding phase pure ReB_2. In addition, the conditions for conventional arc melting synthesis for ReB2 were optimized with respect to the molar ratio of the starting elements. All three preparation methods are summarized in Figure 3.2.

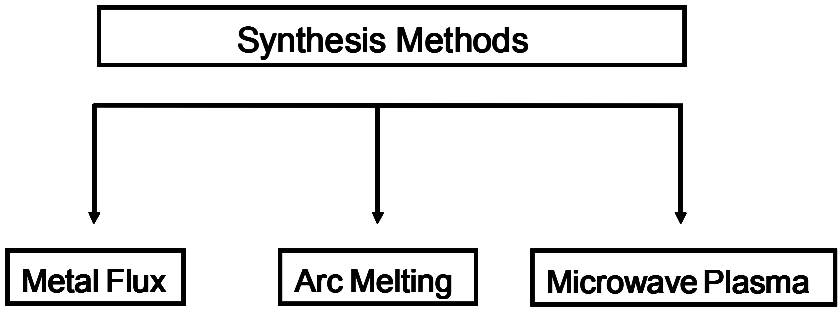

Figure 3.2 Flow diagram of the preparation methods employed for the synthesis of rhenium diboride, ReB_2.

i) Metal Flux

The synthesis studies on superhard ReB_2 were motivated by the recently published work entitled *'Preparation and Properties of Metallic, Superhard Rhenium Diboride Crystals'* [29] describing the isolation of single crystals from an aluminum flux after annealing of the starting elements Re/B/Al (molar ratio = 1/2/50) for 10 hours

at 1673 K. In the present study, ReB_2 was synthesized by using lead (Pb) flux at 1073 K and a molar ratio Re/B/Pb: 1/2/10. The annealing time was 5 hours.

Reaction Temperature Determination

First attempt for the determination of the reaction temperature of Re and B was a zone melting experiment in B_2O_3 (flux) in which the mixture was sintered at 2073 K [28]. In 2009, a sample shrinkage (δ) experiment was performed under applied 20MPa mechanical pressure. At 963 K, sample shrinkage reveals a steep increase within a short time (Figure 3.3) which was interpreted as the temperature of reaction.

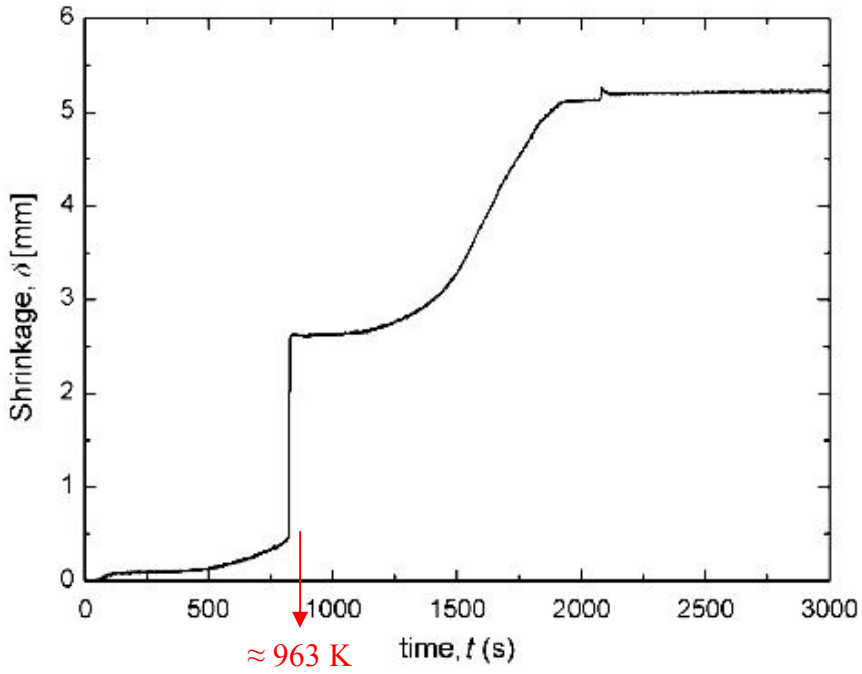

Figure 3.3 Temporal profile of sample shrinkage

Based on these results, the phase transformation from Re_7B_3 to ReB_2 occurred at 973 K which corresponds to sudden increase in shrinkage values. Powders of starting mixtures and sample from the beginning and after the completion of shrinkage are compared in Figure 3.4 [30].

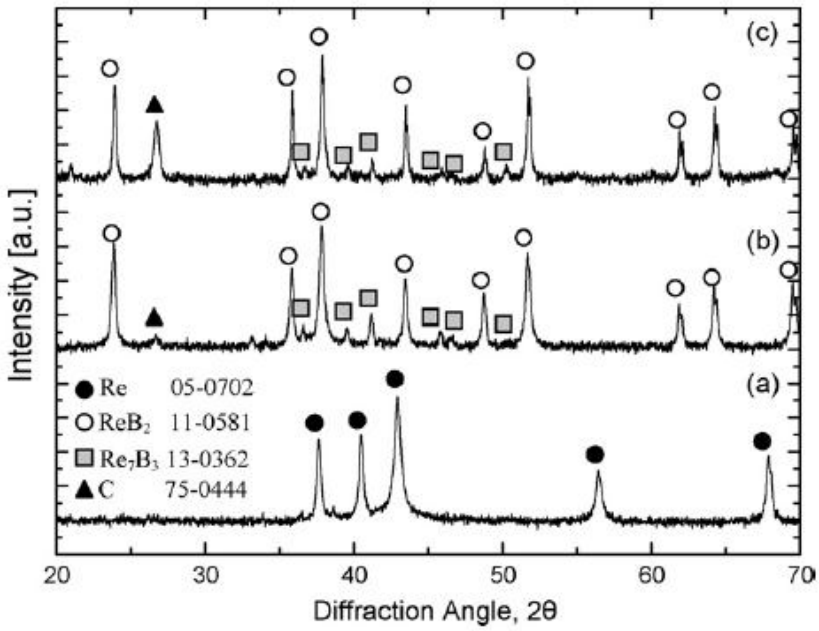

Figure 3.4 X-ray patterns of a) Starting powders, b) Sample at the beginning of shrinkage, c) after the completion of shrinkage

At the proposed temperature the conversion of the starting elements to ReB_2 and Re_7B_3 was registered. Comparison of figure b and c indicates that at the end of the shrinkage, Re_7B_3 transforms to ReB_2; but not completely. The final product contains always traces of Re_7B_3.

These two experiments were performed under applied pressure but ended with an incomplete conversion; i.e. with contaminated ReB_2. Based on these findings, an educated guess was made for the detection of reaction temperature in this thesis. Lowest reaction temperature that can be tried was the melting point of lead which is 596 K. After that temperature, flux starts to form. Two different temperatures were chosen: 873

and 1073 K. Since one of the aims of the present study is the reduction of the reaction temperature to modest values, 873 K was tried first, with the result that the powders did not react at all. Therefore, the sample mixture was heated to 1073 K which surprisingly ended in formation of single phase ReB_2. X-ray diagrams of two different reaction temperatures were presented and discussed in 'results and discussion part'. The temperature for the neat crystallization of ReB_2 obtained at 1073 K was used as reference for further experiments. Prior to employment of Pb flux, Sn and NaCl fluxes were also used, but the experiments ended without mentionable success.

Flux synthesis is a very useful method for performing high temperature syntheses at low temperatures. However, there may be contaminations of flux metal in the final compound which may alter its chemical and physical properties such as hardness, resistance to corrosion etc. Therefore, ICP-AES and EDX measurements were performed to prove that the final product is lead-free.

Experimental setup in figure 2.5 was used. A stoichiometric amount of rhenium was mixed with amorphous boron in an agate mortar. Lead pieces were added onto the mixture so that the final molar ratio of the components was Re:B:Pb = 1:2:10. Synthesis was performed in an alumina crucible under argon gas. The sample was heated up to 1073 K and dwelled at this temperature for 5 h. Pb was removed by boiling with 70% hydrochloric acid. Final product was a black colored powder, stable to air and moisture.

ii) Arc Melting

According to *'Synthesis of Ultra-Incompressible Superhard Rhenium Diboride at Ambient Pressure'*, phase-pure ReB_2 synthesis is also possible with arc melting. However, boron excess values were not given. In this study, we try to synthesize the phase pure ReB_2 by optimizing the boron excess.

Different atomic ratios of 0.5000 g of samples were prepared and mixed thoroughly. 0.13 mm diameter pellets prepared with 10 kN force and arc melted for minimum of 5 times for homogeneity. . In order to avoid any oxidation, the system was evacuated until the sample was cooled down. Final product was shiny and air/moisture stable. Characterizations of the compounds were performed with X-ray powder diagram.

iii) Microwave Induced Plasma

Plasma refers to the fourth state of matter in which - similar to gas - a certain portion of the particles are ionized [31]. Arc is also a type of plasma which can be considered as thermal plasma. It operates over a wide range of pressures (0.1-100 atm) and currents (5-2000 A) with an electron density of approximately 10^{15}-10^{18} cm^{-3} [32]. In case of microwave induced plasmas, microwave power, electromagnetic radiation in the frequency range of 300 MHz to 10 GHz was used. Pressure values were less than 0.1Pa to a few atmospheres and power values vary between a few W to several hundreds of kW. Ionization degree was less than arcs which represents the non-equilibrium plasma with high electron temperature and low gas temperature. Thus, microwave induced plasma systems create high concentrations of chemically active species keeping the bulk temperature as low as possible. Therefore, they allow stimulation of chemical reactions which are not possible by conventional methods [31].

In this study and for the first time ever, the synthesis of ReB_2 was accomplished by the microwave induced plasma technique. Varying molar ratios of the starting elements were employed and hereby an unexpected phase was discovered. Two different plasma gases were used: argon and hydrogen, but only hydrogen plasma resulted in the successful formation of ReB_2. The efficiency of these two plasma gases in the respective reactions is discussed in ‘results and discussion part’.

In a typical reaction batch, a total of 0.25g of the powdered mixtures of Re and amorphous boron B (molar ratios: 1:1, 1:2, 1:4, 1:7 and 1:10) were homogenized and pressed to pellets (p = 10 kN) and transferred into an alumina crucible. The crucible was then placed into a silica reaction tube equipped with a gas inlet and outlet. After evacuation to $p \approx 10^{-3}$ mbar, the system was purged with hydrogen gas and the plasma ignited. When the reaction was done, the silica reaction vessel was disconnected from the vacuum pump and filled with hydrogen gas. The sample chamber was not opened before the system was cooled down to room temperature.

The experiments were performed employing a gas flow rate of 100 sccm and power of 1200 W for 30 min. Different power values (800 W, 900 W and 1000 W) and reaction times (1.30 h and 1 h) were also tried, but the experiments performed at 1200 W (30 min) gave the highest yield.

iv) Ball Milling Study with ReB_2

The synthesis of ReB_2 by ball milling has already been reported, in which the strong exothermic reaction enthalpy of the metallothermic mixture of ReO_2, B_2O_3 and Mg was used as the driving force [33]. Our attempts to reproduce the results failed, however, yielding only contaminated ReB_2 as final product. In the present study, ball-milling experiments were performed exclusively for the particle size reduction of the ReB_2 crystallites. At the end of the ball-milling experiments, the particle size of superhard ReB_2 could successfully be reduced from 1μm to 300 nm. As expected, none of the milled samples showed any indication of thermal decomposition. The investigations were performed with ReB_2 obtained from lead flux. Unmilled sample's particle size distribution was detected with dynamic light scattering and using Hall-Williamson plot as well. DLS measurements and Hall-Williamson plot calculation

resulted in similar values of 1μm and 933 nm, respectively, indicating that particle and grain sizes are compatible.

3.3 Results and Discussion on Rhenium Diboride (ReB_2)

3.3.1. ReB_2 with Flux Synthesis

ReB_2 was successfully synthesized in lead flux at 1073 K (dwell time 5 h). Attempts at 873 K failed, very likely due to the lower solubility of elements in molten lead with respect to liquid metal fluxes such as tin and aluminum. Figure 3.5 shows the powder diagrams of the reactions products obtained from lead flux at 873 K and 1073 K.

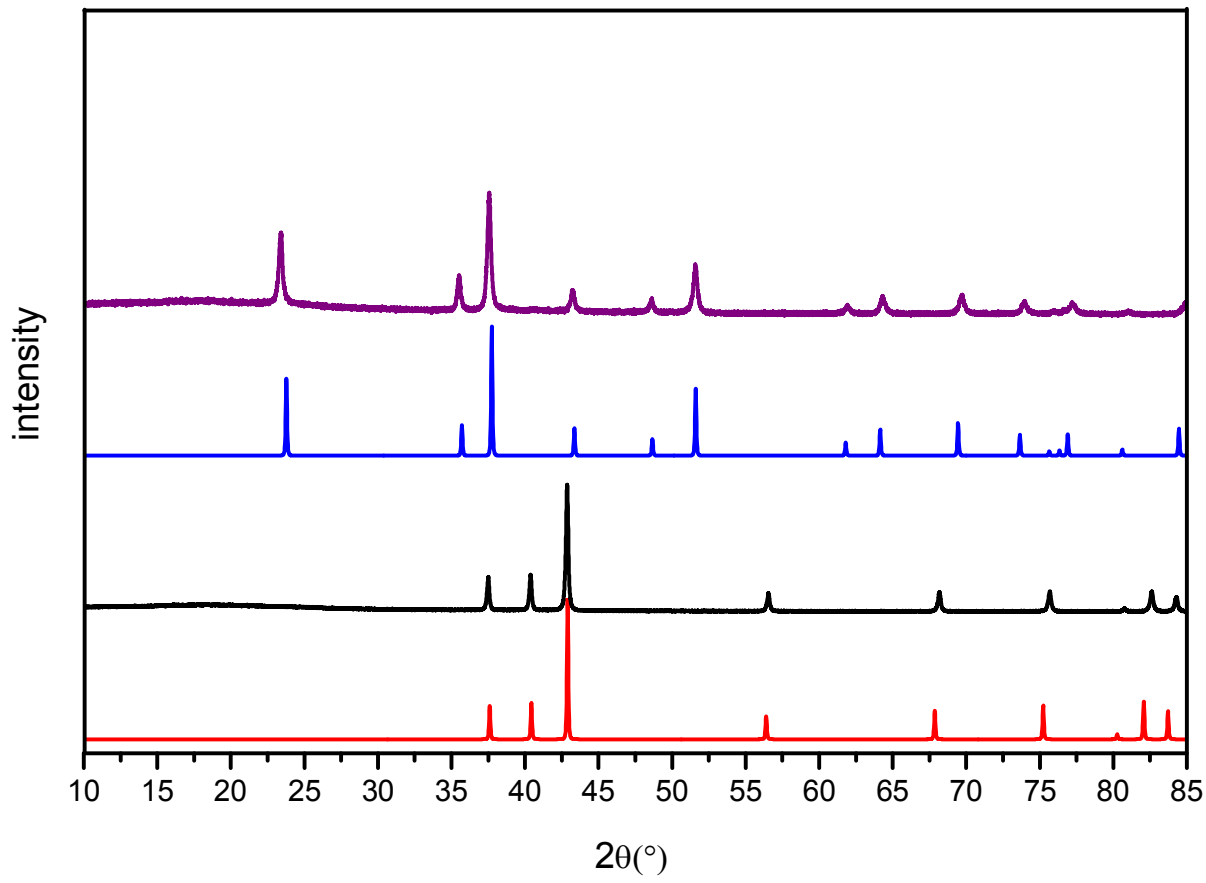

Figure 3.5 Comparison of two fluxes at different temperatures, 873 K and 1073 K

As a future work, reaction temperatures between 873 K and 1073 K should be performed. Lower reaction temperatures are probable for ReB_2 synthesis.

Flux method is really good in terms of performing high temperature synthesis at low temperatures; however, there may be contaminations of flux metal in the final compound which may alter its chemical and physical properties such as hardness, resistance to corrosion etc. Therefore, ICP-OES and EDXS measurements were performed to prove that the final product is lead-free. Based on the results of ICP-OES measurements, the sample composition corresponds to $ReB_{1.98}$. The difference of 0.02 percent is within the standard limits. Furthermore, no lead could be detected in any of the specimens. A further confirmation came from EDXS measurements performed for lead whose results are displayed in Figure 3.6.

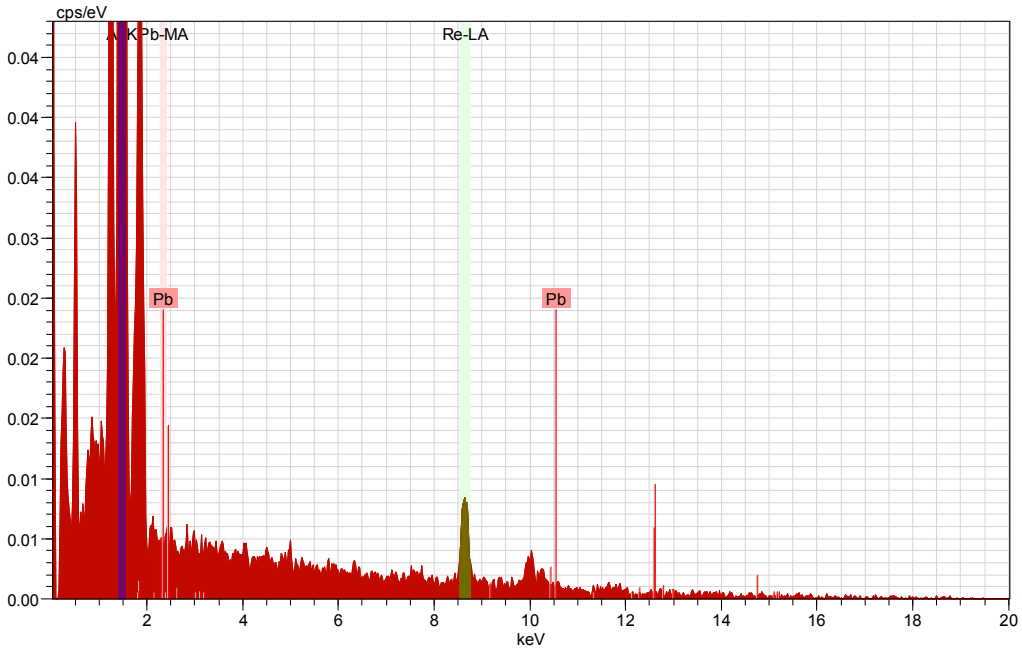

Figure 3.6 EDXS measurement of ReB_2

Both ICP-OES and EDXS are very sensitive analytical methods, particularly for lead and Re. The results allow to conclude that phase-pure ReB_2 could be synthesized using a lead flux for the first time and the without any contribution from lead.

3.3.2. Differential Thermal Analysis

ReB_2 is also an important refractory material whose thermal properties are of general interest. Therefore, differential thermal analyses were performed to investigate its resistance to thermal degradation. DTA measurements (Fig. 3.7) showed that aluminum flux-grown ReB_2 was more resistant to thermal degradation than the one synthesized via solid state reaction from the neat elements [29].

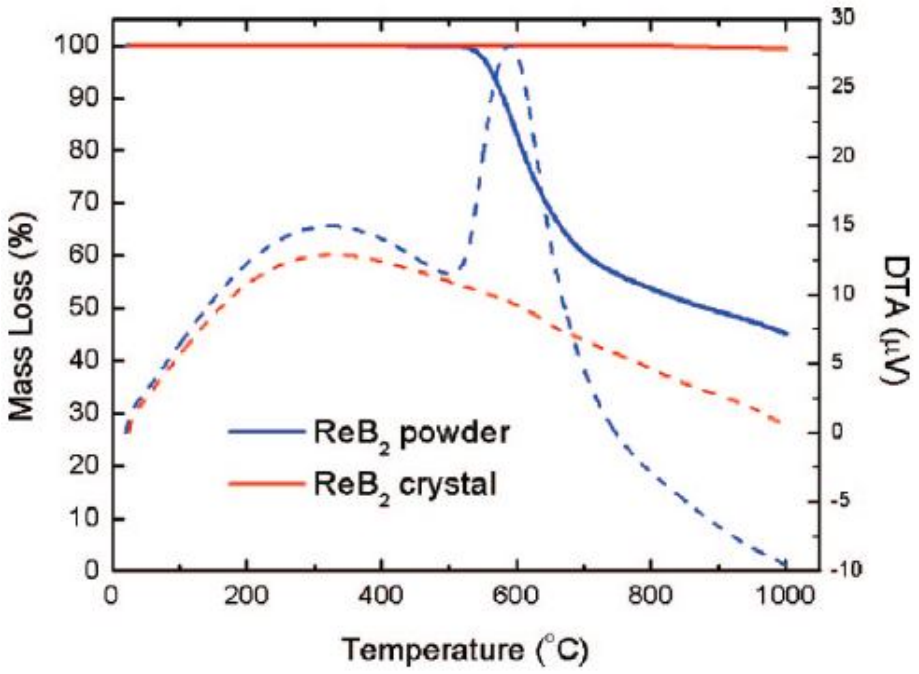

Figure 3.7 Comparison of the DTA results of aluminum flux-grown ReB_2 (red dashed line) and ReB_2 obtained from the solid state reaction (blue dashed line)

ReB_2 synthesized from the straight forward reaction of the elements reveals an exothermic peak at 873 K, while the flux-grown samples do not form any thermal effect. In order to compare these data with our samples, differential thermal analysis of ReB_2 synthesized in lead flux was performed in the temperature range of 298K to 1373 K under synthetic air. The applied heating and cooling rates were 278 K/min and figure 3.8 illustrates the result of the DTA measurement.

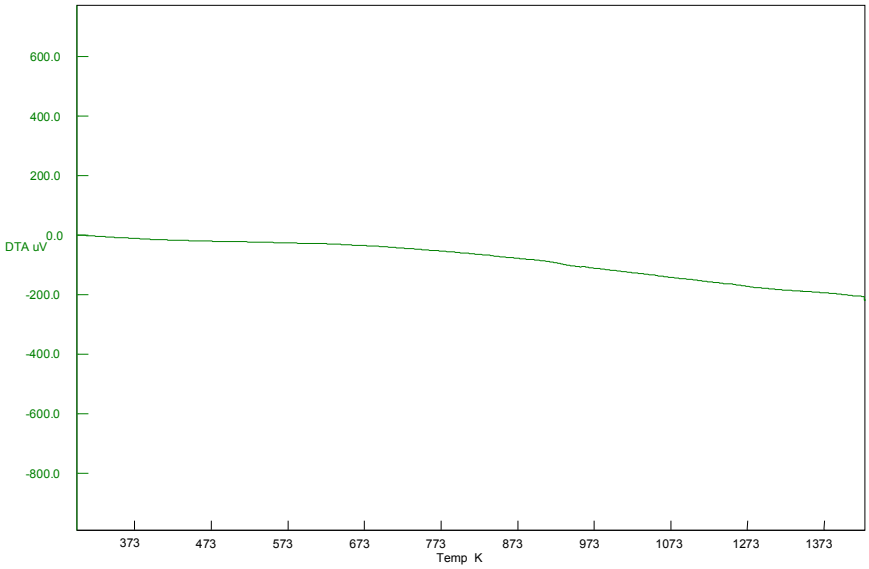

Figure 3.8 DTA curve of lead flux-grown ReB_2 within the temperature range of to 278 to 1373 K.

DTA measurement verifies that the synthesized ReB_2 is stable until 1373 K. According to *Levine* et al., exothermic effect in the sample from direct synthesis results from formation of metal oxides. However, in case of flux-grown ReB_2, a part of boron atoms are replaced by those of the flux metal. The free boron migrates to the surface of the crystallites and form a preventive layer of B_2O_3 protecting the compound from thermal degradation [29]. But this explanation is not plausible, since the direct synthesis of ReB_2 by arc melting requires always certain excess of boron for balancing the losses due to evaporation. Phase diagram confirms also that surplus of boron favors the formation ReB_2 (figure 3.9).

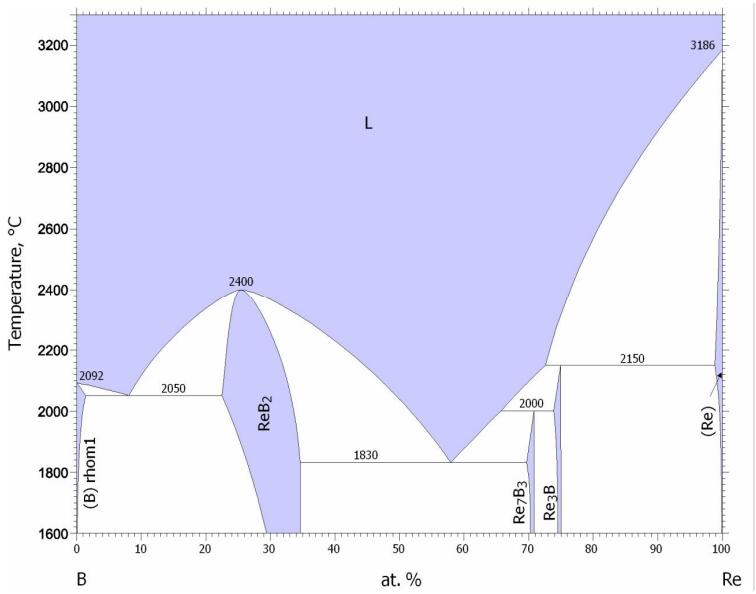

Figure 3.9 Phase diagram of rhenium and boron

More probable origin of the exothermic effect might be the combustion of the excess boron in the solid-state synthesized ReB_2. For clarification, DTA measurements were performed, to investigate the combustion behavior of Grade I boron (≥ 95%, H.C. Starck) under atmospheric conditions (Fig. 3.10).

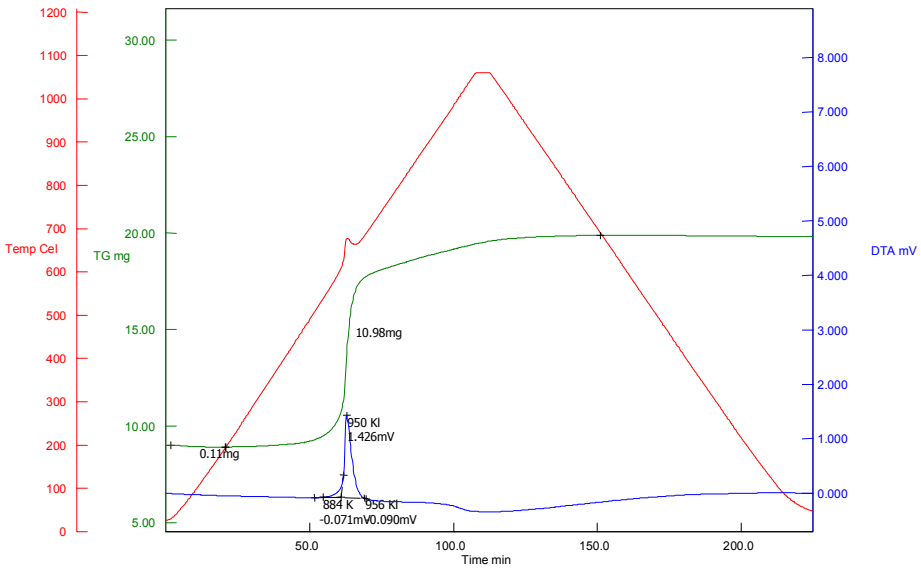

Figure 3.10 DTA measurement of Grade I boron from H.C. Starck company

As can be seen from the TG curve, there is an exothermic peak at 950 K coupled by a gain of mass. Regarding that the combustion of amorphous boron occurs approximately at 950 K, the observed peak and the reported effect in the solid-state synthesized ReB_2 are not compatible. Very likely, the thermal effect in the latter one is caused by the contaminations in the used amorphous boron. Since, the purity grade of the boron employed in [29] is not specified; further substantive comments are not possible.

The results allow the conclusion that for the element synthesis via solid-state reaction, the impurity level of boron will directly effect the final composition of the target compound. In addition, the high temperatures enhance loss of boron due to evaporation so that excess boron is needed for the completion of reaction. However, in the flux method, most of the impurities are leached out by the molten metal. Therefore, the flux method seems to be the most preferable route for preparation of pure binary and ternary transition metal borides.

3.3.3. Arc Melting Synthesis of ReB_2

As stated before, arc melting synthesis of phase pure ReB_2 is only possible when surplus of boron is employed. Until now no clear information was known about how much surplus should be applied. Several experiments were performed to optimize the boron excess. The results are illustrated in Fig. 3.11 and 3.12.

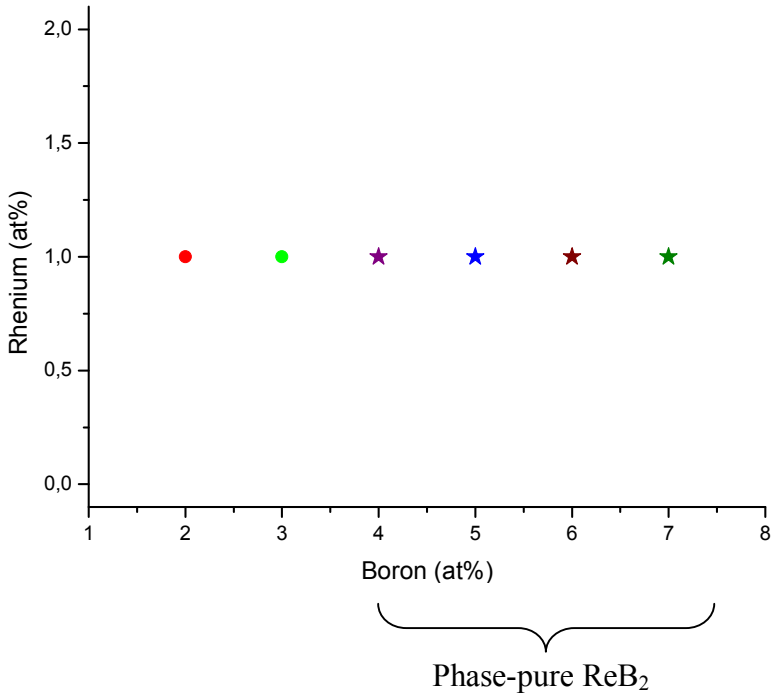

Figure 3.11 Phase-pure ReB_2 synthesized via arc melting using different rhenium/boron atomic ratios.

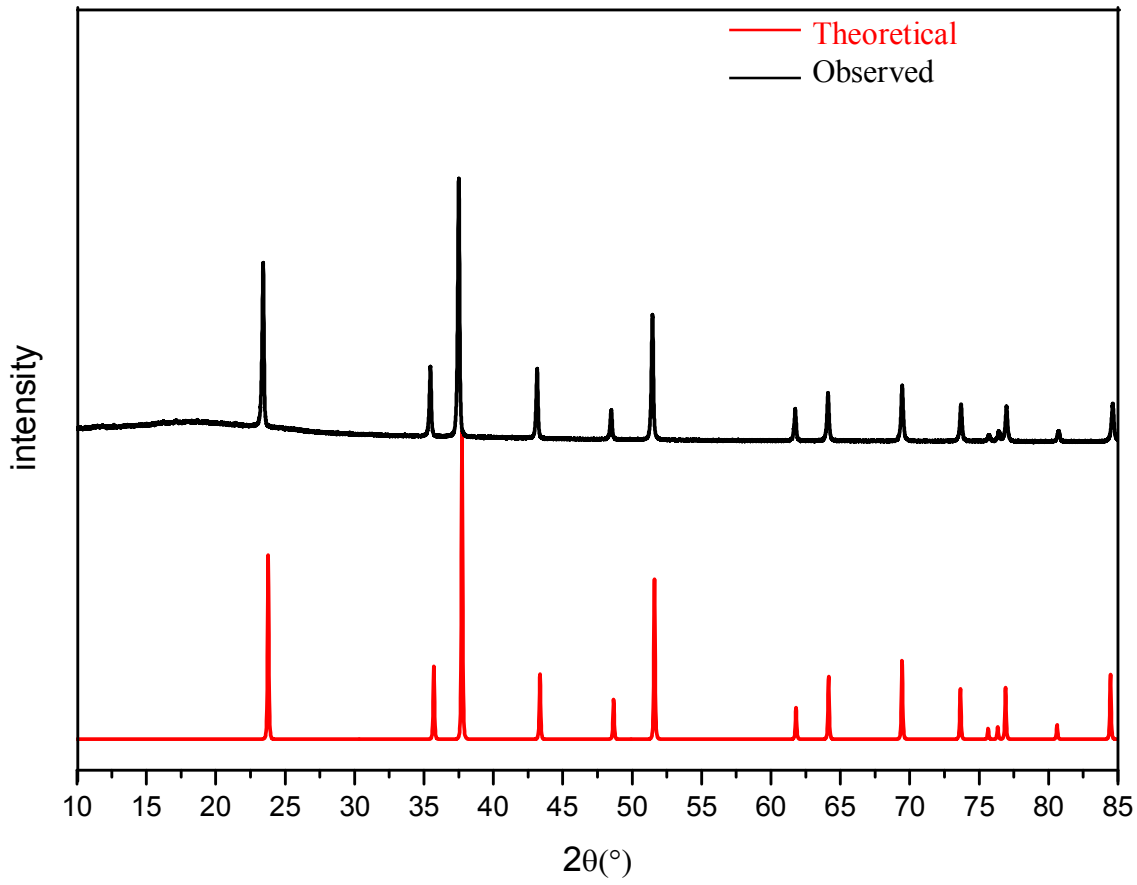

Figure 3.12 X-ray diagram of ReB_2 obtained from arc melting (black) in comparison with the theoretical one (red).

From Fig. 3.12, one can easily see that mixtures with molar ratios Re:B = 1:2 and 1:3 did not yield ReB_2. In contrast, the samples with molar ratios of Re/B = 1:4 to 1:7 clearly indicate the formation of ReB_2, probably in coexistence with excess amorphous boron. Unfortunately, the latter, is not detectable by X-ray diffraction, so that the exact amount of unreacted boron could not be determined. Regarding that temperatures during arc melting process may exceed 3723 K, it is very likely that most of the excess boron was evaporated.

3.3.4. Microwave Induced Plasma Synthesis of ReB_2

Argon and hydrogen gas plasma experiments were performed with a flow rate of 100 sccm and power of 1200 W for 30 minutes. Unfortunately, all synthesis attempts in which argon gas plasma was used failed while experiments with hydrogen plasma yielded ReB_2 and a foreign phase (Fig. 3.13).

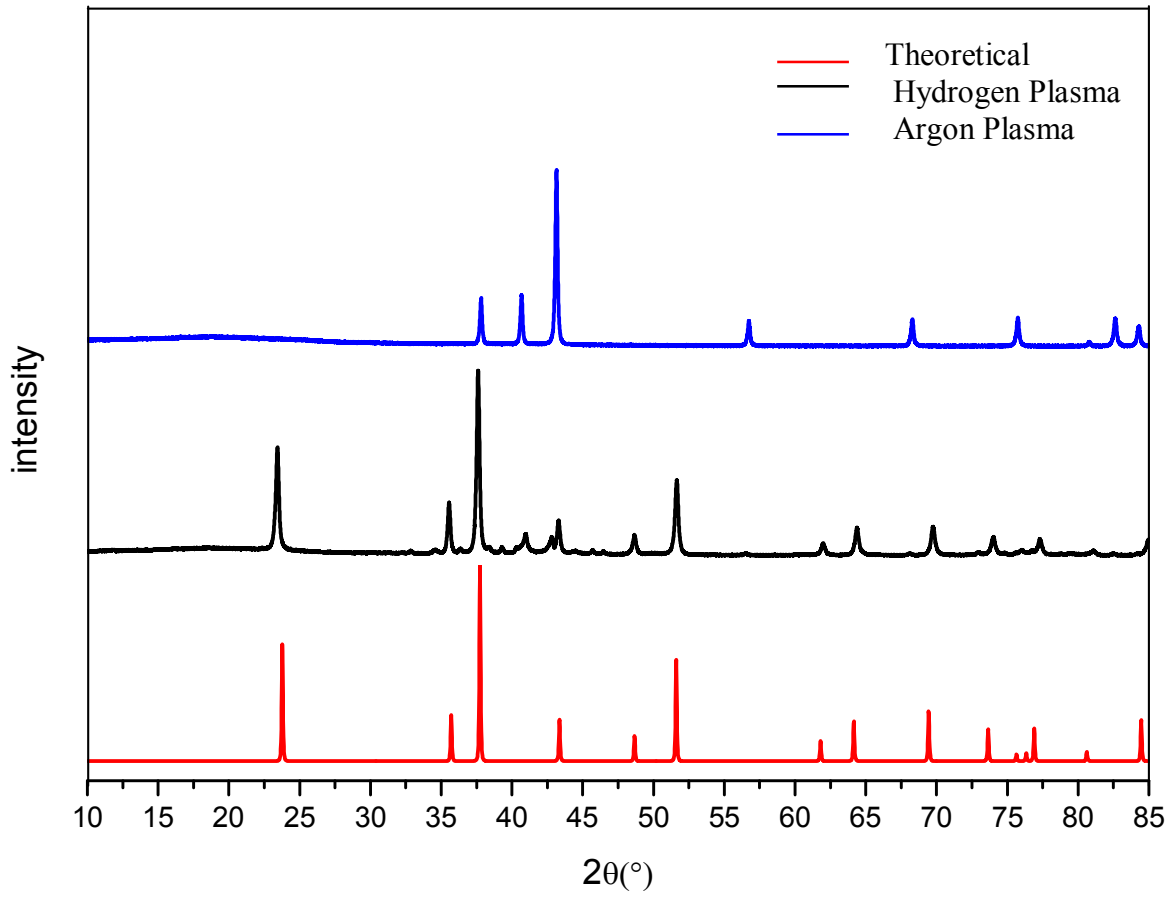

Figure 3.13 Comparison of the products obtained from ReB_2 preparation in argon and hydrogen gas plasma.

For a deeper understanding of the question why hydrogen gas plasma was more successful, reaction parameters were reinvestigated. The first observation was that

plasma temperatures for the two gases differed dramatically. The temperature values were measured in correlation with flow rate of the plasma gases using a thermocouple placed into the plasma setup (Fig. 3.14).

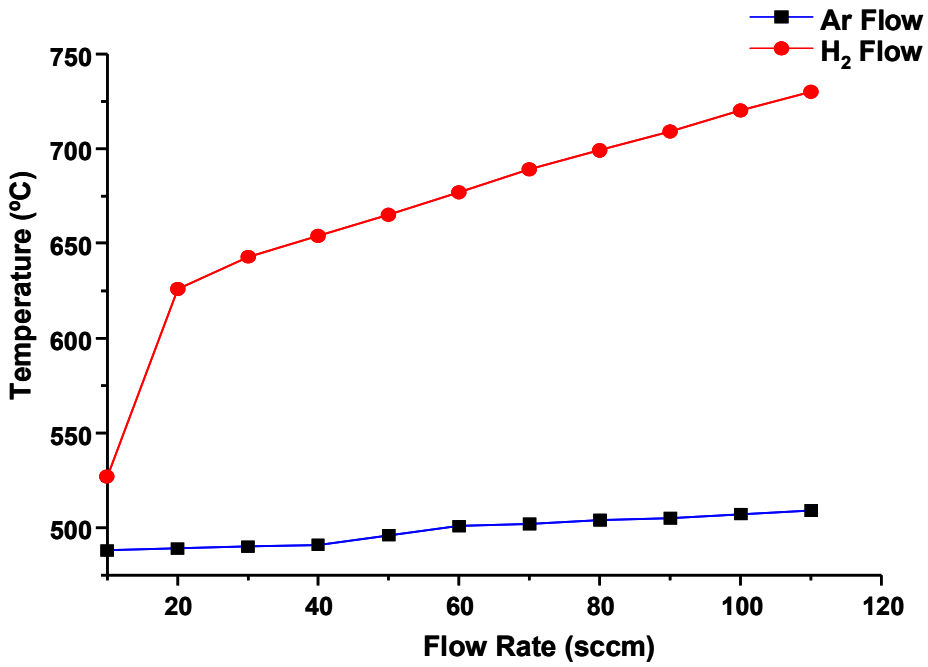

Figure 3.14 Temperature values of argon and hydrogen plasma with respect to flow rate

The maximum temperatures obtained with hydrogen and argon plasma were ~ 900 K and 700 K, respectively. It is important to note that these values are more or less rough estimations, but they are useful and meaningful when considered that the data represent two comparative experiments performed under equal conditions.

3.3.5. Characterization of new phase obtained from microwave induced plasma

According to the binary phase diagram of ReB_2, boron excess should favor the formation of rhenium diboride. However, during the microwave induced plasma synthesis, a new phase emerged, particularly when the samples were boron rich. For clarification, a series of specimens with excess boron were prepared and the results are analyzed in context with those of "rhenium rich" ones. Figure 3.15 and 3.16 display the phases investigated and the corresponding X-ray patterns, respectively.

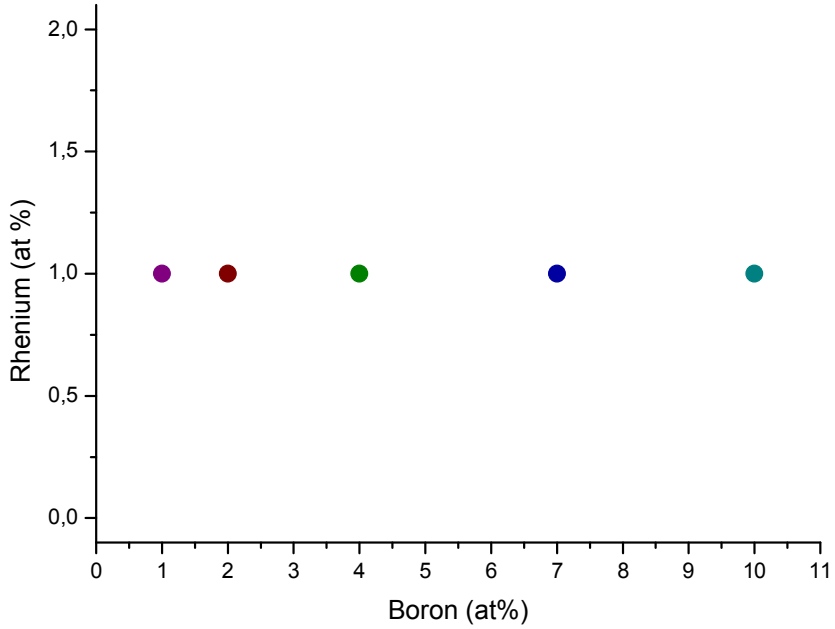

Figure 3.15 Results of the syntheses performed in microwave induced plasma for different Re/B ratios.

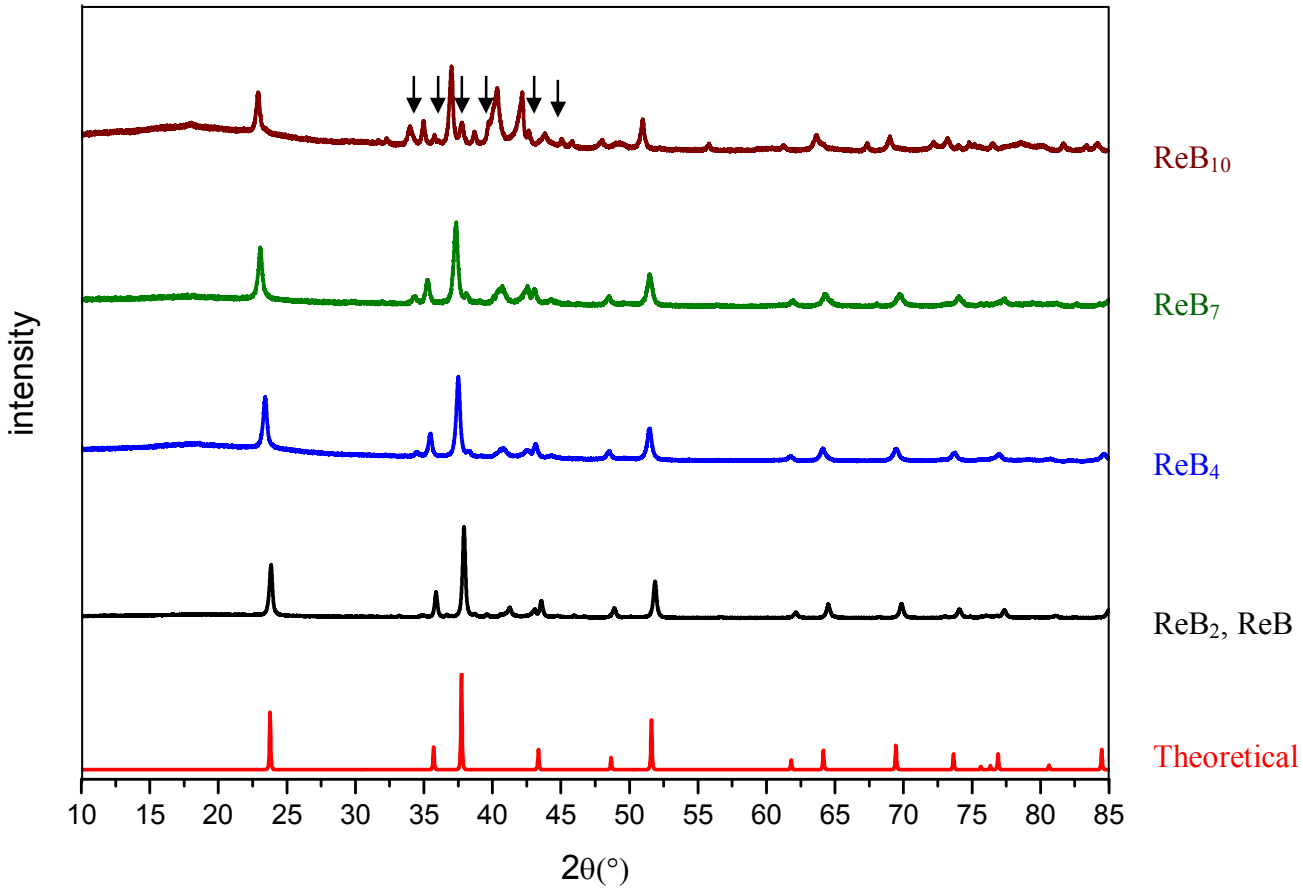

Figure 3.16 Formation of the new rhenium boride phase in correlation with increasing with increasing B/Re ratios. Significant peaks of the new phase are indicated.

There are two plausible explanations for the formation of the new phase. The first one could be the magnesium impurity present in the conventional amorphous boron. The other reason might be due to the high reaction rates generated in the microwave induced plasma. In the arc melting synthesis, magnesium impurities were not a serious problem because of the extreme high operation temperatures. Magnesium is a very volatile metal and one can assume that at 2500 K and more, no trace of magnesium would be left in the sample. In order to verify that new phase was a binary comprising only rhenium and boron and to exclude any Mg incorporation, the previous

syntheses were repeated, but using amorphous boron free of magnesium instead. The latter was prepared in our laboratories via thermal decomposition of diborane, B_2H_6.

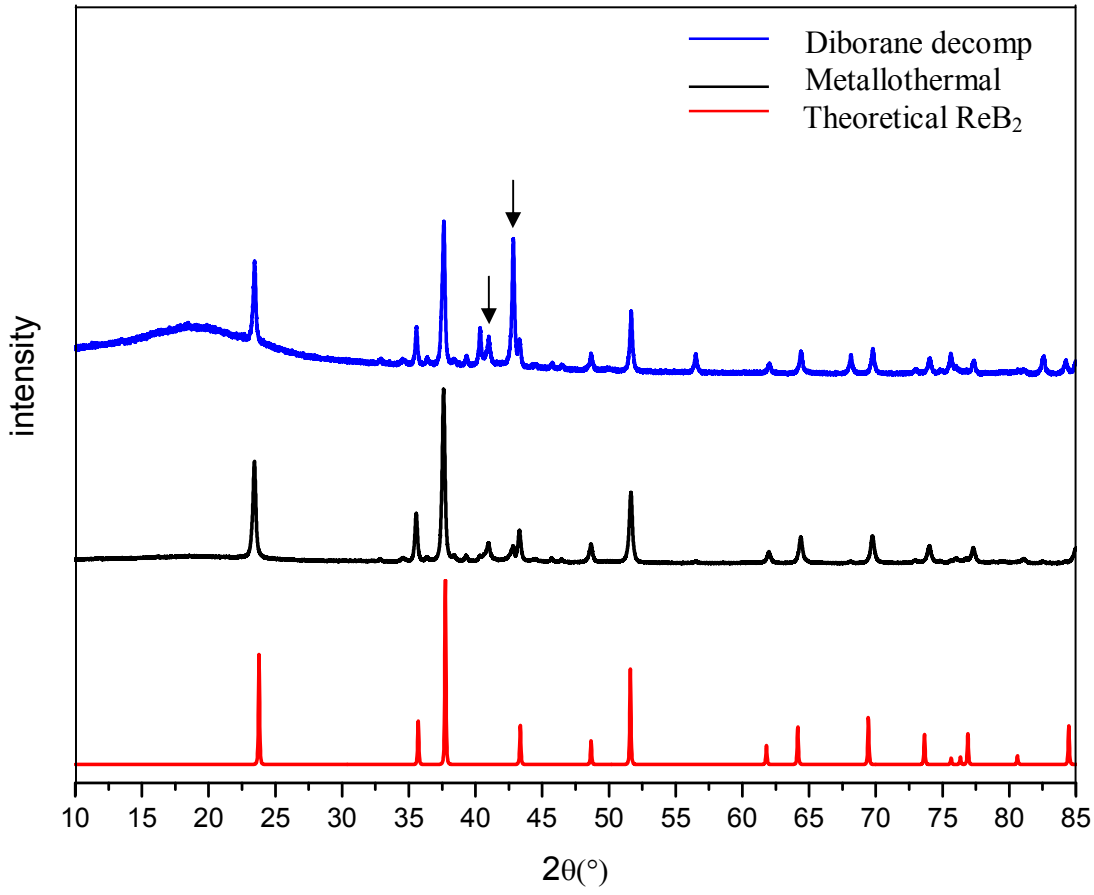

Figure 3.17 Powder patterns of the new phase synthesized using Mg-free and conventional (Mg: 0.8-1%) amorphous boron.

The results in Fig. 3.17 clearly reveal that the new phase forms with the magnesium free amorphous boron, as well. The only difference is that specimens prepared with Mg-free boron crystallize better. This findings are compatible with the higher reactivity of the magnesium free boron powder, connected with comparatively small particle size (ca. 200 nm) and the spherical morphology. The results confirm that the new phase is a boron rich pure binary consisting of Re and B only and the formation is not affected by the impurities contributed by the starting elements.

Still, there is one concern left related with hydrogen plasma source as a possible candidate enhancing the formation of the foreign phase in the microwave. To exclude this hypothesis further investigation were necessary, for which mass spectroscopy and DTA were used. Fig. 3.18 depicts the theoretical mass spectrum of diborane, B_2H_6, while that of ReB_{10} is shown in Fig. 3.18.

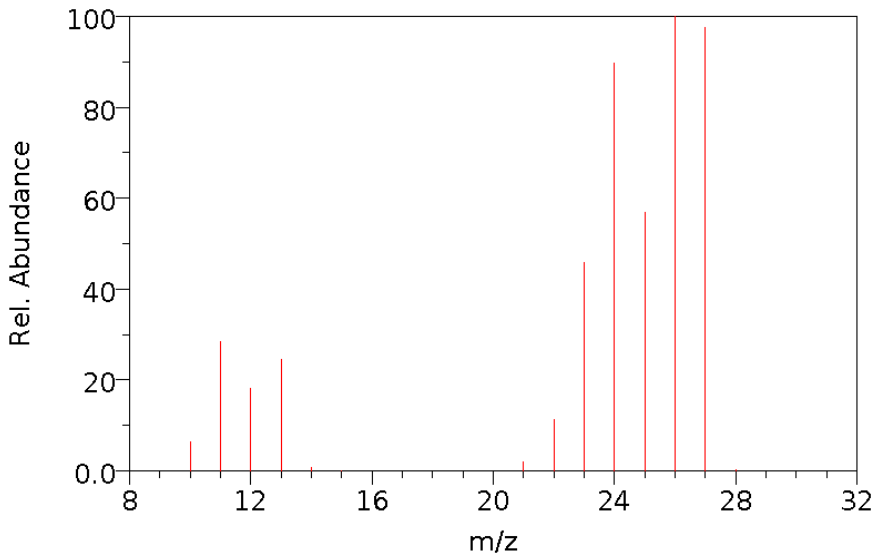

Figure 3.18 Theoretical mass spectrum of diboranes

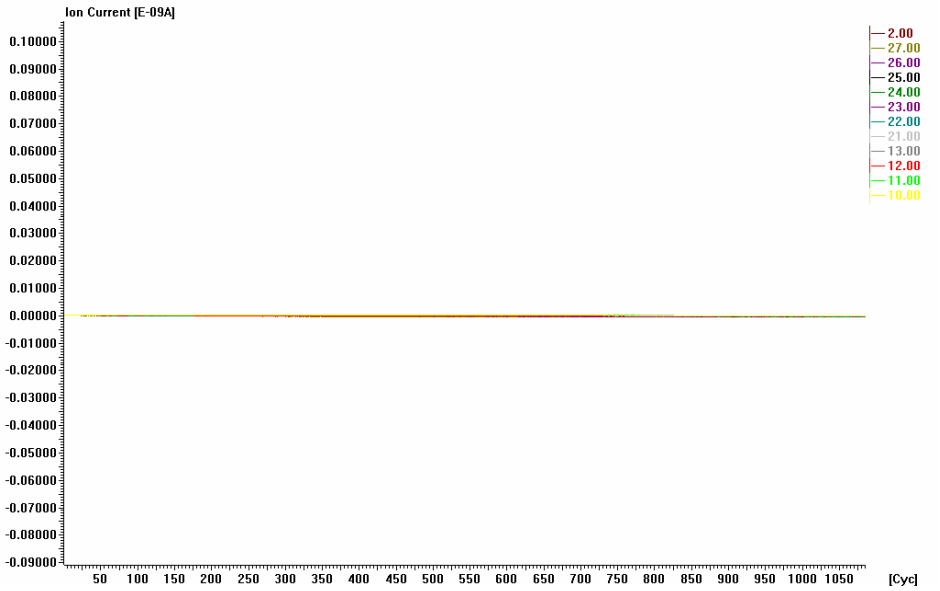

Figure 3.19 Mass Spectrum of ReB_{10}.

In case of any hydrogen incorporation, the sample should decompose before 1373 K yielding hydrogen and/or diborane or higher boranes. No single effect was detected in the mass spectrum. DTA measurement performed up to 1373 K with a heating rate of 278 K/min, revealed an interesting and unexpected property of the new phase. The compound is thermal stable only up to 948 K, above which a decomposition reaction takes place yielding rhenium diboride and boron (Fig. 3.20).

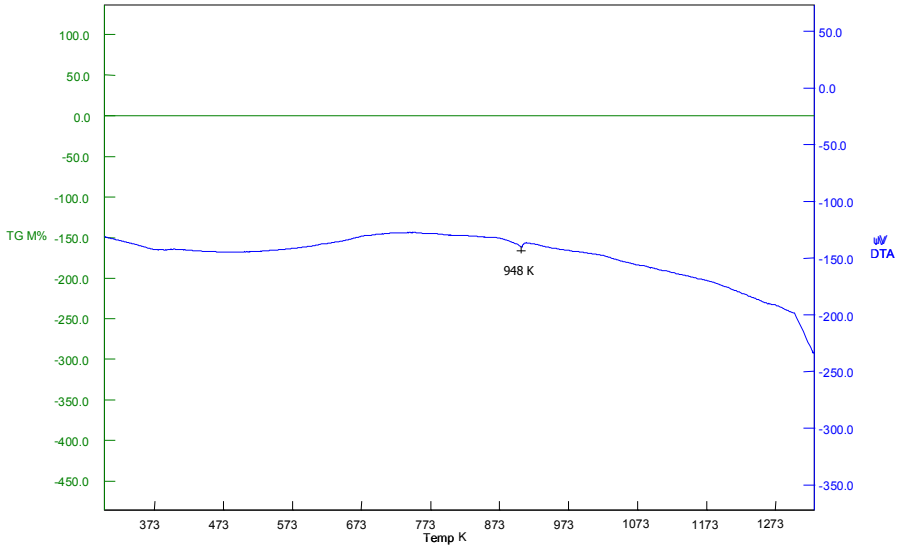

Figure 3.20 DTA measurement of new phase of Re and B.

The results explain, why the new phase has never been observed in conventional solid state reactions. Because at low temperatures, rhenium and boron do not react at all while at elevated temperatures the decomposition to ReB_2 and boron is favored. The microwave induced plasma technique allows syntheses by maintaining the bulk temperature as low as possible while the sample is heated gradually from inside to outside. As a result, higher diffusion and reaction rates are obtained. X-ray diagrams showing the thermal decomposition of new phase are presented in appendix A.1.

3.3.6. Ball Milling Study with ReB_2

During the last decade nano materials moved more and more into the center of interest due to their unique electrical, magnetic and optical properties revealing significant differences compared to their bulk analogues. Therefore, ball milling was

applied on ReB_2 powders with the purpose of reducing the grain size from micrometer to nanoscale.

Ball milling studies introduces a considerable stress as changing their particle sizes. Scherrer equation offers rather simple relationship between the crystallite size and peak broadening. Size and strain broadening show different θ dependence; therefore, Hall-Williamson proposes more sophisticated method for separating size and strain broadening. Equation 4.4 illustrates the Scherrer equation and equation 4.5 displays Hall-Williamson equation. Using Hall-Williamson equation it is possible to develop a plot which gives the size and microstrain effect [35].

$$B(2\theta) = \frac{K\lambda}{L\cos\theta} \qquad \text{Eq 4.4}$$

where B is peak width in radians, K is the dimensionless shape factor usually 1, λ is the wavelength, 1.5405 nm for Cu$K\alpha$ radiation, and L is the crystallite size.

$$FW(S)\times\cos(\theta) = \frac{K\times\lambda}{Size} + 4\times Strain\times\sin(\theta) \qquad \text{Eq 4.5}$$

where FW is the full width at half maximum and normally referred as FWHM. For this study, for the sharper peaks, Lorentzian distribution is applied for peak fitting and FWHM values were calculated according to those data. FWHM x Cosθ values were plotted with respect to Sinθ. Linear fit and standard deviation calculations are performed with MATLAB and the programming details were given in appendix 4.? Slope gives '4 x Strain' and y-intercept gives '(K x λ) / size'. Figure 3.21 and figure 3.22 displays Hall-Williamson plot of ReB_2 treated with 1000 rpm and 300 rpm at different times, respectively.

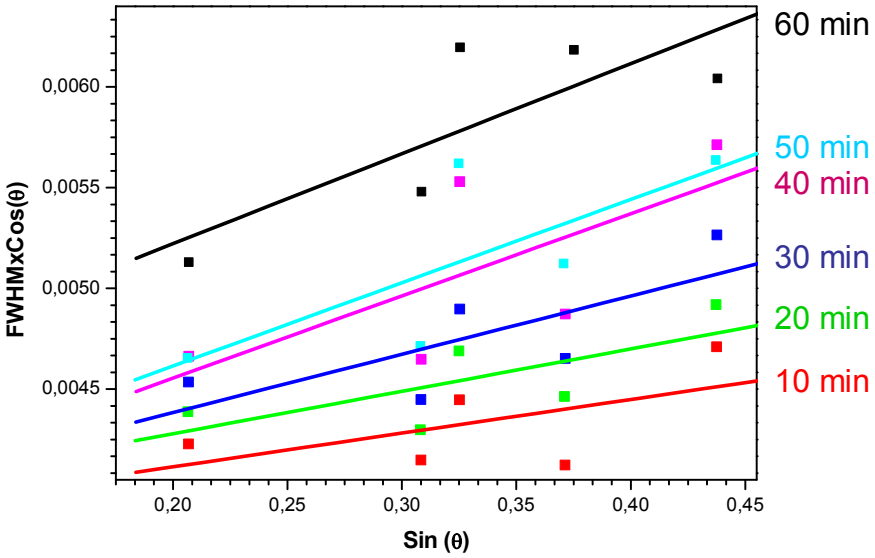

Figure 3.21 Hall-Williamson plot of ReB_2 treated at 1000 rpm at various times.

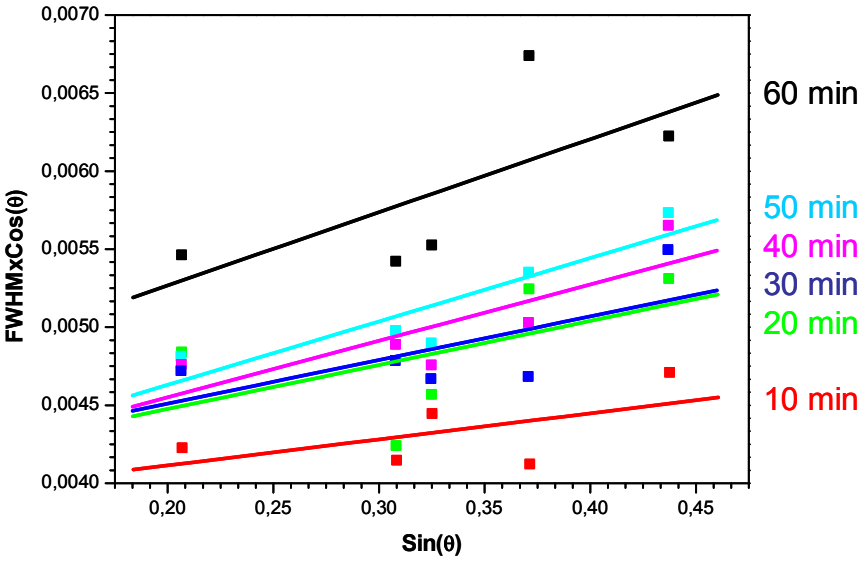

Figure 3.22 Hall-Williamson plot of ReB_2 treated at 300 rpm at various times.

Equation for each linear fit is defined as y = A*x + B where A is slope and B is y-intercept. Calculations were performed for 1000 rpm and 300 rpm and the resulting values were given in table 3.2 and table 3.3, respectively.

Table 3.2 Hall-Williamson values of ReB_2 treated with 1000 rpm.

Treatment time (min)	A (slope)	B (intercept)	Standard Deviation
Unmilled	0.00078	0.00165	0.00023
10	0.00167	0.00374	0.00011
20	0.00210	0.00378	0.00014
30	0.00289	0.00380	0.00019
40	0.00408	0.00386	0.00027
50	0.00433	0.00423	0.00036
60	0.00487	0.00447	0.00033

Table 3.3 Hall-Williamson plot values of ReB_2 treated with 300 rpm.

Treatment time (min)	A (slope)	B (intercept)	Standard Deviation
Unmilled	0.00078	0.00165	0.00023
10	0.00167	0.00378	0.00011
20	0.00282	0.00391	0.00018
30	0.00296	0.00395	0.00018
40	0.00382	0.00401	0.00024
50	0.00383	0.00406	0.00019
60	0.00468	0.00433	0.00031

Figure 3.23-24 and figure 3.25-26 show the effects of milling time on size and strain of 1000 rpm milled sample and 300 rpm milled sample, respectively. Ball milling process induces some strain in the specimens and increasing the milling time increases the microstrain. On the other hand, the decrease of the particle size is associated with an

increase of the dislocation density. Since the microstrain generally follows the features of dislocation density, it increases as the grain size decreases.

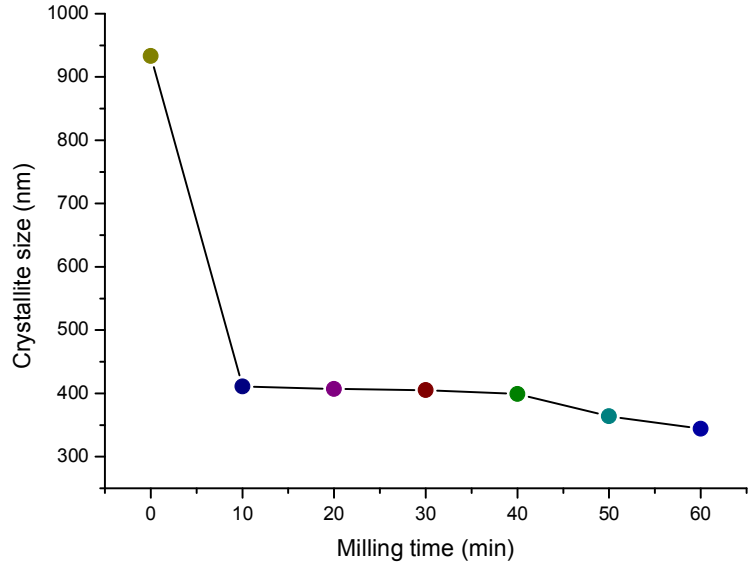

Figure 3.23 Variation of crystallite size of 1000 rpm treated sample as a function of milling time

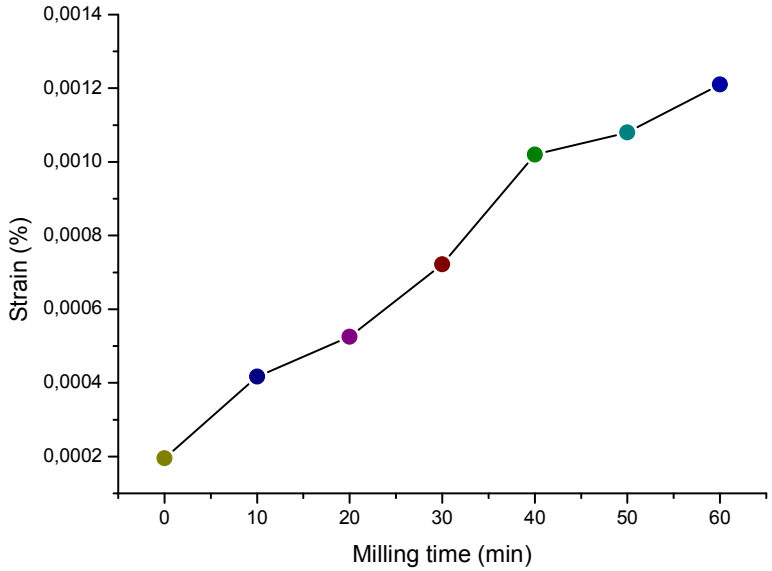

Figure 3.24 Variation of strain of 1000 rpm treated sample as a function of milling time

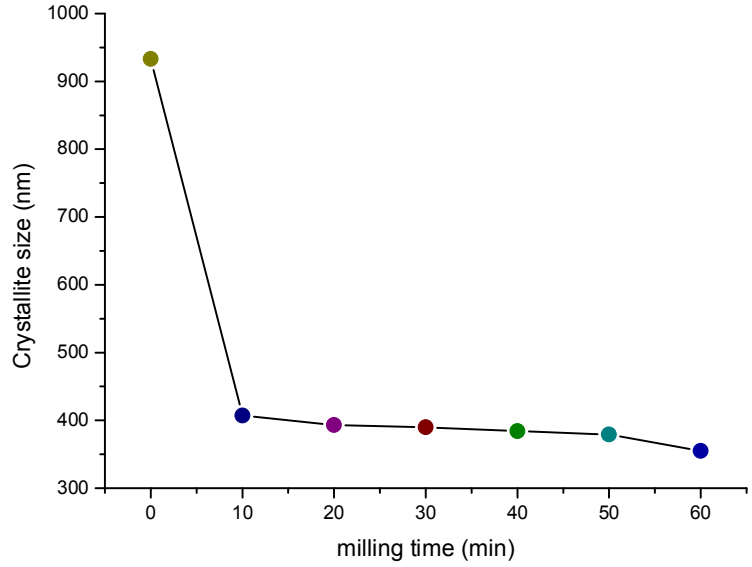

Figure 3.25 Variation of crystallite size of 300 rpm treated sample as a function of milling time

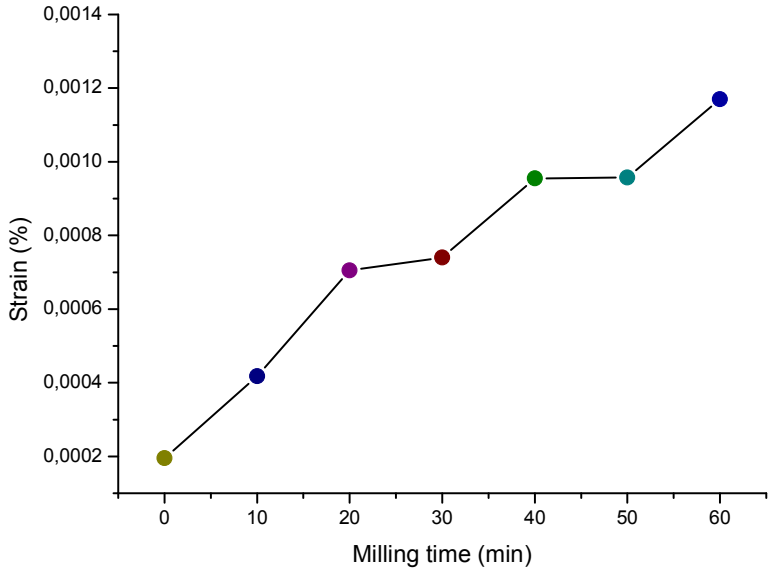

Figure 3.26 Variation of strain of 300 rpm treated sample as a function of milling time

Particle size did not vary markedly for samples treated with 1000 rpm and 300 rpm. Smallest particle sizes obtained were 344 and 355 nm, respectively. However, microstrain values yielded higher values when 1000 rpm was employed. It can be concluded that 300 rpm is preferable for reducing the particle size of superhard ReB_2 from 1μm to 355 nm. In this study zirconium oxide ball milling equipments were used; since the sample material is significantly harder than ZrO_2, the size reduction is expected to result primarily from the friction of ReB_2 particles among each other. As a future work, different milling equipments (such as tungsten carbide) will be applied aiming to improve the obtained particle size values of ReB_2.

Chapter 4

4. Clathrate-I Compound: K_8Ge_{46}

4.1 Introduction

Dictionary definition of clathrate means *a solid compound containing molecules enclosed within the crystal structure of the other component* [36]. Clathrates are 'cage' compounds in which atoms or molecules are trapped into the structure of the bigger molecule. Here, the trapped atom or molecule is called as guest and the other molecule is called as host [37]. First published clathrate compound was a gas hydrate with the suggested formula of $Cl_2(H_2O)_{10}$ [38,39]. However, after hundred years the formula corrected as $(Cl_2)_8(H_2O)_{46}$ and named as ice clathrates [40]. After a decade later, Si clathrate was discovered with the compound of Na_8Si_{46} and that discovery pulled the attention on the other group 14 elements such as C, Ge, Sn and Pb. As a consequence, in 1969, germanium and tin clathrates were synthesized from the fusion of pure elements with the formula of K_8Ge_{46} and K_8Sn_{46} respectively [41,42].

There are two types of clathrate compounds with the general formulas M_8X_{46} and $M_{24}X_{46}$ referred to as type-I and type-II, respectively. Here, M stands for the guest atom and X stands for the host. Type-I clathrate compounds crystallize in a simple cubic lattice with space group *Pm*3*n* and their structure is shown in Figure 4.1 with the representations of building blocks, layers and unit cell [43].

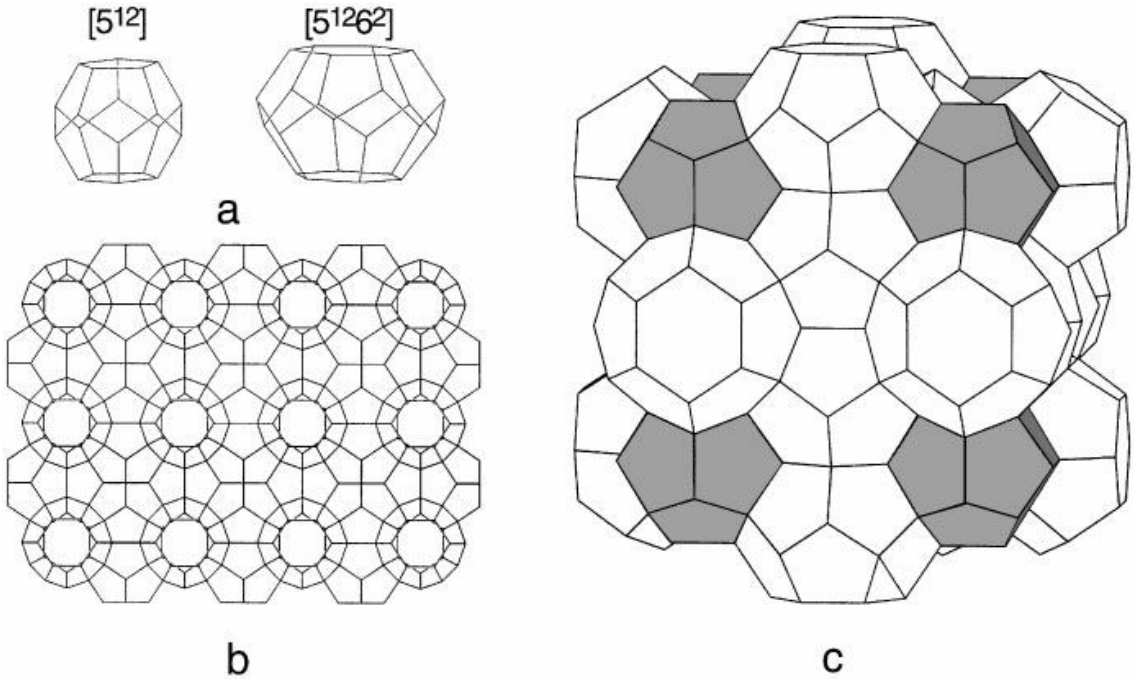

Figure 4.1 a) Building units of clathrate-I structure, the 20-atom pentagonal dodecahedron [5^{12}] with 12 pentagonal faces and the tetrakaidecahedra [$5^{12}6^2$] with 12 pentagonal and 2 hexagonal faces, **b)** Clathrate-I layer **c)** Polyhedral representation of the clathrate-I unit cell

In recent years, there has been a growing interest for the synthesis and characterization of new clathrate compounds due to the discovery of their superconducting and thermoelectric properties. They nestle high thermoelectricity low thermal conductivity which can be used for the industrial applications. Clathrate compounds are small and they are good candidates for miniaturized semiconducting devices [44]. Their synthesis is usually carried out at 650 ^oC and 10^{-5} mm Hg pressure over a period of one to three weeks. Such a synthesis method is expensive and time taking for industrial scale production. In this study, we propose a method to synthesize the type-I clathrate K_8Ge_{46} at low temperatures (235 K) without any pressure application. Synthesis starts with the precursor K_4Ge_9 and liquid ammonia is used as a solvent. K_4Ge_9 was prepared within 5 hours and the complete

synthesis of clathrate compound took one day. Characterization of the final product was done by X-ray powder diffraction.

In the second part of the study, microwave induced plasma technique was applied for the synthesis of the clathrate compound with K_4Ge_9 as precursor. Clathrate formation is confirmed together with elemental germanium as byproduct. Proposed preparation method reduces the reaction time to 20 minutes and larger scale synthesis seems to be possible.

4.2 Experimental Procedure

4.2.1. Synthesis of K_8Ge_{46} at Low Temperatures

The motivation for this study came from the report '*Oxidation of M_4Si_4 (M = Na, K) to Clathrates by HCl or H_2O*'. in which the well-known intermetallic compounds Na_4Si_4 and K_4Si_4 were oxidized by protic agents (i.e. water vapor and HCl (g)) at 673 K to yield surprisingly the clathrate M_8Si_{46} (M = Na, K), as described in equation 4.1.

$$11.5\ M_4Si_4 + 38\ HCl \rightarrow M_8Si_{46} + 38\ MCl + 19\ H_2 \qquad \text{Eq 4.1}$$

In the present study, the experiment was modified by using K_4G_9 and NH_4Cl as precursor and protic agent, respectively. In addition liquid ammonia introduced as solvent which helped to reduce the reaction temperature markedly. The chemical reaction which is expected to take place is:

$$46\ K_4Ge_9\ (sol) + 108\ NH_4Cl\ (sol) \rightarrow 9\ K_8Ge_{46}\ (s) + 108\ KCl\ (sol) + 54\ H_2\ (g) + 108\ NH_3\ (g) \qquad \text{Eq 4.2}$$

The precursor, K_4Ge_9, was synthesized from stoichiometric amounts of elemental K and finely ground powder of Ge in welded tantalum ampoules. To exclude any air and moisture penetration, the tantalum ampoules were placed into an outer silica ampoule and sealed under vacuum. The sample was heated up to 750 ^oC within 5 h and annealed for additional 5 h and followed by slow cooling to room temperature (25^oC). The black to dark red colored final product K_4Ge_9 is very sensitive to air and moisture and must be handled under inert conditions, i.e. Glove box; Ar, $H_2O \leq$ 1ppm, $O_2 \leq$ 1ppm.

The solvent liquid ammonia is commercially available as ammonia gas containing 1-3% water. Due to the extreme moisture sensitivity of the precursor, ammonia gas was condensed onto metallic sodium and freshly distilled prior to use.

For the main reaction, a total of ca. 1g of the precursor and the oxidizing agent NH_4Cl were mixed in molar ratio of 1:2 and placed into a pyrex tube equipped with a vacuum valve on top. The tube was then attached to the vacuum line and evacuated with an oil pump until $p \approx 10^{-3}$ mbar. Dry ammonia gas was condensed onto (ca. 20 mL) by using liquid nitrogen as cooling bath. The solid mixture was transferred into another dewar vessel containing an ethanol-liquid nitrogen bath as cooling medium. The reaction tube was connected to the vacuum line and then to the overpressure manometer consisting of an U-tube filled with mercury. The dewar vessel with the reaction mixture was allowed to warm up. After liquefaction at ca. -78 ^{o}C, a dark red solution was formed. The color faded away with the start of the redox reaction at ca. - 38 ^{o}C. Hydrogen and gaseous ammonia which evolved during the reaction were removed via mercury overpressure manometer. After one day of total reaction time, a gray product was obtained insensitive to air and moisture. The identification of the final product was done by X-ray powder diffraction, indicating the coexistence of the target phase K_8Ge_{46} and elemental Ge, in addition to KCl as main component.

Figure 4.2 a) NH_3 inlet; b) Pyrex reaction tube was placed into liquid nitrogen-ethanol mixture

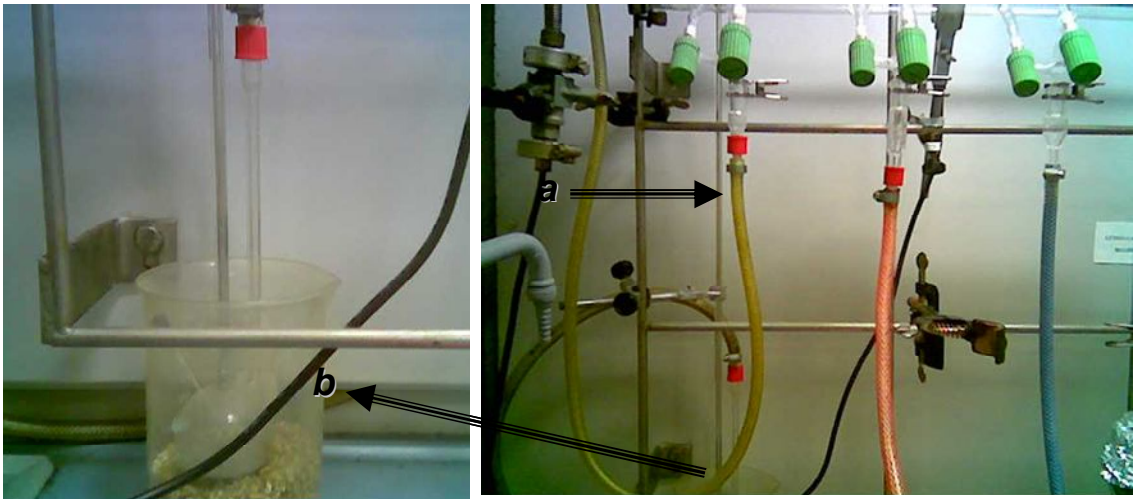

Figure 4.3 a) Gas Purge **b)** Mercury bubbler

The final product was extracted with ammonia. Contrary to K_4Ge_9, K_8Ge_{46} was not soluble in ammonia. So, the clathrate compound remained on the sintered glass and residue was collected with ammonia at the bottom. Bottom part cut by torch and the clean powder collected for characterization.

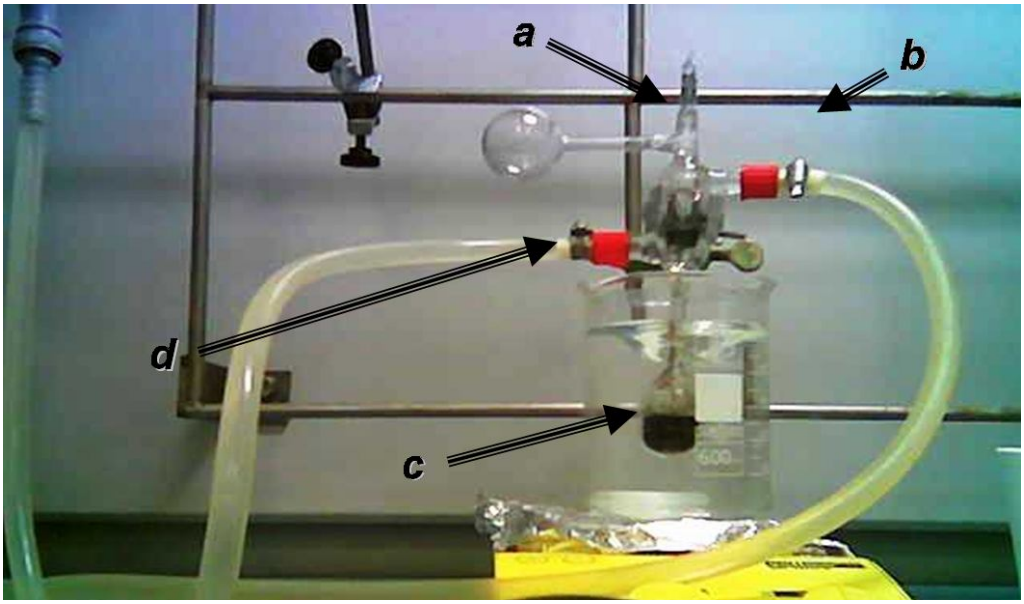

Figure 4.4 a) Soxhlet; b) water outlet c) liquid ammonia d) water inlet

The main experiment was repeated but starting from different molar ratios of the reactants. In all cases the reaction product turned out to be a mixture of clathrate and Ge (Fig. 4.5).

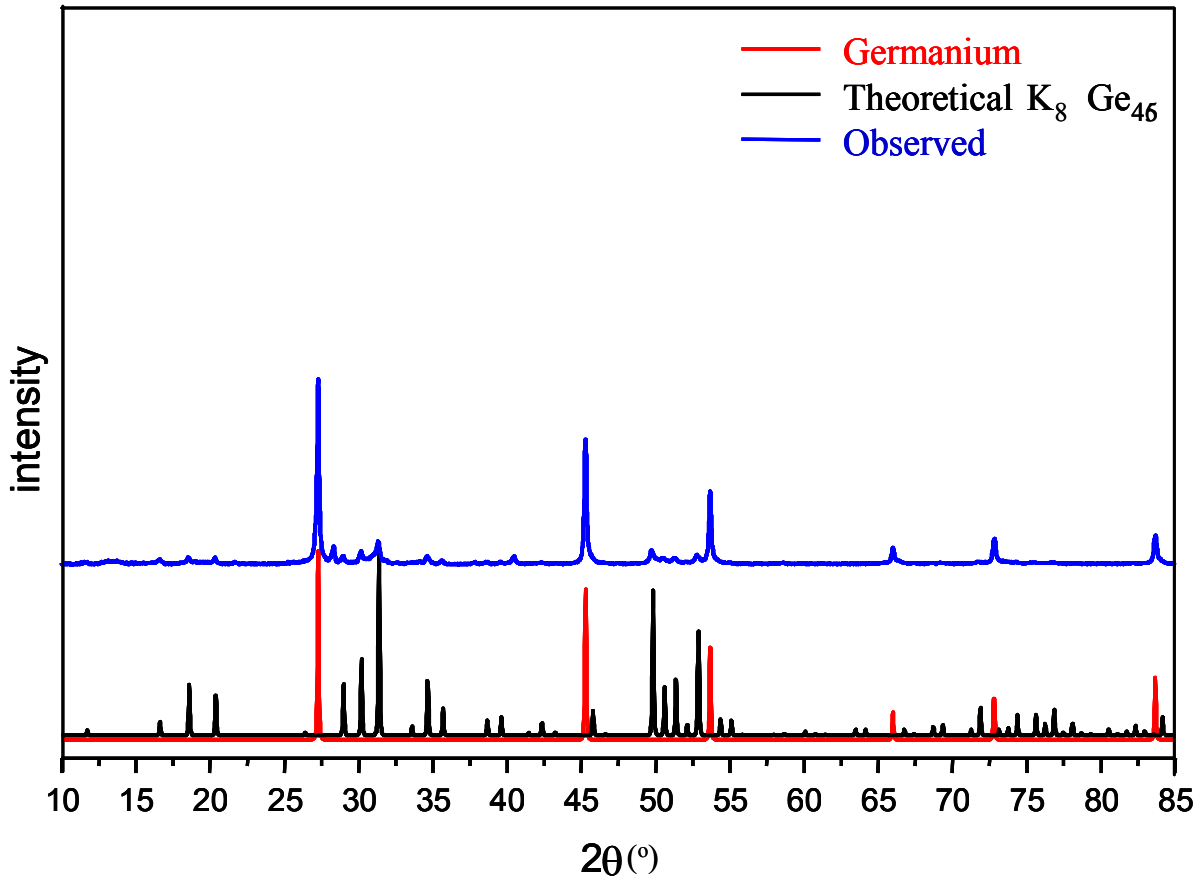

Figure 4.5 X-ray powder diagram of the product from reaction in liquid ammonia in comparison with calculated ones for K_8Ge_{46} and Ge.

4.2.2. Synthesis of K_8Ge_{46} with Microwave Induced Plasma

Due to contamination by elemental Ge, the synthesis attempts for phase pure K_8Ge_{46} at low temperatures was only partially successful. Since all conventional wet and dry chemical preparation methods were already applied, an unusual synthesis route should be favored yielding K_8Ge_{46} free of Ge. The method of choice was the microwave induced plasma technique with K_4Ge_9 as precursor, and hydrogen plasma serving as protic agent, i.e. "H^+ supplier". The results are astounding, showing a dramatic decrease

in the formation of the byproduct germanium with respect to the target compound K_8Ge_{46}. The plasma conditions applied in the syntheses and the resulting products are summarized in Table 4.1.

Table 4.1 Power values and different treatment times and their results are presented

Power Values (W)	**Time (Min)**	**Results**
600 W	20	Clathrate & Germanium
600 W	40	Clathrate ↑ & Germanium ↓
900 W	40	Clathrate & Germanium ↑
1200 W	40	Only Germanium
1200 W	20	Only Germanium

According to these findings, the amount of Ge as byproduct is minimized when a power output of 600 W was employed for 40 min. Higher power values, such as 1200 W results in a complete decomposition of the target compound K_8Ge_{46}. Therefore, a reaction series was started maintaining a constant output of 600 W but varying the reaction time until the formation of elemental germanium was minimized.

In a typical reaction batch, 0.250 g of K_4Ge_9 was placed into an alumina crucible and transferred into a reaction tube of silica. After evacuation to $p \approx 10^{-3}$ mbar, the hydrogen gas purge was started (flow rate 100 sccm) and the plasma ignited using different power outputs. The final product(s) - K_8Ge_{46} and Ge - are air and moisture insensitive, can be handled under atmospheric conditions. The X-ray powder diagrams representing the products from both K8Ge46 syntheses – i.e. via reaction in liquid ammonia and microwave plasma - are comparatively depicted in Fig. 4.6.

4.3 Results and Discussion on Clathrate-I Compound: K_8Ge_{46}

4.3.1. Comparison of Synthesis of K_8Ge_{46} with Ammonia and Microwave Induced Plasma

The X-ray powder diagrams representing the products from both K8Ge46 syntheses – i.e. via reaction in liquid ammonia and microwave plasma - are comparatively depicted in Fig. 4.6.

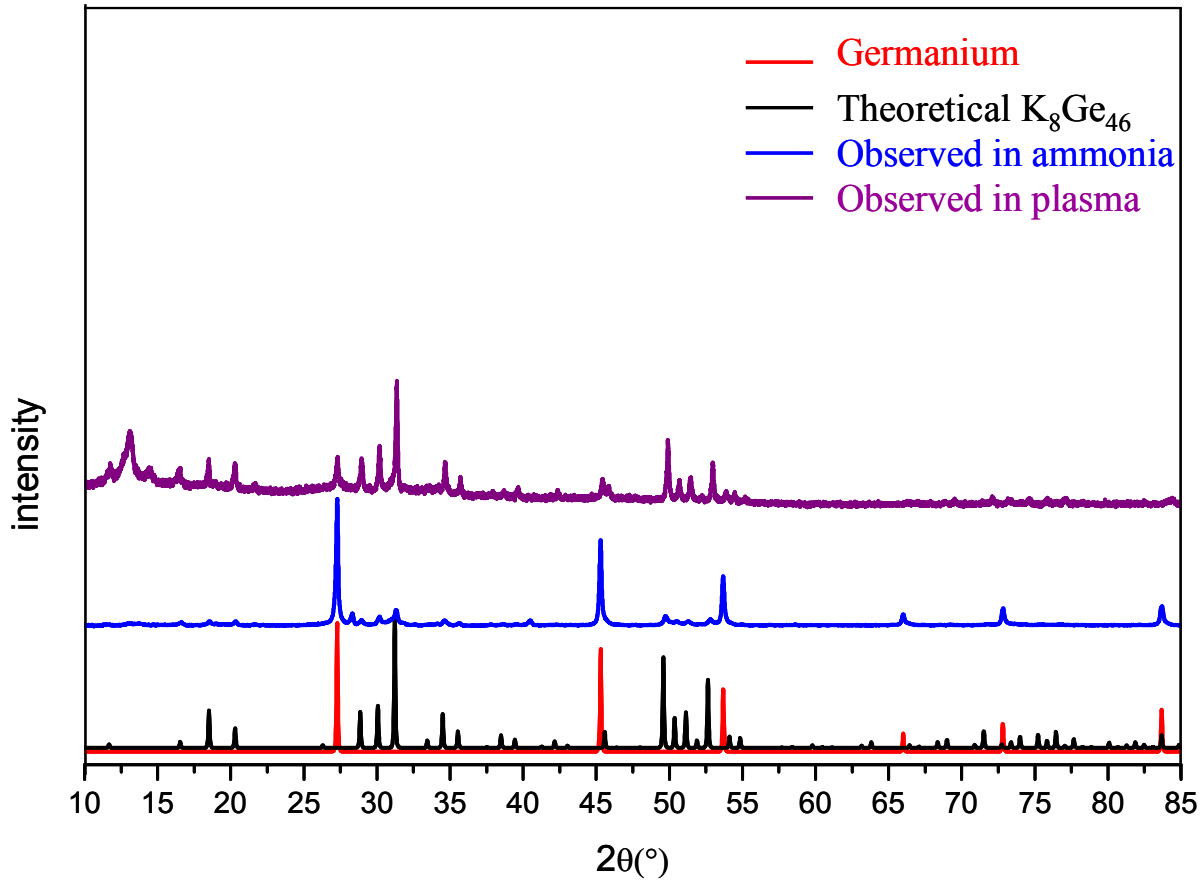

Figure 4.5 Comparison of X-ray diagrams of the clathrate K_8Ge_{46} synthesized in liquid ammonia and via microwave induced plasma

The comparison of the two methods reveal, that the microwave induced plasma technique is a much less demanding and comfortable synthesis tool allowing an easy control on both the reactions parameters, as well as the rate of formation of the products. Also the reaction time is very short. The only disadvantage is that the present microwave induced plasma system is only employable for gram scales, meaning that further studies are necessary so that its industrial application is possible.

Chapter 5

CONCLUSION

Amorphous boron was the common component in almost all investigated systems so that the use of high purity boron was of first priority. For this purpose, the commercially purchased amorphous boron (85.6 wt%) containing a magnesium impurity of 12% was exposed to chlorine gas at elevated temperatures (1073 K). At the end of this treatment the purity value of boron could be increased up to 97.6% while the magnesium content was reduced below 0.8 %. This product served as the boron source in all experiments.

The main thesis consists of three separated parts. The first one is focused on synthesis and characterization of transition metal borides in the ternary Ta-Co-B, Ta-Ni-B, Ta-Re-B, Nb-Re-B, Hf-Ni-B, Ta-La-B and Re-Ni-B. The employed preparation technique was the solid state high temperate reactions performed in a home-made arc melting furnace. Characterization and identification of the obtained phases was done by X-ray powder diffraction and chemical analyses. In case of Nb-Re-B system, niobium successfully substituted the tantalum atoms of $Ta_3Re_3B_4$ and a novel ternary compound was synthesized with the composition of $Nb_3Re_3B_4$. Except for the Re-Ni-B system, all products were phase mixtures of ternaries with already well-known binaries. A novel ternary compound was isolated with the nominal composition Re:Ni:B = 1:1:1. Optical micrographs confirmed that new “phase” comprised two different ternary borides, the shiny one being Re and the dark one Ni-rich, respectively. The analysis of the rhenium rich phase was performed with WDXS yielding an approximate composition of $Re_{20}Ni_3B_{11}$. Based on this, the empirical formula of the Ni-rich dark phase was calculated to $ReNi_{6.67}B_4$. Re:Ni:B = 1:1:1 could also be synthesized using the lead flux method explained below.

Technology requires the usage of enduring materials and ReB_2 is one of them, due to its superhardness - second hardest compound after diamond - and refractory properties. There are only few works published on the syntheses of ReB_2 and they are usually performed via solid state reaction of the elements at high temperatures and/or pressure coupled by long annealing time.

In this thesis, ReB_2 was prepared using two novel synthesis routes: from reaction of the elements in molten metal (flux) and via microwave induced plasma method. The application of metal flux as medium for chemical reactions is quite old. The classical examples are molten aluminum and tin while the use of lead as flux was restricted exclusively to growth of single crystals, up to now. The synthesis of rhenium diboride in the present study is the first time ever, in which lead flux is applied as preparative tool. For this purpose the stoichiometric mixture of the starting elements were annealed in molten lead (molar ratio Re:B:flux Metal = 1:2:10; alumina crucible) for 5h at 1073 K, which is the lowest reaction temperature recorded for ReB_2, yet. Molten aluminum (1673 K, dwell time: 12h) has previously been employed as flux for the same purpose, but yielding only the ternary $ReAl_{0.011}B_{1.85}$. Beside the quite moderate reaction temperatures, synthesis in lead flux has the advantage of having comparatively short reaction time and most of all the obtained product is phase pure, free of lead. The latter was verified by a series of ICP-OES and EDXS measurements clearly proving that no lead was incorporated into target compound ReB_2. Based on the results from ICP-OES and wet chemical analyses, the empirical formula was calculated to $ReB_{1.98}$. The minor deviation with respect to the theoretical composition (ReB_2) is tolerable and lies within the range of standard errors.

The microwave induced plasma technique is the second novel preparative method introduced in this study to investigate the formation of ReB_2 under unconventional conditions, which is the plasma state. For the main reaction, a homogenous mixture of the educts (molar ratio Re:B = 1:2) was exposed to two different plasma gases - argon and hydrogen – at different flow rates and power output. The approximate temperature of the plasma gas was measured with a thermocouple

inserted the silica reaction chamber. The maximum temperatures detected for the hydrogen and argon plasma were 990 K and 700 K, respectively. The significant differences in the plasma temperatures are in good accordance with the experimental results indicating the successful formation of ReB_2 took place only in hydrogen plasma, while the educts in Ar plasma remained unreacted. The maxiumum yield was achieved when hydrogen plasma with a power value of 1200 W and the reaction time of 30 min were employed. The phase analysis of the final products was performed by the X-ray powder diffraction method revealing that the formation of ReB_2 was accompanied by a foreign phase. Mass spectroscopic measurements exclude hydrogen as possible contamination source. The results of the resynthesis experiments but using amorphous boron free of Mg, proved that the formation of the new phase was due to an "intrinsic" reaction between rhenium and boron and not initialized by the impurities in the used amorphous B, containing 0.8% Mg as main impurity. DTA measurements confirmed that foreign phase is boron-rich decomposing surprisingly at 948 K to yield ReB_2 and elemental boron. The latter findings give also a plausible explanation why the new phase has never been mentioned in previous reports. Very likely, annealing process and high temperatures are responsible for the complete thermal decomposition while the conditions in the plasma - i.e. reactive hydrogen species and moderate temperatures - favored the unexpected formation of the foreign compound.

The conventional synthesis method for most of the binary and ternary transition metal borides - including ReB_2 - is the high temperature solid state reaction in arc melting furnace followed by long annealing time. However, there has been no report available yet, mentioning the effect the initial molar ratios of the reactants and particularly that of boron on the phase purity of the target product. That is interesting, since it is known that almost all conventional prepared ReB_2 samples are contaminated by at least one foreign phase of unknown composition. For this purpose, a systematic phase analytical study was started in which the correlation between boron excess and the chemical composition of ReB_2 was investigated. The results show that starting from

molar ratios of Re:B = 1:4 to 1:7 yield the best output with respect to phase purity of ReB_2

The clathrates are known for more than 100 years. The discovery of their unusual superconducting and thermoelectric properties in the last decade, however, moved this class of compounds in center of growing industrial interest. Their synthesis usually occurs at high temperatures connected with long annealing time which is not feasible for large scale industrial production. For this purpose two new preparative routes were worked out and applied on the model clathrate-I compound K_8Ge_{46}. The low temperature method implies the mild oxidation of the well-known precursor K_4Ge_9 with NH_4Cl in liquid ammonia as solvent at -38 °C. and ammonia condensation. In the alternative microwave induced plasma technique, K_4Ge_9 was again employed as precursor while hydrogen plasma acted as protic agent. In both cases, the formation of the final product was accompanied by the presence of elemental germanium. Hydrogen plasma was the “method of choice” giving the highest yield of clathrate compound and the lowest value for the byproduct elemental germanium.

Chapter 6

EXPERIMENTAL METHODS and THEORETICAL CONCEPTS

6.1 Introductory Remarks

The studied systems were sensitive to impurities in amorphous boron; therefore, a systematic study was performed to purify the purchased amorphous boron which was synthesized with metallo-thermal reaction (Mg impurity). Magnesium impurity was removed by treating with chlorine. Moreover, for the arc melting synthesis home-made arc melting furnace was built and optimized. Those two things are really important in this thesis; therefore, they were studied thoroughly.

i) Purification of Amorphous Boron

There are several ways for synthesizing the elemental boron such as reduction of boron halides with hydrogen, pyrolysis of boron halides and hydrides etc. However, metallo-thermal method (Moissan) is the main commercial production technique. Boron used in this thesis was supplied from H.C. Starck and Pavezyum Company. H.C. Starck boron is used for the comparison, but mainly boron from Pavezyum is used in the syntheses. Boron was synthesized according to Moissan method. Boron-oxygen compounds reduced with magnesium powder or turnings. For the complete conversion to borates, excess B_2O_3 was required. Reactions are given in equation 6.1.

$$B_2O_3 + 3Mg \rightarrow 2B + 3MgO$$

$$2B_2O_3 + 3Mg \rightarrow 2B + Mg_3(BO_3)_2$$

$$4B_2O_3 + 3Mg \rightarrow 2B + 3Mg(BO_2)_2 \qquad \text{Eq 6.1}$$

Borates and oxides are removed with acid treatment. However, MgB_2, MgB_4 and MgB_{12} remained in the final product and MgB_xO_y is also reported as the main impurity sideproduct [47].

Boron with 86 % purity was supplied from Pavezyum. From the X-ray powder diagram, MgB_{12} was determined as the main purity. However, since MgB_xO_y is amorphous, there is no information about its contamination. Boron and magnesium contents were analyzed with titration method. Boron was dissolved in dilute (10 %) nitric acid and heated up to 353 K until a clear solution is obtained. Boron is converted to boric acid and titrated with 0.1 M NaOH. Optimization of titration methods were performed with boric acid solution with the known concentration. According to those optimizations, the pH value should be 6.5 and mannitol should be used to convert the weak acid into strong acid for better end point detection. Magnesium was titrated with EDTA. Boron content determined as 85.6%, afterwards, it was treated with chlorine gas in order to remove magnesium from the system. 85.6 % boron was placed into tube furnace within aluminum oxide crucible. Argon gas purged until the system heated up to the desired temperature. When the aimed temperature was obtained, argon gas purge stopped and chlorine gas purged for a specified time. Until system cools down to room temperature, argon gas purge was carried. Product was washed with 10% HCl acid. System was heated up to 373 K because anhydrous magnesium chloride dissolves better when heated. The procedure has been described in US3001855.However, optimization results were not given. We performed several experiments to optimize the system. Optimization results are given in Figure 6.1.

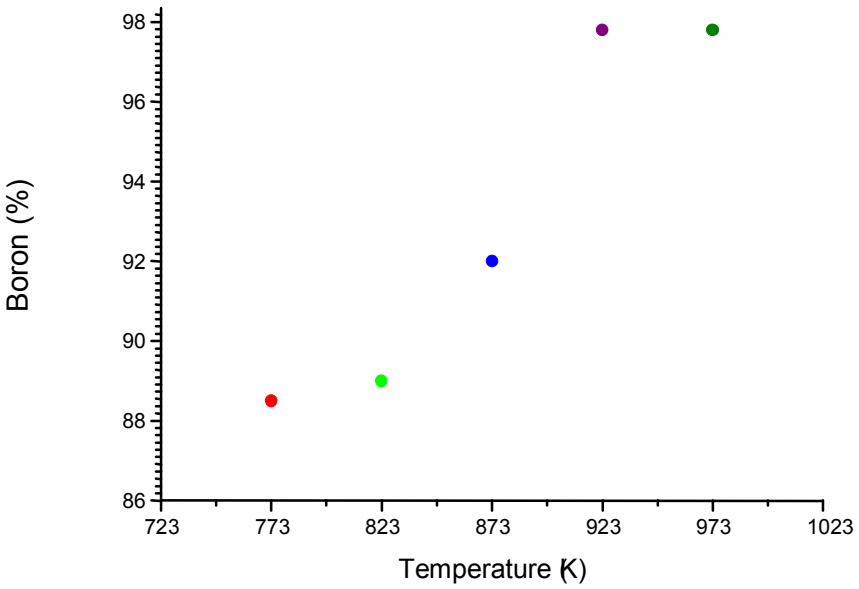

Figure 6.1 Temperature optimization of Chlorine experiment (20 min, 1000 ml/min)

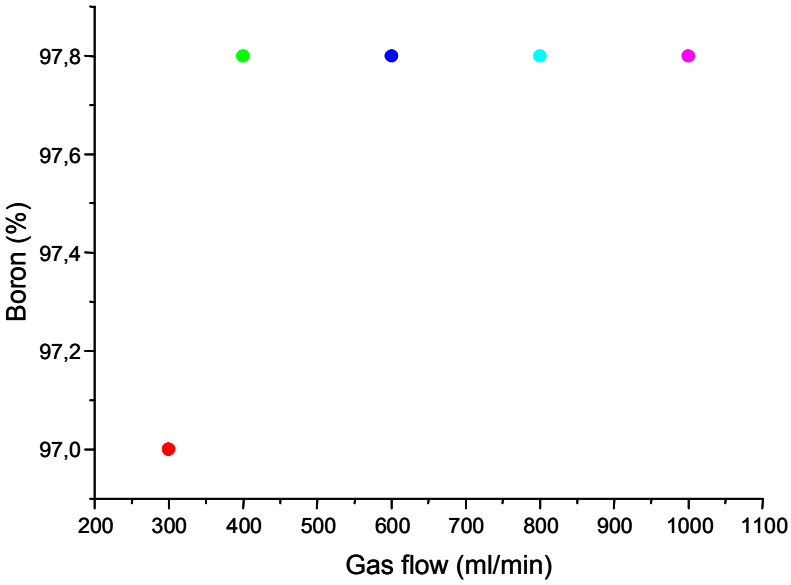

Figure 6.2 Gas Flow rate optimization (20 min, 923 K)

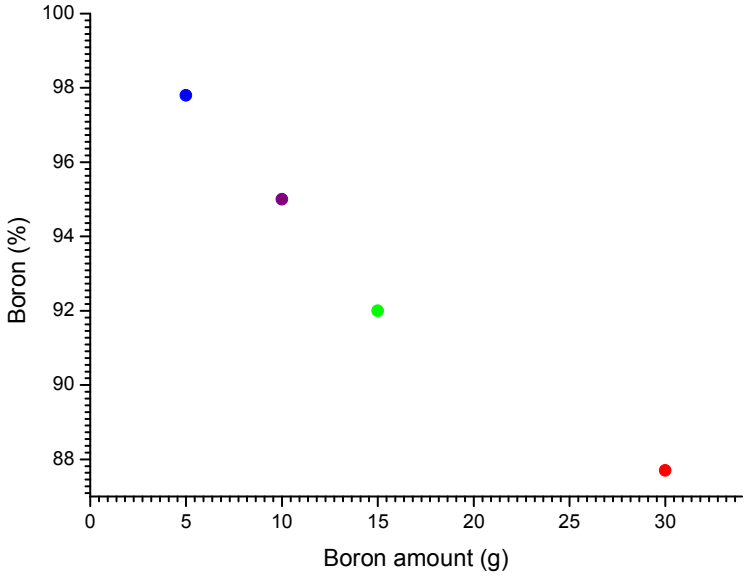

Figure 6.3 Boron amount optimization (923 K, 20 min, 400 ml/min)

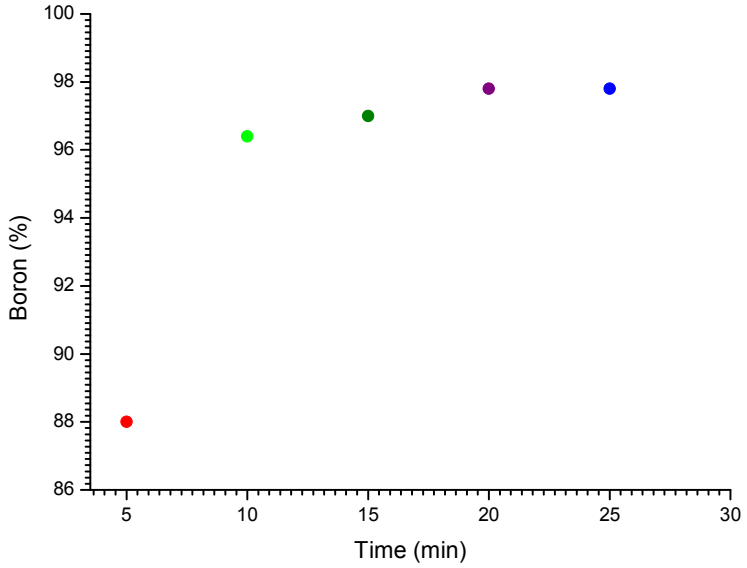

Figure 6.4 Time optimization (923 K, 400 ml/min, 5g)

The best result for boron content of 5 g sample was obtained at 923 K with a flow rate of 400 ml/min and 20 minute reaction time. X-ray diagram in figure 6.5

compares the 86% amorphous boron with MgB_{12} and it also illustrates the boron after chlorine treatment. For the rest of the experiments, purified boron was used.

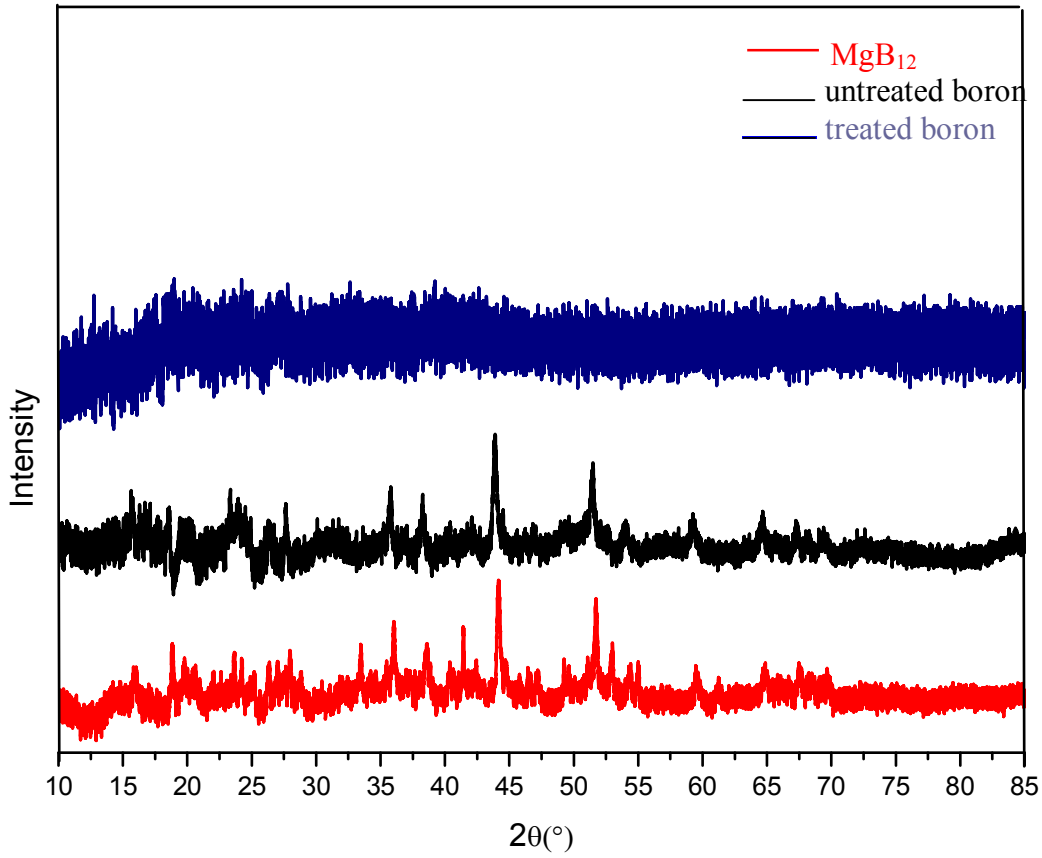

Figure 6.5 Chlorine treated sample and untreated sample were compared with MgB_{12}

During the arc melting synthesis and microwave induced plasma synthesis, new phases were detected. In order to be sure of new phases are not coming from boron impurity (magnesium), amorphous boron was cleaned as much as possible. Furthermore, amorphous boron was synthesized with another method which does not yield magnesium impurity and obtained new phases checked again.

In the second method, amorphous boron was obtained with the pyrolysis of diborane which was reported as a good method for the synthesis of high purity

amorphous boron. It is a promising method for the synthesis of 99% purity boron. However, at low temperatures (~523 K) yield of those reactions are decreased with the formation of higher boranes [48]. Equation 6.2 gives the higher boranes formed during the synthesis .

$BH_3 + B_2H_6 \leftrightarrow B_3H_9$

$BH_3 + B_3H_9 \leftrightarrow 2B_2H_6$

$2B_3H_9 \leftrightarrow 3B_2H_6$

$B_3H_9 \rightarrow B_3H_7 + H_2$

$BH_3 + B_3H_7 \leftrightarrow B_4H_{10}$

$B_2H_6 + B_3H_7 \leftrightarrow BH_3 + B_4H_{10} \leftrightarrow B_5H_{11} + H_2$ Eq 6.2

First, diborane was synthesized with ball milling. Afterwards, it was decomposed to diborane at 353 K and successively to amorphous boron at 1123 K. Equation 6.3 gives the reactions [49].

$ZnCl_2 + 2NaBH_4 \rightarrow Zn(BH_4)_2 + NaCl$

$Zn(BH_4)_2 \rightarrow B_2H_6 + Zn + H_2$

$B_2H_6 \rightarrow 2B + 3H_2$ Eq 6.3

With the proposed method, amorphous boron was synthesized without magnesium impurity. Syntheses performed with microwave induced plasma and arc melting were compared by using both types of amorphous boron.

ii) Arc Melting Furnace

Centorr vacuum industries 5SA/38042-A arc melting furnace motivated the design of home-made arc melting furnace. Centorr arc melting furnace consists of a resistor box, a power supply and a set of water cooled power cables to bring power and water to the furnace. Its operating temperature is greater than 3723 K [50]. Figure 6.6 demonstrates the Centorr arc melting furnace placed into glove box in Max-Planck institute, Dresden.

Figure 6.6 Centorr arc melting furnace placed into glove box.

Following the Centorr arc melting furnace, simple system was built. This furnace contains a silica cover which allows the observation of process, a power supply, a copper hearth and water cooling system. Figure 6.7 displays the home-made arc melting furnace.

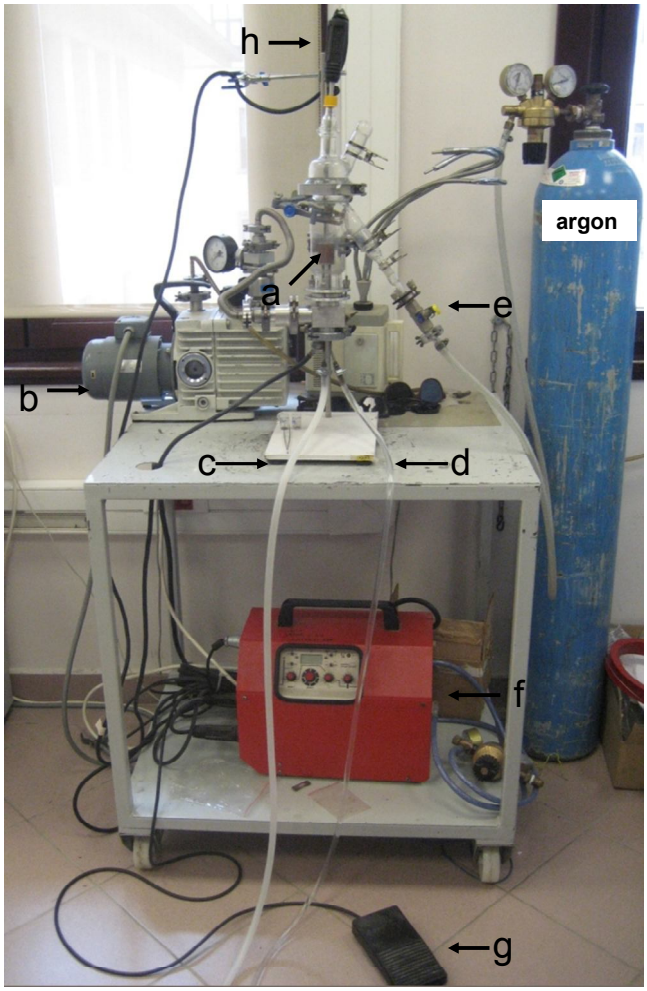

Figure 6.7 Home-made arc melting furnace a) copper hearth b) Vacuum oil-pump c) water inlet pipe d) water outlet pipe e) argon gas inlet f) power supply g) pedal h) tungsten electrode

Copper hearth was placed onto a stand which was connected to water cooling pipes. Water cooling pipes were made from teflon which stands until 600 K. Copper hearth was cooled during the reaction to prevent any damage on the copper and improving the cooling of the system. Sample was pressed into pellets at 10 kN and placed onto the copper hearth. Silica top was sealed with a ring and sealing was further improved with vacuum oil. Silica top part was equipped with a swivel ball in which carries the tungsten electrode. This allows angular movement. Since the system could

not be placed into the glove box, air and moisture were eliminated from the system by purging with an oil pump. It was vacuumed to 10^{-1} mbar and then filled with argon gas. Arc ampere was detected by several experiments.

Table 6.1 Optimization of Arc ampere

Arc ampere	**Observation**
60 A	Tungsten electrode starts melting
50 A	Arc generates without any problem
40 A	Hard to generate arc

According to the studies of *Ponomarev,* stability of the growth process strongly depends on the geometric positions of the ingot. Any deviation from axial symmetry or from horizontal position enhances the crystallization rate during arc melting processing. Crystallization growth rate can be detected by attaching a video camera and calculating the velocity of crystallization or it can also be detected by investigating the X-ray diagrams of same samples which were synthesized at two different positions, horizontal and tilted. Co_2B pellets were prepared and one of them was placed horizontally onto the copper hearth and the other one was placed as tilted onto the copper hearth. Figure 6.8 displays the X-ray diagram of horizontal and tilted samples.

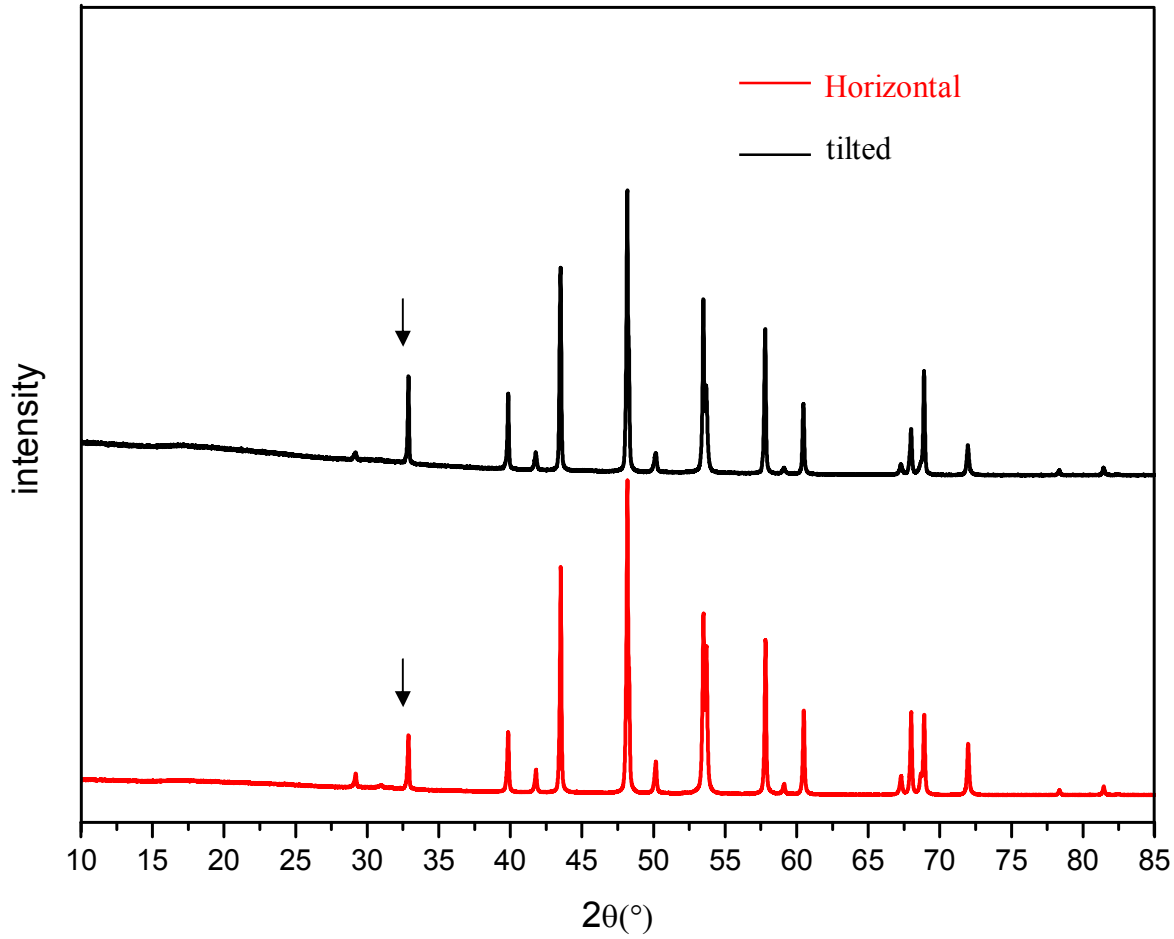

Figure 6.8 X-ray diagrams of horizontal and tilted pellets

Crystallization value was determined by comparing the intensity differences. Simply by looking at the peak at 2θ value of 32.887°, it can be concluded that the sample better crystallized at the tilted position. The peak intensities of horizontal and tilted ones are 6244 and 6637, respectively. For a better investigation, Lorentzian distributions were performed for both of the X-ray diagrams for estimating the full width at half maximum (FWHM). FWHM values of horizontal and tilted samples were 0.11897 and 0.09626, respectively. Those results are compatible with the expected results because as the peak intensity increases without any peak broadening, FWHM values decreases. Same experiments repeated several times and similar results obtained.

For the further arc melting syntheses, 50 A as arc ampere and tilted pellet position were adopted.

Syntheses of transition metal borides and clathrate compounds are very susceptible and they need a special care during the syntheses. The chemicals should be of high purity and the composition should be exact. For the clathrate compounds, any oxygen or moisture contact or contamination may lead to another compound or decomposition of them. Therefore, in order to eliminate moisture each and every glass container and preparatory apparatus (such as valves, stoppers etc) were dried in a hot air sterilizer laboratory oven which is at 393 K for minimum of 2 hours. Oxygen and moisture were reduced by antechamber operation. All the equipment and chemicals were evacuated for minimum of 30 minutes before transferring them into the glove box. The oxygen and water level of the glove box were controlled by monitoring the oxygen and water level in parts per million with minimum threshold set at $\leq$ 0.1 ppm for both O_2 and H_2O. Argon gas was used to obtain inert atmosphere in the box and its excess pressure was set to 2 mbar.

6.2 Materials and Chemicals Used, Sources and Quality

All educts, except boron, were highly pure chemicals and commercially purchased. There are only a few companies who produce boron with high purity (such as H.C. Starck) and due to the preparation of amorphous boron, final product is accompanied with magnesium impurity. Their specifications are given in table 6.2.

Table 6.2 Specifications of commercially available amorphous boron (H.C Starck)

	Amorphous Boron	**Magnesium**
Grade I	> = 95 wt%	< = 0.80 %
Grade II	> = 90 wt%	< = 6.0 %
Grade III	> = 86 wt %	< = 12.0 %

For this study, 85.6 wt% pure amorphous boron is purchased from Pavezyum Company in Turkey. Impurity of amorphous boron comes from MgB_2 and from the sub-oxides of boron such as B_6O, B_7O. Purchased boron is treated with chlorine gas and its purity is raised to 97.6 % and magnesium impurity is lowered to 0.8 %. Remaining impurity belongs to sub-oxides. Details of experimental procedure are given in section 6.1. Reaction takes place is given in equation 6.4.

$$MgB_2\,(s) + 2\,Cl\,(g) \xrightarrow[\Delta]{} MgCl_2\,(s) + B\,(s) \qquad \text{Eq 6.4}$$

For Ta-Ni-B ternary system Tantalum wires with 0.8 mm in diameter were used. Every annealing in the study was performed in Ta ampoules with 8mm in diameter. For hafnium ternary system, hafnium purchased in sponge form and was grinded with tungsten carbide mortar. Table 6.3 gives an overview of the chemicals utilized in the study, including their sources and purity grades.

Table 6.3 Chemicals used and their specifications

Elements	Atomic Weight (g/mol)	Melting Point (^oC)	Physical State	Company	Purity %
Tantalum (Ta)	180.9478	2996	powder Ampoule	ChemPur Chempur	99.9
Nickel (Ni)	58.693	1453	powder	Alfa Aesar	99.9
Cobalt (Co)	58.9332	1495	Powder	ChemPur	Alfa Aesar
Rhenium (Re)	186.207	3186	Powder	ChemPur	99.9
Niobium	92.9064	2477	Powder	ChemPur	99.9

(Nb)					
Hafnium (Hf)	178.4900	2233	Powder	ChemPur	99.9
Boron (B)	10.8110	2076		Pavezyum	86
COMPOUNDS					
Lanthanum hexaboride (LaB_6)	203.7800	2210		ChemPur	99.9
Calcium hexaboride (CaB_6)	104.9400	2235		ChemPur	99.9

6.3 Experimental Methods

6.3.1. Glove Box

Clathrate part of this study is highly sensitive to air and moisture and therefore, it requires a consistent and reliable inert atmosphere for the proper results. For those purposes, glove boxes are the most suitable devices. Those are sealed containers that provide the desired inert atmosphere. They have a transparent shield that one can see inside and two gloves are mounted onto that shield, so one can work placing their hands into it without causing any air interruption. Interference of oxygen and moisture during the transfer of used equipment and chemicals are controlled by at least one evocable antechamber. The proper evacuation requires minimum of 30 minutes. After evacuation, for an appropriate transfer the chamber is filled with an inert gas such as Argon or Nitrogen. Gas circulation is maintained by standard inert gas system (MBRAUN) and the inert gas continuously circulates between the glove box and the gas purification chamber. The free air at 283K contains 209000 ppm of oxygen and

12100 ppm of moisture and in a glove box, the standard values reported for both oxygen and moisture are less than 1 ppm. Glove boxes are equipped with an automatic regeneration system that keeps up the capabilities of the oxygen and moisture filters. A finely divided metal in our case an amorphous copper is used for the oxygen removal. While the column is heated, hydrogen/ argon mixture or hydrogen/nitrogen mixture is passed through the column and the excess oxygen is removed through that operation. Since a molecular sieve may absorb water up to 22 % of its own weight, they are used as well for removal of water through absorption.

For the experiments performed at Koç University, VAC OMNI-LAB glove box with a high purity of nitrogen atmosphere was used. For the experiments performed at Max Planck Institute in Dresden, MBRAUN glove box with a high purity of argon atmosphere was used. Figure 6.9 shows a standard glove box system [50].

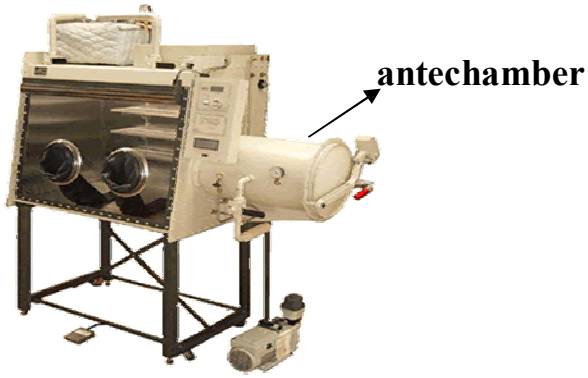

Figure 6.9 VAC-OMNI model glove box system

6.3.2. Arc Melting

Arc melting furnace was used for the syntheses of many high temperature transition metal borides and as well as for sealing of Ta ampoules that are used as a container for the reacting materials. Centorr vacuum industries 5SA/38042-A [51]arc melting device is placed into the glove box which has a cooling system with copper hearts of various

sizes and tungsten electrodes. The furnace chamber can be evacuated and it is also filled with argon gas during the synthesis. Even though compact matter is preferred for the syntheses by pressing into pallets at various pressures, many of the syntheses still require high temperatures. For that purpose, arc melting system gives the opportunity that many commercial furnaces cannot and it can even exceed its operating temperature to 3773 K. Figure 6.10 shows the arc melting system in Max Plack institute. However, here in Koç University, we built up a new arc melting system which was discussed in section 6.1.

Figure 6.10 Centorr vacuum industries arc melting system

6.3.3. Vacuum Line

A part of the study requires a clean and inert system. Vacuum line is a glassware equipment which supplies the reduced atmosphere. System has several ports and two lines. It is also equipped with an oil vacuum pump and a cold trap. 'Trap' was cooled down with liquid nitrogen and it helped to protect the pump from aggressive gases and liquids. Oil pump with the trap drew pressure down to 10^{-3} mbar. It was also connected to a mercury bubbler for gas release.

Vacuum line was used for the Type-I clathrate compound synthesis and sealing of the soxhlets. Liquid ammonia was condensed onto the mixture and whole reaction took place at the vacuum line which was described with details in Experimental 3.10.

For sealing of the soxhlets, the required pressure was between $6x10^{-3}$-$2x10^{-3}$ mbar which took approximately half an hour. After the evacuation of the vacuum line, soxhlet was connected to the vacuum line through one of the valves. In order to prevent the recrystallization of glass/quartz neck of the soxhlet, it was wiped with ethanol or acetone. Propane gas torch was used for sealing of the soxhlets.

Figure 6.11 Vacuum line

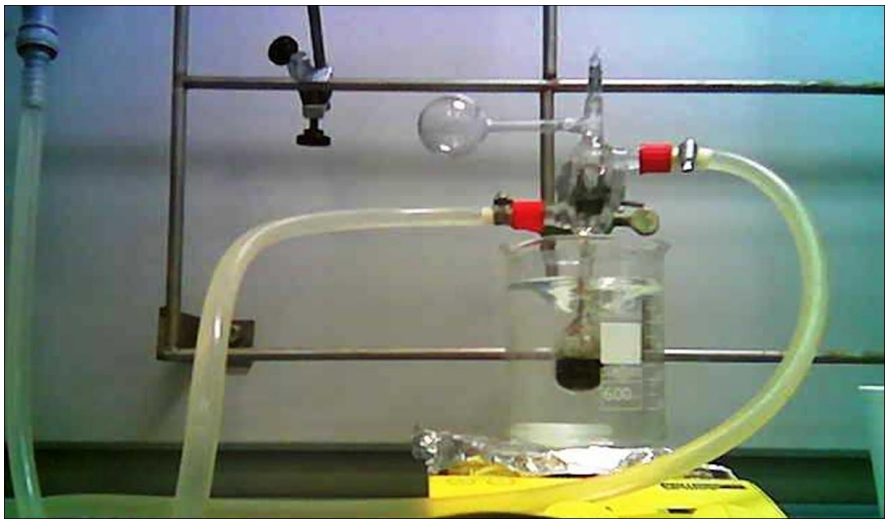

Figure 6.12 Sealed Soxhlet

6.3.4. High Temperature Annealing in Sealed ampoules and Silica tubes

Clathrate compounds were further protected from the air contamination by sealing the tantalum containers into silica tubes with a diameter of 40 mm, a length of 500 mm and a wall thickness of 1.5 mm. Figure 6.13 shows the prepared ampoules. Afterwards, reaction tubes were placed into vertical ovens for proper heat treatment.

Figure 6.13 Tantalum ampoule sealed into Silica tube and it was protected with glass wool from both sides.

After the reaction completed, sealed ampoules were transferred into the glove box and opened by breaking the silica. Then tantalum ampoule cut into pieces and sample was collected.

6.4 Materials Characterization Techniques

6.4.1. X-Ray Powder Diffraction Techniques

6.4.2. Theory

X-ray crystallography dates back to 1912, to the discovery of the diffraction of X-rays by crystals. With that discovery experimental determination of crystal structure became possible. X-ray techniques can be divided into two classes: single crystal and powder. For a good crystal structure determination, well formed single crystals should be used. Powder diffraction is not preferable for structure determination because it only gives limited amount of reflections. However, if the structure is not too complex or it is not possible to obtain single crystals, then powder diffraction can be used for characterization [52].

Furthermore, X-ray diffraction method can be used to determine quantitative phase analysis with the comparison of peak intensities, unit cell lattice parameter by indexing peak positions, microstrain and crystallite size by examining the peak broadening [53].

Before going into the details of X-ray theory, some concepts should be defined such as lattice, unit cell and crystal systems. A crystal is solid object with a basic

pattern of atoms. Those atoms repeat themselves within all three dimensions. There are three vectors describing those translations in space and their total operation forms the lattice. Smallest repeating volume of the lattice forms the unit cell and symmetry operations on the lattice forms the crystal systems. Possible considerations give seven crystal systems with varying restrictions that are shown in table 6.4 [54].

Table 6.4 Crystal systems with their restrictions

Restriction in	**cell edges**	**Cell angles**
Triclinic	None	None
Monoclinic	None	$\alpha=\gamma=90^o$
Orthorhombic	None	$\alpha=\beta=\gamma=90^o$
Tetragonal	a=b	$\alpha=\beta=\gamma=90^o$
Trigonal, hexagonal	a=b	$\alpha=\beta=90^o$, $\gamma=120^o$
Cubic	a=b=c	$\alpha=\beta=\gamma=90^o$

X-rays generated by using a sealed tube. A flat plate of pure metal is used as anode and with a voltage source of 30-60 kV beam of electrons are generated in cathode and focused onto the anode. During transportation, electrons hit the target material and their kinetic energy turns into a characteristic radiation. By changing the anode material, emitted x-ray can be changed. For x-ray diffraction, K_α radiation is normally employed and in order to eliminate the radiations from lower wavelengths such as K_β suitable filter is used [54]. Table 6.5 shows the five common anode materials and the suitable filters [55].

Table 6.5 Common anode sources with suitable filters.

Metal	Wavelength (Å)			β Filter
	$K_{\alpha 1}$	$K_{\alpha 2}$	K_β	

Cr	**2.28975**	**2.293652**	**2.08491**	**V**
Fe	**1.93608**	**1.94002**	**1.75664**	**Mn**
Co	**1.78900**	**1.79289**	**1.62082**	**Fe**
Cu	**1.54059**	**1.54441**	**1.39225**	**Ni**
Mo	**0.70931**	**0.71361**	**0.63230**	**Nb, Zr**

Generated x-ray beam hits the sample and then it is diffracted with an angle θ determined by the distance between the planes. Interatomic planes are represented with Miller indices and they are parallel to each other. All planes will be observed with the beam and each type of plane will occur at its characteristic diffraction angle. By changing the experimental angle 2θ, all possible diffraction peaks will be obtained. Bragg's Law presents a simple way of understanding and predicting diffraction phenomena.

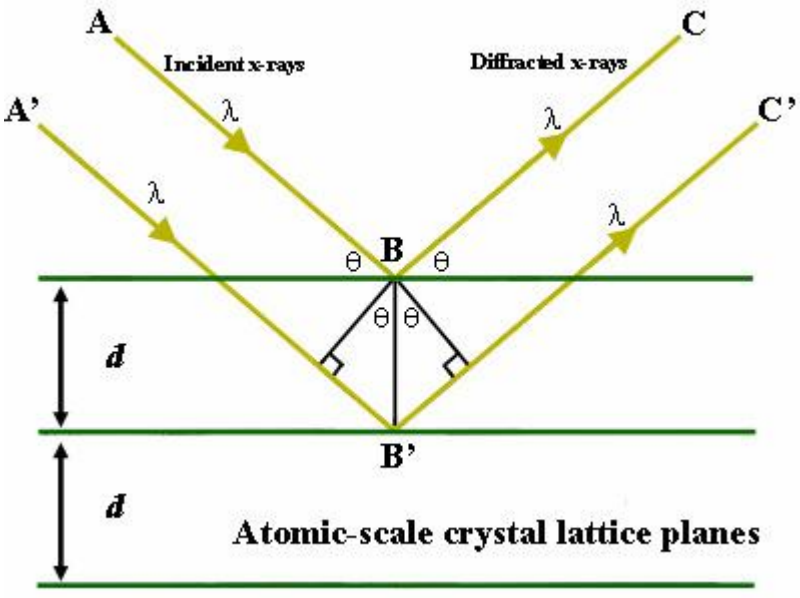

Figure 6.14 Geometric representation of Bragg's Law

$$n\lambda = 2d_{hkl}\sin\theta_{hkl} \qquad \text{Eq 6.5 [56]}$$

X-ray diffraction phenomenon is based on Bragg's law where n is an integer, λ is the wavelength of the x-ray, *d* is the interplanar spacing and θ is the diffraction angle. In that formula, $2d_{hkl}\sin\theta_{hkl}$ is the difference of the paths of a pair of waves before and after reflection from neighboring parallel planes and $n\lambda$ is the constructive interference observed with the order of reflection of *n* [57].

6.4.3. Rietveld Method

Rietveld Method is used for quantitative phase analysis by developing a calculated full pattern. In order to perform the Rietveld method approximate crystal structure should be known. It uses neutron powder diffraction data and it takes the difference between the observed and the calculated intensities at every step and minimizes. The minimized quantity is the conventional least squares residual which was given in equation 6.6.

$$R = \sum w_j \left| I_{j(o)} - I_{j(c)} \right| \qquad \text{Eq 6.6}$$

where $I_{j(o)}$ and $I_{j(c)}$ are the intensities observed and calculated, respectively. w_j is the weight. Although Rietveld method is a powerful technique for structure determination, it is experience dependent. The quality of the powder diagram and the ability of the user on refinement sequence is highly important. The Rietveld refinement is performed with the WinCSD program [57].

6.4.3.1. Experimental

In this thesis, two different types of compounds were studied. Clathrate types of compounds are highly air and moisture sensitive. Therefore, their preparations were performed in glove box. Transition metal borides are stable in air and moisture. For both type, compounds were finely ground. Air sensitive ones were sandwiched between two Polyimide (Kapton) films and for the air stable ones Mylar films were used. Both films were placed onto aluminum ring holders. Prior to placing them into rings, silicon oil was smeared on the periphery of the rings and inside the films as well. This is also help to seal it further from the air and it prevents the powder from moving during the measurement. Second protecting film was placed onto them and films were stretched and squeezed into the ring.

HUBER G670 diffractometer with a germanium monochromator was used for x-ray diffraction analysis. $CuK\alpha_1$ radition with the wavelength of 1.5405929 Å was preferred. The data is collected between the angle range of $5^o<2\theta<100^o$ with 0.005º increments. Further data manipulations were performed with STOE WinXPOW software.

6.5 Energy/Wavelength Dispersive X-ray Fluorescence Analysis

6.5.1. Theory

X-ray fluorescence spectroscopy is widely used to identify elements in a substance. Furthermore, it is also used for quantifying the amounts of elements present in the sample at the ppm level with a great precision. The system is basically based on determining the characteristic wavelength or energy of the element. The quantification is performed by measuring the intensity of element's characteristic emission. There are two widely used fluorescence techniques: Energy dispersive X-ray and Wavelength dispersive X-ray.

Both of methods typically utilize activity in the first three electron orbitals which are K, L and M lines. When high energy primary X-ray photons are emitted from the source, they go and strike the sample. Those photons have enough energy to knock electrons out of the innermost orbitals (K or L), subsequently, they will form unstable ions. For gaining the stability back, an electron from outer most orbital, L or M, will move into the vacant position. While that electron moves from outer orbital to the inner one, it will emit an energy which is known as the secondary X-ray photon. That secondary X-ray produced is characteristic to each specific element. As a consequence, fluorescence will form and the energy of the emitted fluorescent X-ray photon will be determined by having the difference in energies between the initial and final orbitals [58,59]. Figure 6.15 illustrates how fluorescence forms [60].

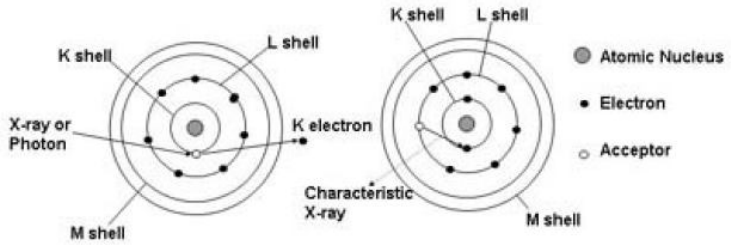

Figure 6.15 Fluorescence generation

Energy and wavelength relation is described with the equation 6.7 where h is the Planck's constant; c is the velocity of light and λ is the characteristic wavelength.

$$E=hc/\lambda \qquad \text{Eq 6.7}$$

Energy dispersive X-ray analysis and wavelength dispersive X-ray analysis are very similar to each other, except the detectors of them. EDXS detects the characteristic energies of elements. Its X-ray sensitive detector is equipped with liquid nitrogen dewar for cooling and most common detectors are made of Si (Li) crystals. Detectors absorb the energy of incoming x-rays by ionization; as a consequence free electrons are formed in the crystal which also makes it conductive. An electrical charge bias is obtained. Those electrical pulses correspond to characteristic X-rays of the elements [61].

WDXS works in the similar way with EDXS. WDXS system uses a crystal for dispersing the X-ray. Most commonly gas proportional counters are used in such systems. X-ray photon ionizes a gas atom and formed electron moves toward the body, consequently a pulse which is proportional to the energy of the incident photon is formed. WDXS performs the measurement in terms wavelength and EDXS performs the measurement in terms energy. Compared to EDXS, WDXS system is more advantages in terms of higher spectral resolution especially in longer wavelength or in low energy region. Furthermore, it has the ability of measuring ultralight elements down to boron and beryllium. On the other, it provides more complex system and it requires high power X-ray source [62].

6.5.2. Experimental

EDXS and WDXS microstructure analyses were performed by embedding a piece of sample into epoxy resin substrate which increases the surface conductivity. Figure 6.16 shows an example of sample embedded into epoxy resin [63].

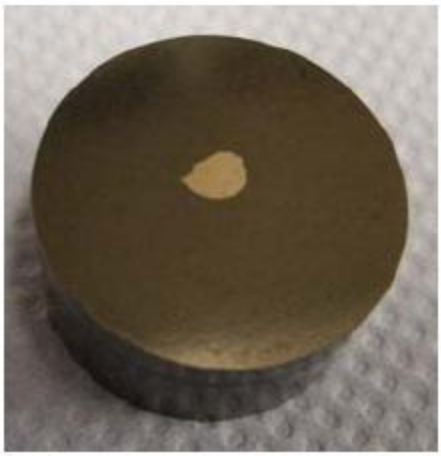

Figure 6.16 Sample embedded into epoxy resin for WDXS or EDXS measurement

Prepared sample was polished with different micron sized diamond powders in paraffin. Philips XL 30 SEM with integrated EDXS spectrometer and Cameca SX 100 WDX spectrometers were used for the measurements. Data handling was performed with EDAX software and the optical microscope images were collected with Light Optical Polarization Microscope from Zeiss Axio Plan 2.

6.6 Thermal Analysis Techniques

Thermal analysis methods measure the changes in physical or chemical properties of a substance and this is constructed as a function of temperature. This definition also contains the methods that measure the changes in weight and in energy as well. There are several types for thermal analysis and those are thermochemical analysis (TMA), thermogravimetry (TG), differential thermal analysis (DTA), differential scanning calorimetry (DSC) and evolved gas analysis (EGA). However, this study mainly concentrates on the thermogravimetry and differential thermal analysis.

6.6.1. Theory

Thermogravimetry is based on the precision balance with linear rise of temperature with time. In other words, changes in weight are recorded as a function of temperature or time [64]. There is also another option which is the derivative thermogravimetric (DTG) curve. In this method, it takes the first derivative of thermogravimetric curve with respect to temperature or time. Figure 6.17 shows a typical thermogravimetric curve [65].

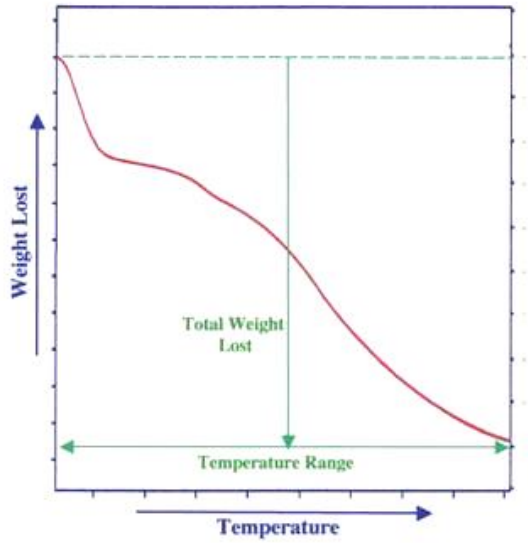

Figure 6.17 Typical thermogravimetric curve

There are several applications of thermogravimetric method.

1. Determination of purity and thermal stability of both primary and secondary standards
2. Investigation of drying temperatures
3. Determination of the composition of alloys and mixtures.

In differential thermal analysis (DTA), temperature is measured with respect to a reference usually alumina. Controlled heating or cooling program is applied and the difference between the sample and reference material is recorded with respect to temperature. Therefore, endothermic and exothermic changes will be observed in the graph. Physical changes usually yields endothermic curves and chemical reactions yield exothermic reactions [64]. Figure 6.18 shows an apparatus for conventional DTA and figure 6.19 shows a typical curve for DTA [65,66].

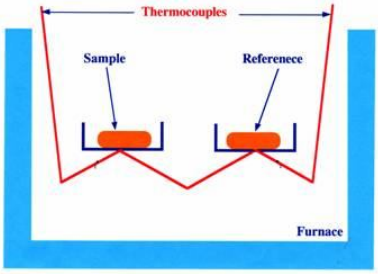

Figure 6.18 Apparatus for conventional DTA

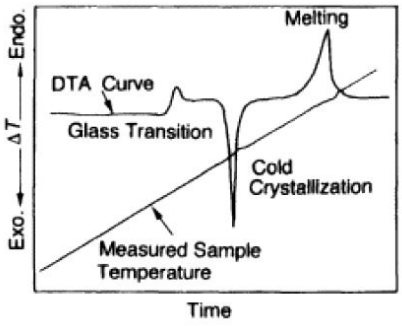

Figure 6.19 Schematic illustration of DTA curve

6.6.2. Experimental Method

NETZSCH STA 449 instrument in which heating is possible from room temperature to 1100 ^{o}C was used for the DTA/TG measurements. In clathrate compounds, measurements were performed to obtain the reaction temperatures by applying a heating/cooling rate of 10 ^{o}C /min. Once the final temperature of heating cycle was completed, the cooling process was immediately begun without further preservation time at that temperature. For the transition metal borides, the instrument was not sufficient to use for the detection of melting. Their melting point is much higher than 1100 ^{o}C. However, measurements were used to further prove the absence of binary. Furthermore, it was also used to prove that they are stable until 1100 ^{o}C which is a desirable property in industry.

Samples were ground finely in order to obtain a homogenous temperature through the whole sample. Air sensitive samples were prepared in glove box. All samples were measured in aluminum oxide crucibles. Approximately 10 mg of samples were prepared and proper weighing was also obtained for TG measurements. 150 ml/min argon gas flow was preferred for air sensitive ones. For the stability check, transition metal boride measurements were performed under synthetic air. After each measurement, X-ray powder diffraction analysis was applied in order to determine the type of products formed during the heat treatment.

6.7 Hardness Measurements

6.7.1. Theory / Measurement

Hardness is defined as resistance of a material to a permanent deformation. Deformation contains the indentation, scratching, cutting or bending. Plastic deformation of the surface is used for the hardness analysis of metals, ceramics and most polymers. On the other hand, elastic deformation is used for the elastomers and some polymers. Since there is no single definition for hardness, it is usually considered as the combination of yield strength, work hardening, tensile strength, modulus and other factors. There are different tests for the measurement of hardness. Mohr hardness, Brinell hardness, Rockwell hardness, Scleroscope and Rebound hardness, Durameter hardness, Barcol Hardness and Vickers and Knoop Microhardness are some of them. In this study, Vickers Microhardness measurements were performed. For those measurements, arc melted samples were cut into two for obtaining a flat surface and then surface is polished. A small diamond pyramid is dipped into the sample under loads. Only difference in Vickers microhardness measurement from Knoop microhardness measurement is the shape of the diamond pyramid. In Vickers microhardness test, square pyramidal indenter is used. On the other hand, in Knoop

microhardness test rhombic-based pyramidal indenter is used. Diagonals of impressions were measured and those values were used to obtain hardness number [67]. Figure 6.20 shows the hardness measurement results of ReB_2 under applied load [68].

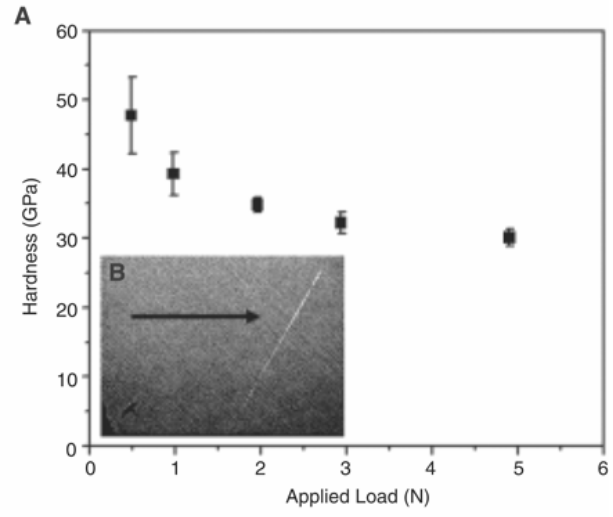

Figure 6.20 Hardness of ReB_2 plotted as a function of applied load

6.8 Mass Spectroscopy

6.8.1. Theory

Heating process usually involves formation of gases due to decomposition or desorption. Mass spectroscopy is a powerful technique for identifying those unknown compounds. Mass spectroscopy is based upon the separation of the rapidly moving ions. Mass to charge ratios (*m/z*) of those ions affects that motion. Figure 6.21 represents the block diagram of mass spectrometer.

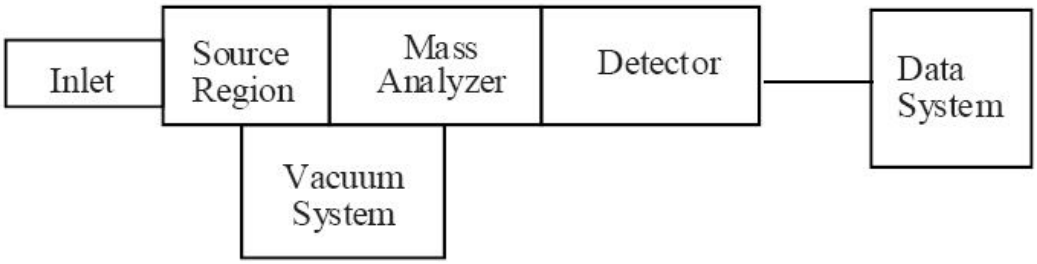

Figure 6.21 Mass spectrometer block diagram

In the inlet part, sample is transferred into the vacuum part and source region ionizes the neutral sample molecules. Ionized molecules are accelerated into the analyzer with a help of an electric field. Using mass to charge ratio, ions are separated and then detected. Analysis part is the most important part of mass spectroscopy. Each analyzer has very different operating characteristics.

Usually mass spectrometers are named in terms of their filters and the one used in the analyses are quadrupole. This type of mass spectrometer is one of the most common mass analyzer. Their sizes are compact and scan rates are fast. The quadrupole analyzer consists of four rods and those rods are arranged as configured in figure 6.22.

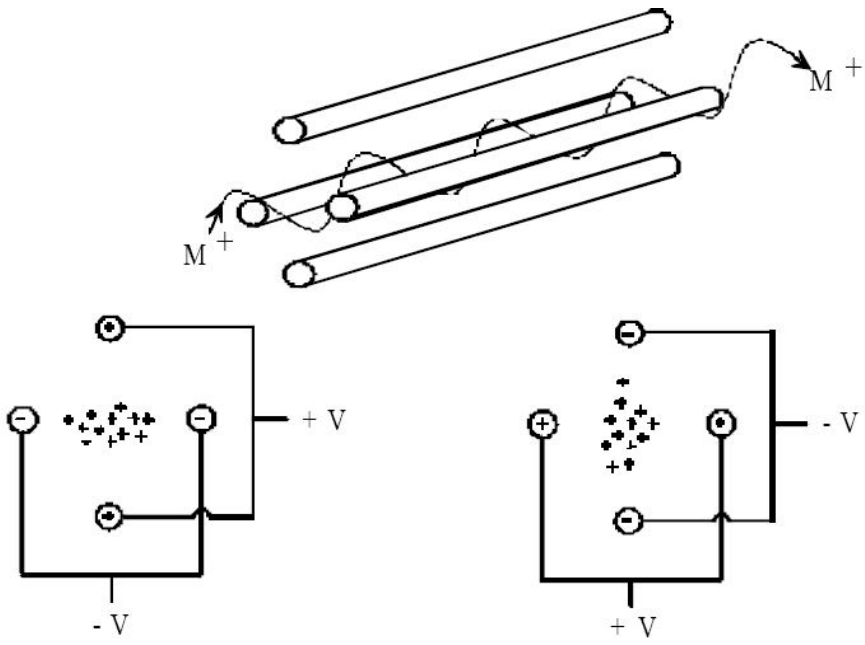

Figure 6.22 Quadrupole mass analyzer

Specified mass to charge ratio is detected with a radio frequency. Voltages applied to the electrodes and those voltages produce oscillating electric field which functions as a filter to the transmitted molecule. By selecting a suitable radio frequency and potential, ions are separated from each other [69].

Sample preparation characterization was performed with ThermoStar^{TM} GSD 301 T. First sample was placed into DTA/TG instrument and argon gas flow was adjusted to 100 ml/min. Ion currents of the selected mass channels were recorded with respect to time.

6.9 Inductively Coupled Plasma

6.9.1. Theory

Inductively coupled plasma (radiofrequency) is one the most common plasma source. It contains three glass tubes of a plasma torch. Each glass tube is equipped with a plasma and coolant. Outermost glass tube is cover with a coil of copper and power input to the system is supplied with that copper coil. Controllable energy source which allows the proper energy needed to excite all elements without appreciable ionization is required. ICP-OES optical emission spectroscopy utilizes plasma excitation source. Argon gas is used in order to obtain plasma in the system. After atoms gain energy from collisions, they start emitting light of a characteristic wavelength. Careful grating of the system enables quantitative characterization. Schematic presentation of ICP is given in figure 6.23 [70].

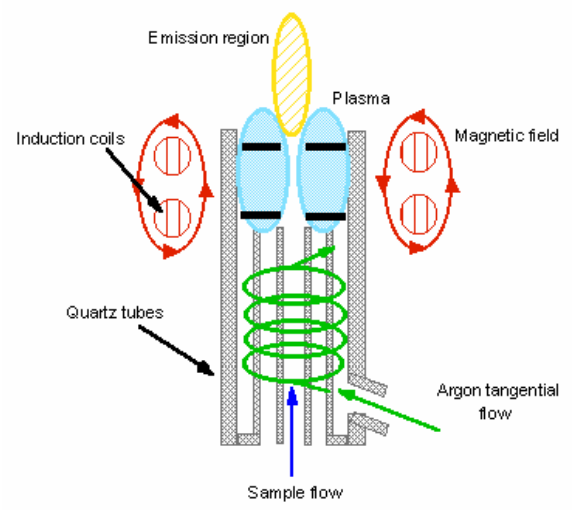

Figure 6.23 Schematic representation of inductively coupled plasma

6.9.2. Sample Preparation

Since ICP-OES system is a very sensitive system; therefore, every equipment used in the measurement is cleaned thoroughly and dried at 383 K. A standard method was formed for the quantification of the analyses. Therefore, ICP-OES standards were purchased and different concentrations of those solutions were prepared. For the characterization of ReB_2 and Re-Ni-B compounds, samples were dissolved in 10% HNO_3 and then diluted to 50 ml. Results obtained from analyses was sensitive in ppm level.

Appendix

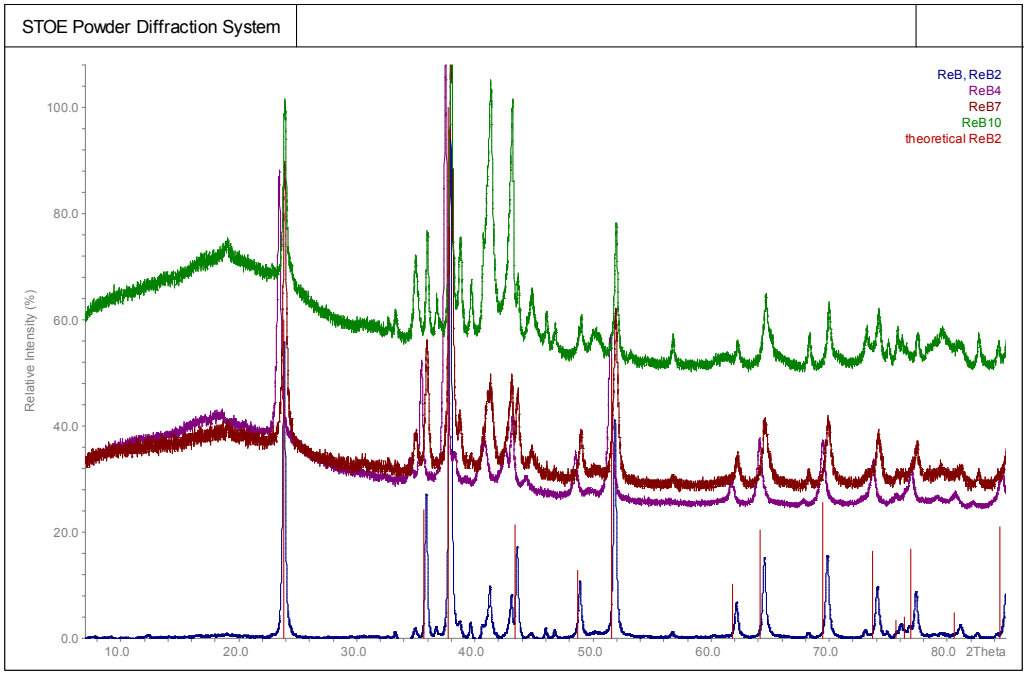

Figure A. 1 Comparison of X-ray diagram Re/B at different atomic ratios in microwave induced plasma

```
clear all; close all; clc; format long


x = [0.206637 0.307952 0.325005 0.371074 0.437209]';

% x represents the sin theta values in radians.

y = [0.0054633 0.0054228 0.0055268 0.0067394 0.0062244]';

% y represents FWHM values multiplied with cos theta. Both of them in
radians.

%equations given below are used to check the curve fit with
overdetermined system.
```

```
% C      = [x ones(size(x))];
% r      = [y];
% DetC   = det(C);     %%%% SEE IF IT IS NONZERO
%                     %%%% TO HAVE A UNIQUE SOLUTION!
% u      = C\r;
% m      = u(1)
% b      = u(2)
% xx     = linspace(x(1)-1,x(end)+1,1001);
% yy     = m*xx+b;
% figure(5)
% plot(x,y,'ro', xx,yy,'b-', 'linewidth',2)
% xlabel('x'), ylabel('y'), grid on
% legend('Given data','Exact polynomial fit',0)


% %%% Curve fit by using OVERDETERMINED SYSTEM OF EQUATIONS
%
C  = [x ones(size(x))];
a  = (C'*C)\(C'*y);
A  = a(1);
B  = a(2);
xxd  = linspace(x(1),x(end),1001);
yyd  = A.*xxd + B;

% plot(xxd,yyd,'r-', 'linewidth',1)

u=std(yyd)
A
B
```

Figure A. 2 MATLAB programming used for Hall-Williamson Plot

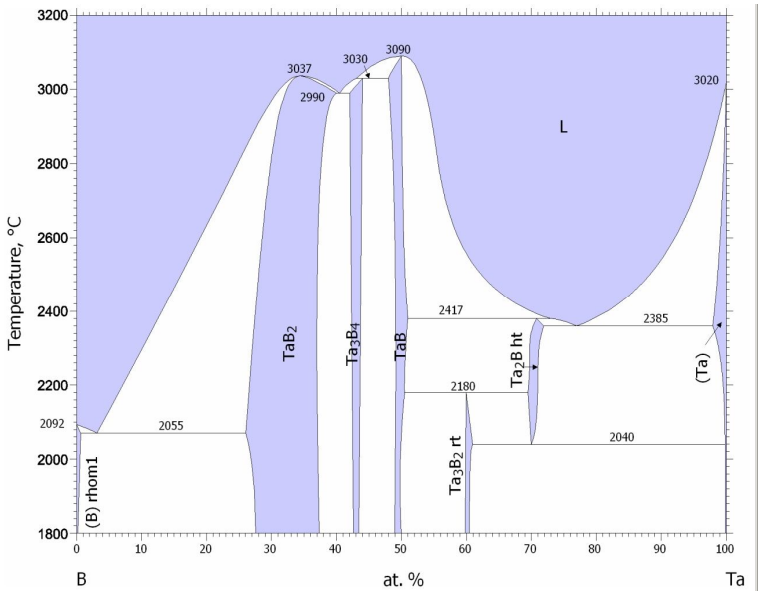

Figure A.3 Phase diagram of Ta-B

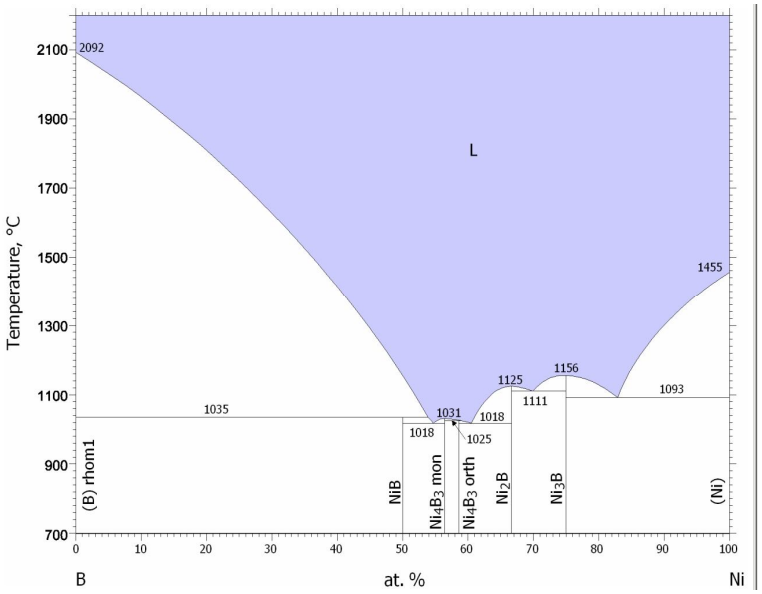

Figure A.4 Phase diagram of Ni-B

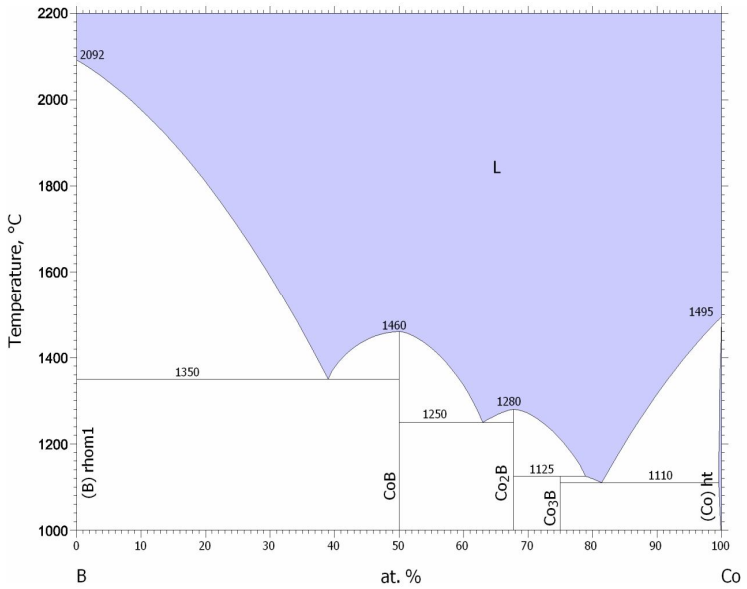

Figure A.5 Phase diagram of Co-B

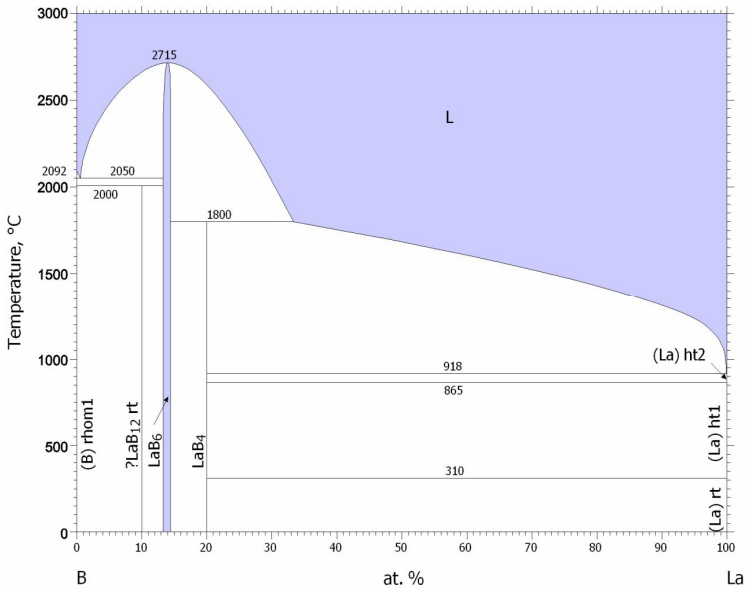

Figure A.6 Phase diagram of La-B

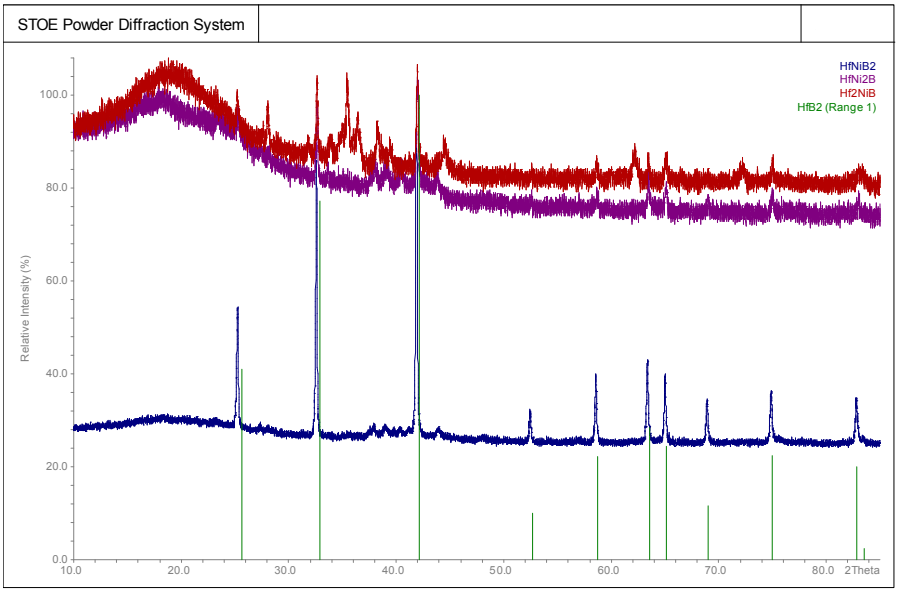

Figure A.7 Comparison of X-ray diagram of Hf-Ni-B compounds

Bibliography

Bibliography

1. M. Gerloch, E.C.C., *Transition Metal Chemistry: the Valence Shell in d-Block Chemistry* 1994, New York: VCH Verlagsgesellschaft.
2. N.N. Greenwood, A.E., *Chemistry of the Elements* second ed. 1997, Oxford: Butterworth - Heinemann.
3. *Model ChemLab*. [cited.
4. D.F. Shriver, P.W.A., *Inorganic Chemistry* third edition ed. 2001: Oxford University Press.
5. Group, t.B. *Crystal Field Theory* [cited.
6. Karlin, K.D., *Progress in Inorganic Chemistry* 1997, New York: Wiley
7. Williams, W.S., *Transition Metal Carbides, Nitrides and Borides for Electronic Applications.* JOM, 1997: p. 38 - 42.
8. Gorshkov B.N., K.Y.P., Laskutov V.S., Nerorov V.A., Alekseev V.V., *Application of coatings of some metal borides by plasma deposition* Powder Metallurgy and Metal Ceramics 2004: p. 350-353.
9. Demeter Tzeli, A.M., *Electronic structure and bonding of the 3d transition metal borides, MB, M = Sc, Ti, V, Cr, Mn, Fe, Co, Ni and Cu through all electron ab initio calculations.* The Journal of Chemical Physics 2008. **128**: p. 034309-1.
10. Lundström, T., *Structure, defects and properties of some refractory borides.* Pure & Applied Chemistry 1985. **57**(10): p. 1383 - 1390.
11. Matkovich, V.I., *Boron and Refractory Borides*. 1977, Berlin; New York: Springer - Verlag.
12. Hideki Abe, K.Y., *Electrochemical Synthesis of Superconductive Boride MgB_2 from Molten Salts.* Journal of Applied Physics, 2002.
13. Kiessling, R., *The Borides of Tantalum* Acta Chemica Scandinavica, 1949. **3**: p. 603 - 615.
14. M.A. Ponomarev, Y.A.S., *Plasma - Arc Growth of Refractory Single Crystals from SHS Products and Green Mixtures: an Autoreview.* International Journal of Self - Propagating High - Temperature Synthesis, 2009. **18**(1): p. 51 - 59.
15. Mercouri G. Kanatzidis, R.P., Wolfgang Jeitschko, *The Metal Flux: A Preparative Tool for the Exploration of Intermetallic Compounds.* Angewandte Chemie, 2005. **44**: p. 6996 - 7023.
16. Yu. B. Kuz'ma, N.F.C., *Phase Equilibrium at 800 ^{o}C in the Ta-Co-B and Nb-Co-B systems.* Plenum Publishing Corporation, 1980.
17. Walter Steurer, P.R.u.H.N., *Neue Boride mit NbCoB2-Typ.* Monatshefte für Chemie, 1978. **109**: p. 919-924.

18. Kuz'ma, Y.B.L., V.I.; Stadnyk, B.I.; Chaban, N.F., *System Tantalum-Rhenium-Boron.* Akademiia Nauk Ukrains'koi RSR, Dopovidi, Seriia A-Fiziko-Tekhnichni i Matematichni Nauki. , 1971. **33**: p. 849-851.
19. Kuz'ma, Y.B.,
Phase Equilibria in the Hf-Co-B, Hf-Ni-B and Nb-Mn-B Ternary Systems Khim., 1972. **14**: p. 20-24.
20. E.M. Slyusarenko, A.V.P., E.Yu. Kerimov, M.V. Sofin, D.Yu. Skorbov *Ternary systems of nickel and rhenium with transition metals* Journal of Alloys and Compounds, 1998. **264**: p. 180-189.
21. Qinfen Gu, G.K., Walter Steurer, *Transition Metal Borides: Superhard versus Ultra - incompressible.* Advanced Materials 2008. **20**: p. 3620 - 3626.
22. Alessandro Latini, J.V.R., Daniela Ferro, Roberto Teghil, Valerio Rossi Albertini, Sergey M. Barinov, *Superhard Rhenium Diboride Films: Preparation and Characterization.* American Chemical Society 2008. **20**: p. 4507 - 4511.
23. Musil, J., *Hard and superhard nanocomposite coatings.* Surface and Coatings Technology 2000. **125**: p. 322 - 330.
24. Hsiu-Ying Chung, M.B.W., Jonathan B. Levine, Abby Kavner, Jenn-Ming Yang, Sarah H. Tolbert, Richard B. Kaner, *Synthesis of Ultra-Incompressible Superhard Rhenium Diboride at Ambient Pressure* science 2007. **316**: p. 436-439.
25. Yongcheng Liang, B.Z., *Mechanical and Electronic properties of superhard ReB_2.* the American Physical Society 2007. **76**: p. 132101-1-4.
26. Sam La Placa, B.P., *The Crystal Structure of Rhenium Diboride.* Acta Chemica Scandinavica, 1962. **15**: p. 97 - 99.
27. Natalia Dubrovinskaia, L.D., Vladimir L. Solozhenko *Comment on 'Synthesis of Ultra-Incompressible Superhard Rhenium Diboride at Ambient Pressure'.* Science 2007. **318**: p. 1550.
28. Shigeki Otani, T.A., Yoshio Ishizawa *Preparation of ReB_2 single crystals by the floating zone method* Journal of Alloys and Compounds 1997. **252**: p. 19-21.
29. Jonathan B. Levine, S.L.N., Haider I. Rasool, Jeffrey A. Wright, Stuart E. Brown and Richard B. Kaner, *Preparation and Properties of Metallic, Superhard Rhenium Diboride Crystals.* Journal of American Chemical Society, 2008. **130**: p. 16953-16958.
30. Antonio Mario Locci, R.L., Roberto Orru, Giacomo Cao, *Reactive Spark Plasma Sintering of Rhenium Diboride* Ceramics International 2009. **35**: p. 397-400.
31. Fridman, A., *Plasma Chemistry* 2008: Cambridge University Press
32. Annemie Bogaerts, E.N., Renaat Gijbels, Joost van der Mullen *Gas Discharge Plasmas and Their Applications* Spectrochimica Acta Part B, 2002. **57**: p. 609-658.
33. Katsuhiro Nishiyama, T.N., Shigenori Utsumi, Hideki Sakai *Preparation of ultrafine boride powders by metallothermic reduction method.* Journal of Physics. **176**: p. 1-8.

34. http://webbook.nist.gov/chemistry/.
35. P. Kameli, H.S., A. Aezami, *Effect of particle size on the structural and magnetic properties of $La_{0.8}Sr_{0.2}MnO_3$.* Journal of Applied Physics 2006. **100**: p. 053914-1-4.
36. IncWebFinance, I., www.science-dictionary.com. 2010.
37. Vaidya, S., *Clathrates: an Exploration of the Chemistry of Caged Compounds.* Resonance 2004: p. 18-31.
38. Davy, H., Philosophical Transactions of the Royal Society of London 1811. **101**: p. 155.
39. Faraday, M., *On hydrate of Chlorine* Quartly Journal of Science 1823. **15**: p. 71.
40. M. von Stackelberg, O.G., J. Pietuchovsky, O. Witscher, H. Fruhbuss, and W. Meinhold, *Structure and Formula of Gas Hydrates* Fortschr. Mineral., 1947. **26**: p. 122.
41. J. S. Kasper, P.H., M. Pouchard, and C. Cros, *Clathrate Structure of Silicon Na_8Si_{46} and Na_xSi_{136}.* Science, 1965. **150**: p. 1713-1714.
42. J. Gallmeier, H.S., and A. Weiss, Naturforsch, 1969. **24b**: p. 665.
43. Svilen Bobev, S.C.S., *Clathrates of Group 14 with Alkali Metals: An Exploration.* Journal of Solid State Chemistry, 2000. **153**: p. 92-105.
44. Svilen Bobev, S.C.S., *Isolated deltahedral clusters of lead in the solid state: synthesis and characterization of Rb_4Pb_9 and $Cs_{10}K_6Pb_{36}$ with Pb_9^{4-}, and $A_3A'Pb_4$ (A=Cs, Rb, K; A'=Na, Li) with Pb_4^{4-}.* Polyhedron 2002. **21**: p. 641-649.
45. Shoji Yamanaka, E.E., Hiroshi Fukuoka, Masahiro Yasukawa *High-Pressure Synthesis of a New Silicon Clathrate Superconductor, Ba_8Si_{46}.* Inorganic Chemistry 2000. **39**: p. 56-58.
46. T.F. Fassler, S.P., *Crystal Growth and Structure Refinement of K_4Ge_9.* Zeitschrift für anorganische und allgemeine Chemie 2007. **633**(3): p. 393-397.
47. Amberger, W.S.E., *Gmelin Handbook of Inorganic Chemistry. Boron Supplement*, ed. K.C. Buschbeck. Vol. 2. 1981: Berlin: Springer - Verlag.
48. Lawrence, B., *Gmelin Handbook of Inorganic and Organometallic Chemistry Boron Compounds 4th supplement* ed. K.N.J. Faust. Vol. 1a. 1994: Berlin: Springer-Verlag.
49. Acar, S., *Phd proposal: 'Novel Synthesis Methods for High Purity Amorphous Boron'* 2010, Koç University
50. *Centorr Vacuum Industries Arc Melting* [cited 2010.
51. www.vac-atm.com/omni. [cited.
52. M.F.C. Ladd, R.A.P., *Structure Determination by X-ray Crystallography* 1993, New York: Plenum Publishing Corporation
53. Speakman, S.A. *Basics of X-ray Diffraction: Self-User Training for the X-ray Diffraction SEF* [cited 2010.
54. Massa, W., *Crystal Structure Determination* 2004: Springer.
55. Zavalij, V.K.P., *Fundamentals of Powder Diffraction and Structural Characterization of Materials* 2005, New York Springer

56. Eby, G.N., *Principles of Environmental Geochemistry* 2004: Thomson-Brooks/Cole Learning.
57. Ron Jenkins, R.S., *Introduction to X-ray Powder Diffractometry* 1996: Wiley-Interscience Publications
58. http://www.equipcoservices.com/support/tutorials/introduction-to-xrf-spectrometry/. *X-ray Fluorescence (XRF) Spectrometry* [cited 2004-2010.
59. Goldstein, J., *Scanning electron microscopy and X-ray microanalysis* 2003: Kluwer Adacemic/Plenum Publishers
60. http://www.seiko-instruments.de/files/xrf_principle.pdf. *X-ray Fluorescence Analysis* [cited.
61. Severin, K.P., *Energy Dispersive Spectrometry of Common Rock Forming Minerals* 2004: Kluwer Academic Publishers
62. B. Beckhoff, N.L., R. Wedell, H. Wolff, *Handbook of Practical X-Ray Fluorescence Analysis* 2006: Springer
63. Aydemir, U., *Clathrate I Compounds of Barium with Transition Metal, Silicon and Germanium Framework and Contributions to TaNiSi* in *MASE*. 2006, Koç University
64. J. Mendham, R.C.D., J.D. Barnes, M. Thomas, *VOGEL's Textbook of Quantitative Chemical Analysis* 2000: Pearson Education Limited
65. Scott, R.P.W., *Book 5: Thermal Analysis*
66. T. Hatakeyama, F.X.Q., *Thermal Analysis: Fundamentals and Applications to Polymer Science.* 1999.
67. Vladislav Navratil, J.N., *Some problems of Microhardness of Metals* Journal of Applied Mathematics 2009. **2**.
68. Boyer, H.E., *Hardness Testing* 1987: ASM International
69. Russell D.H., *Experimental Mass Spectroscopy,*1994.
70. Dean, J.R., *Practical Inductively Coupled Plasma Spectroscopy* 2005: WILEY.

VITA

Burcu Uslu was born in 1984, in Turkey. She graduated from Kabataş Erkek Lisesi in 2003 as the second best student. Same year, she started her study in Chemistry department at Koç University, İstanbul. In 2008, she received her B.S. degree as the second best student of the department and started to study her Master thesis in the program Material Science and Engineering at Koç University. Her research interests are on investigations with transition metal borides, superhard materials and clathrate compounds.